Building A Magnesium Ion Trap For Quantum Computation

Building A Magnesium Ion Trap For Quantum Computation

By

Jiajia Zhou, B.Sc.

A Thesis

Submitted to the School of Graduate Studies

in Partial Fulfilment of the Requirements

for the Degree

Master of Science

McMaster University

MASTER OF SCIENCE (2007) McMaster University

(Department of Physics and Astronomy) Hamilton, Ontario, Canada

TITLE: Building A Magnesium Ion Trap For Quantum Computation

AUTHOR: Jiajia Zhou, B.Sc.

SUPERVISOR: Dr. Brian King

NUMBER OF PAGES: xvi, 115

Abstract

Trapped ions are one of the best candidate systems to realize quantum computation. In our laboratory, we are trying to implement quantum computing and information processing: two hyperfine ground-states of magnesium-25 ions will serve as the two-level system to store quantum information. The ions are confined in a linear radio-frequency trap under ultra-high vacuum conditions and will be cooled down to their motional ground-states. By illuminating the ions with frequency-stabilized lasers we will be able to initialize, manipulate, and read out their internal electronic quantum states in a well-controlled way and with high fidelity. In addition, the ions can be made to interact with each other by coupling their internal electronic states to a collective vibrational mode of motion along the trap axis. In this thesis, the focus will be on the process of building a trapped-magnesium-ion quantum information processor.

Acknowledgements

I would like to take this opportunity to thank my supervisor, Brian King. Your patience, determination and knowledge are greatly admired and appreciated. Thanks for giving me the opportunity to explore the wonderful quantum and experimental physics worlds.

I would also like to thank my labmates Jason and Laura. I have learned a lot from you both. Jason, thanks for those smokes I bummed off you. The time we spent outside always gave me a much-needed break. Laura, thanks for introducing me to the magic of dark chocolate. It gave me a little bit of sweetness during my boring thesis-writing. Also thanks for not bugging me during my writing. I can't image how long this thesis would have taken if you were around :-).

I also want to thank all the summer students who have worked in our lab: Peter, Swati, Jesse, John, Sarah, Agnes, Daniel, James, Martin, Vick, Katie, Mike, Ben and Nick. You guys made the summer the most fun time during the year.

I want to thank all my teachers at McMaster. You taught me a lot, not just the knowledge but also how to be a good person. I also want to thank all my friends here. You guys are wonderful and I couldn't imagine what my life would be without you. Thanks to Cao Jun, Ning Fanlong, Zhou Zhuowei, Sun Youhai, Zhao Yang and Liang Yu. The paper-card games are always great.

Thanks to my friends Ai Yinghua, Xiao Lingyi, Yang Lilin (for the awesome xenogears and mgs series), Jin Xiaoliang, Shen Wenjing, Wang Wei, Qin Wenjia (for the ps2), Zhang Rui, Fang Hao (thanks for the psp) and Zhu Taoxi. Every time I run into problems, you are always there for me.

I thought I've got almost everyone until *caring is creepy* starts to play in the background. Without The Shins' *Oh, Inverted World* and Magnetic Fields' *69 Love Songs*, those late nights would be much longer. So thanks. Also thanks to Steve Jobs: macbook is wonderful, if only it could be cheaper.

Finally, I would like to thank my parents, Kang Zhengfen and Zhou Yiping. Without your support I would never have been able to make it. Thank you.

Neatly constructed apparatus may work; sloppily built apparatus never do.

Table of Contents

List of Figures

List of Tables

Chapter 1

Introduction

Classical computers have been with us for more than half a century and we have enjoyed the benefits of the fast calculation provided by modern processors. In the course of computer development, people started to ask questions like "what are the possibilities for and the limitations of classical computers?" It turns out there is a set of computational problems which are hard, intractable and infeasible, even with the most powerful state-of-the-art modern computers.

One of these problems is to predict the behavior of a quantum system. Quantum mechanics is the most accurate and complete description of the world known. It associates the state space of an isolated physical system with a complex vector space (Hilbert space), and it allows for the possibility of superposition states. For example, for a system consisting of $n = 100$ two-level atoms, we need $2^n = 1.27 \times 10^{30}$ coefficients to specify the state of this system, whereas a classical system would require 200 numbers. The requirement of exponentially increasing resources to describe a quantum system makes it very difficult to simulate such a system.

It was Richard Feynman [1] who first asked if we could simulate quantum mechanics with a new kind of computer – a quantum computer built out of quantum elements and obeying the laws of quantum mechanics. That way, quantum mechanical properties like superposition and entanglement would be inherently included in the computer hardware.

After Feynman's paper in 1982, it was David Deutsch, a physicist from Oxford, who made the next advance. In his 1985 paper [2], he proved that quantum computers have the ability to do calculations that conventional computers are unable to do efficiently. However, people found it challenging to come up with good quantum algorithms to solve difficult problems. It was not until 1994 that interest in quantum computing really exploded. The reason was that Peter Shor of Bell Labs had discovered a quantum algorithm that could *efficiently* solve the factoring problem [3, 4], for which people believed that there are no efficient solution using classical computers.

Shor's discovery resulted in increased theoretical interest in finding physical systems amenable to implementing universal quantum computation. Trapped ions emerged as one of the candidates that fulfilled the requirements for constructing a quantum computer. This largely resulted from two ground-breaking inventions in atomic physics: ion trapping and laser cooling. A Nobel Prize has been awarded for each of these achievements [5, 6, 7, 8, 9]. Ion traps provided the ability to confine and manipulate a two-level quantum system – an atomic ion – in a well-controlled manner. Laser cooling enabled the precise control of trapped ions and coherent coupling between the internal states and motional states (see Refs. [10, 11, 12, 13]).

In 1995 Cirac and Zoller presented the first formal proposal for implementing a quantum gate with trapped ions [14]. The Cirac-Zoller scheme involves entangling the internal states of the ions by coupling to their collective quantized motion. A few month later, it was realized experimentally by the NIST Ion Storage group [15]*. In their experiment, they demonstrated the operation of a two-qubit controlled-NOT gate using the Cirac-Zoller scheme. The two qubits consist of a quantized motional qubit and an ionic qubit. The controlled-NOT gate on two ionic qubits was realized

*At the same year, the Caltech Cavity-QED group also realized a conditional phase gate using a single atom strongly coupled to a high-finesse optical resonator [16].

by Innsbruck group in 2003 [17]. At almost the same time, NIST group demonstrated a robust, geometric two ion-qubits phase gate [18].

In our laboratory, we are trying to implement ion-trap quantum computing and information processing: two hyperfine ground-states of magnesium-25 ions will serve as the two-level system to store quantum information. The ions are confined in a linear radio-frequency trap under ultra-high vacuum conditions and will be cooled down to their motional ground-states. By illuminating the ions with frequency-stabilized lasers we will be able to initialize, manipulate, and read out their internal electronic quantum states in a well-controlled way and with high fidelities. In addition, the ions can be made to interact with each other by coupling their internal electronic states to a collective vibrational mode of motion along the trap axis, using the momentum carried by the laser-beam photons.

In this thesis, I will describe the implementation and study of several components of a trapped-magnesium-ion quantum information processor. This thesis is divided into three parts. The first part, consisting of Chapters 2 and 3, focuses on theoretical considerations. Chapter 2 describes the theory of a radio-frequency trap, and the design of a linear ion trap for magnesium. Chapter 3 describes the properties of magnesium ions which can be used to implement quantum computation. The theory of trapped-ion quantum computation is well-described in several references [19, 20, 21]. We will apply some of these results to magnesium ions.

The second part (Chapter 4-7) will describe the details of various systems: trap, vacuum, laser, and imaging. These systems are essential for our ion-trapping. Chapter 4 is devoted to the trap assembly. We will describe the actual trap, the magnesium ovens and the electron guns. The voltage supplies, both dc and rf, will also be described in this chapter. The vacuum system is the topic of Chapter 5. The final pressure should be on the order of 10^{-11} torr, so it is essential to make sure that

everything is as clean as possible during the vacuum cleaning and assembling. Various laser beams needed to address and manipulate magnesium ions are discussed in Chapter 6. We have developed laser sources at ultraviolet wavelengths to drive the transitions of magnesium ions, and also set up Doppler-free saturated absorption spectroscopy of iodine as a frequency reference. Finally, we will describe the imaging system in Chapter 7. The imaging system is used to collect the fluorescence from trapped ions and form an image of the trapped ions.

In the third part of this thesis we present experimental results. Chapter 8 will describe the process of trapping $^{24}Mg^{+}$ ions with our apparatus. Trap frequencies are measured and compared to the results from computer simulations.

Our next goal is to trap $^{25}Mg^{+}$ ions which have the hyperfine structure to serve as our qubit system. We plan to do some preliminary spectroscopy experiments to measure the linewidth of $^{2}P_{1/2}$ states[†], and eventually move on to implement quantum computation using $^{25}Mg^{+}$ qubits.

[†]The outline of this measurement can be found in Laura Toppozini's thesis [22].

Chapter 2

Radio-Frequency Ion Traps

A radio-frequency ion trap (Paul trap) has several unique properties which make it a particularly powerful experimental device. First is its ability to selectively confine charged particles in a small region of space. This permits the realization of high-sensitivity mass spectrometry, which is important in chemistry and physics. On the other hand, an ion trap can hold a single ion nearly stationary at the trap centre. Atomic physics experiments can be conducted with minimal influence of the environment. Third, being a well-isolated quantum system, the trapped ion naturally becomes one of the best candidates to perform quantum computation and simulation.

The purpose of this chapter is to give a brief introduction to the design of a radio-frequency ion trap; emphasis will be placed on the linear rf trap.

At first we will discuss the physics of dynamic stabilization of ions in time-dependent parabolic potentials. By solving the classical equation of motion, we will have a better understanding of how ion traps work. The stability region of a single ion's motion will be introduced in this section. The stability diagram will be useful during the trap design. More detailed discussion can be found in Refs. [20, 23, 6]. A quantum-mechanical approach can be found in Refs. [24, 25, 26, 27]; the results show that in the range of trapping parameters used in the experiments, the classical and quantum treatments give the same conclusion.

In the chapter's second part, we will turn to the linear rf trap, which has the ability to trap several ions at the node of the rf field. The trapping schemes are different in the radial and axial directions, so we will treat them separately. The first linear rf trap was reported in Refs. [28, 29]. A more detailed description about the construction of a linear rf trap can be found in Refs. [30, 31].

We will begin the real trap design in the third part of the chapter. There is a big gap between a physics idea and a laboratory apparatus which works. We will give a step-by-step description of how we bridge this gap.

2.1 How Radio-Frequency Ion Traps Work

2.1.1 Time-Dependent Parabolic Potential

Ions can be bound to a point in space if a force acts on them which has the form:

$$\mathbf{F} = -U_0(\alpha x\mathbf{i} + \beta y\mathbf{j} + \gamma z\mathbf{k}),$$

in other words, if they move in a parabolic potential

$$\Phi(x, y, z, t) = U_0\frac{1}{2}(\alpha x^2 + \beta y^2 + \gamma z^2), \tag{2.1}$$

where (x, y, z) are the components of the displacement vector $\mathbf{r}$.

The Laplace condition $\Delta\Phi = 0$ imposes the relation $\alpha+\beta+\gamma = 0$. This restriction implies that there is no local three-dimensional extremum in free space for a static electric potential, so the ions can only be trapped in a dynamical way.

Suppose the potential varies sinusoidally at the rf drive frequency Ω_T :

$$\Phi(x, y, z, t) = -V_0\cos(\Omega_T t)\frac{1}{2}(\alpha' x^2 + \beta' y^2 + \gamma' z^2). \tag{2.2}$$

At first sight one might expect that the time average of the time-dependent term would be zero. But this would be true only for a homogeneous field. In an oscillating inhomogeneous field, like the one in Eqn. (2.2), a small average force will be left after the time average. This implies that it is possible to choose the drive frequency and voltages in such a way that the potential (2.2) will give rise to stable, approximately harmonic motion of the trapped ions. We can derive the result using the "pseudopotential" approximation, originally considered by Kapitsa [32].

2.1.2 Pseudopotential Approximation

For simplicity, we will only treat the motion in the x direction. The other directions can be treated analogously. The equation of motion for an ion with mass m and positive charge Q is

$$\ddot{x} = -\frac{Q}{m}\frac{\partial \Phi}{\partial x} = \frac{QV_0\alpha'}{m}\cos(\Omega_T t)x. \tag{2.3}$$

The pseudopotential approximation assumes that the complete motion, x_{tot}, consists of two different parts. One is called the *secular motion* x with large amplitude but low frequency; the other one is called the *micromotion* x_μ, which has small amplitude but oscillates at the high drive frequency Ω_T. These assumptions imply

$$x \gg x_\mu \quad \text{and} \quad \ddot{x} \ll \ddot{x}_\mu.$$

Eqn. (2.3) can be written as

$$\ddot{x} + \ddot{x}_\mu = \frac{QV_0\alpha'}{m}\cos(\Omega_T t)(x + x_\mu).$$

Applying those two approximations, we obtain a relation between the secular motion and micromotion:

$$\ddot{x}_\mu = \frac{QV_0\alpha'}{m}\cos(\Omega_T t)x,$$

$$x_\mu \approx -\left[\frac{QV_0\alpha'}{m\Omega_T^2}\cos(\Omega_T t)\right]x. \tag{2.4}$$

Substituting Eqn. (2.4) back into the original equation, we can cancel out the micro-motion term and reach an equation for just the secular motion:

$$\ddot{x} = \left[\frac{QV_0\alpha'}{m}\cos(\Omega_T t)\right]x - \left[\frac{Q^2V_0^2\alpha'^2}{m^2\Omega_T^2}\cos^2(\Omega_T t)\right]x. \tag{2.5}$$

Remembering that x oscillates at a frequency much smaller than the driving frequency Ω_T, we can average Eqn. (2.5) over one period of the rf. The cosine term averages to zero, and $\cos^2$ term averages to $1/2$. Thus we have

$$\ddot{x} = -\left(\frac{Q^2V_0^2\alpha'^2}{2m^2\Omega_T^2}\right)x. \tag{2.6}$$

This just is the equation of motion for a simple harmonic oscillator with frequency

$$\omega_x = \frac{QV_0\alpha'}{\sqrt{2}m\Omega_T}. \tag{2.7}$$

Combining Eqn. (2.7) and (2.4), we have the equation for the ion's x-component of motion when it is in an rf oscillating potential:

$$x_{\text{tot}} \propto \cos(\omega_x t)\left[1 - \frac{QV_0\alpha'}{m\Omega_T^2}\cos(\Omega_T t)\right]. \tag{2.8}$$

We see from Eqn. (2.8) that a charged particle indeed is confined by the oscillating harmonic potential.

2.1.3 Mathieu Equation

Now we add a static voltage term to Eqn. (2.2):

$$\Phi(x,y,z,t) = U_0\frac{1}{2}(\alpha x^2 + \beta y^2 + \gamma z^2) - V_0\cos(\Omega_T t)\frac{1}{2}(\alpha' x^2 + \beta' y^2 + \gamma' z^2). \tag{2.9}$$

In the x direction, the equation of motion becomes

$$\ddot{x} = -\frac{Q}{m}\frac{\partial\Phi}{\partial x} = -\frac{Q}{m}[U_0\alpha - V_0\cos(\Omega_T t)\alpha']x. \tag{2.10}$$

In terms of the dimensionless parameters

$$\xi = \frac{\Omega_T t}{2}, \quad a_x = \frac{4QU_0\alpha}{m\Omega_T^2}, \quad q_x = \frac{2QV_0\alpha'}{m\Omega_T^2}, \tag{2.11}$$

Eqn. (2.10) can be written as

$$\frac{d^2x}{d\xi^2} + [a_x - 2q_x\cos(2\xi)]x = 0. \tag{2.12}$$

Eqn. (2.12) is called the Mathieu equation and the solutions are well described in the mathematical physics books [33, 34]. The Mathieu equation has stable and unstable solutions. The stability depends only on the parameters (a_x, q_x) and not on the initial conditions of the ion's motion. The zones of stability for small values of (a_x, q_x) are shown in Fig. 2.1. The stable region that contains the point ($a_x = 0$, $q_x = 0$) is called the lowest stability region. The traps relevant to experiments mostly work inside the lowest stability region.

The ion's trajectory $x(t)$ in the case $(|a_x|, q_x^2) \ll 1$ can be found to be [20]:

$$x(t) \approx 2A\cos(\omega_x t)[1 - \frac{q_x}{2}\cos(\Omega_T t)], \tag{2.13}$$

$$\omega_x = \frac{\beta_x}{2}\Omega_T \approx \frac{\Omega_T}{2}\sqrt{\frac{q_x^2}{2} + a_x}, \tag{2.14}$$

where A is the amplitude of the oscillation.

Eqn. (2.13) agrees with Eqn. (2.8) when the static voltage is set to zero. As we discussed in the pseudopotential approximation, the ion's motion can be broken into two parts: the *secular motion* and the *micromotion*. The secular motion is the motion of an ion trapped in a harmonic oscillator with trap frequency $\omega_x \ll \Omega_T$. We can write the trap frequency explicitly as:

$$\omega_x^2 = \frac{1}{2}(\frac{QV_0\alpha'}{m\Omega_T})^2 + \frac{QU_0\alpha}{m} = (\omega_x)_{rf}^2 + \text{sign}(\alpha)(\omega_x)_s^2, \tag{2.15}$$

with

$$(\omega_x)_{rf} = \frac{|QV_0\alpha'|}{\sqrt{2}m\Omega_T} \quad \text{and} \quad (\omega_x)_s = \sqrt{\frac{|QU_0\alpha|}{m}}.$$

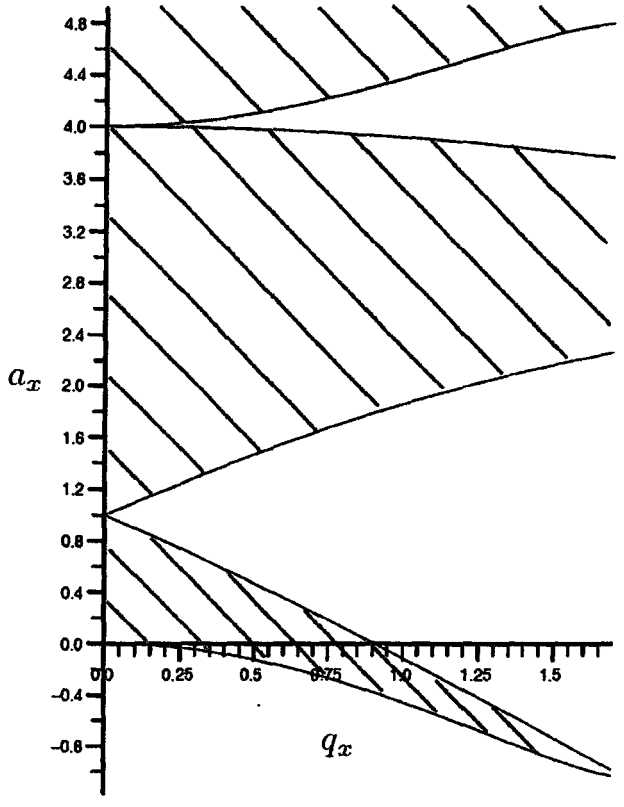

Figure 2.1: Stability diagram for Mathieu equation. The gray-hatched areas are the regions where the ion's motion is stable.

The trap frequency consists of two parts. One is related to the rf voltage. Its contribution to the trap frequency is always positive. The other part is related to the static voltage. Depending on the sign of α, it can enhance or reduce the trap frequency.

The micromotion is a much faster oscillation – its frequency is approximately the same as the drive frequency Ω_T*. The amplitude of the micromotion is proportional to the instantaneous displacement of the ion from the position where rf field is zero. From Eqn. (2.13), we see that the constant of proportionality is $|q_x|/2 \ll 1$, so

*The frequencies are the same in the pseudopotential approximation. The exact micromotion frequency differs from the drive frequency if we solve the Mathieu equation [20].

the micromotion amplitude is much smaller than that of the secular motion in the approximation that the trap is truly quadratic. Micromotion has several adverse effects; it can broaden the line shapes of the atomic transition, introduce significant Doppler shifts, and shorten the ions' lifetime without laser cooling. Methods to detect and minimize micromotion can also be found in Ref. [35].

2.2 Linear RF Ion Trap

Due to their strong Coulomb interaction, if there are several ions in an ion trap, they tend to displace each other. As shown in Section 2.1, the ions which are away from the rf null will experience enhanced micromotion. For this reason, we turn to the linear rf trap (see Fig. 2.2). Basically, a linear rf trap is a two-dimensional rf trap extended along a line, so there is a line where the rf field is zero instead of one point. The linear rf trap confines ions radially in an oscillating quadratic electric field created by the rf voltage applied to four parallel electrodes with hyperbolic surfaces. In the axial direction, the ions are confined by a static potential created by the voltage applied to the static-potential electrodes at both end of the trap (not shown in Fig. 2.2). The ions sit at or near the nodal line of the rf field.

2.2.1 Radial Trapping

In this section, we will focus on the radial confinement of the linear rf trap, which is related to the rf voltage. The geometric factors for rf trapping obey

$$\alpha' \approx -\beta', \qquad |\gamma'| \ll |\alpha'|,$$

where we have chosen the nodal line of the rf field as the z axis. $|\gamma'|$ will be zero if the electrodes have infinite length.

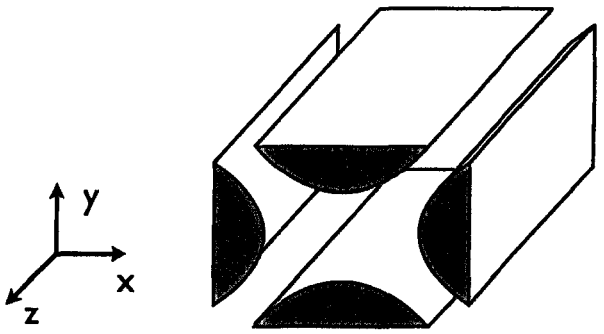

Figure 2.2: The electrode structure for a linear rf trap. The static-potential electrodes which confine ions in the z direction are not shown.

From Eqn. (2.15), we can see the trap frequency due to the rf part is proportional to the magnitude of α'. A large value of $|\alpha'|$ will give a larger trap frequency with fixed rf voltage and drive frequency, so the ions can be confined in a smaller region of space. In this case, we say the trap is *strong* in the radial direction. Our goal is to design a strong trap.

In order to generate a perfect quadratic potential distribution, the surfaces of the electrodes should be hyperbolic. Practically, it is very difficult to construct electrodes with hyperbolic surfaces, so people use round rods to build traps. Near the trap centre, the difference in potential between traps with hyperbolic surfaces and round surfaces is negligible.

A popular trap design consists of four parallel rods arranged with their axial centres on a square. This design has been used in many ion trap experiments and is well-described in Refs. [28, 29]. Because the ground rods are in the proximity of the

trap centre, the curvature of the electric field lines is large near the trap centre (see Fig. 2.3(a)), which gives a large value of $|\alpha'|$. The disadvantage of this design is the positioning of the rods. The centres of the four rods should stay exactly on a square, which offers manufacturing challenges, especially when working with a millimeter-size trap. For this reason, a simpler configuration might be preferable.

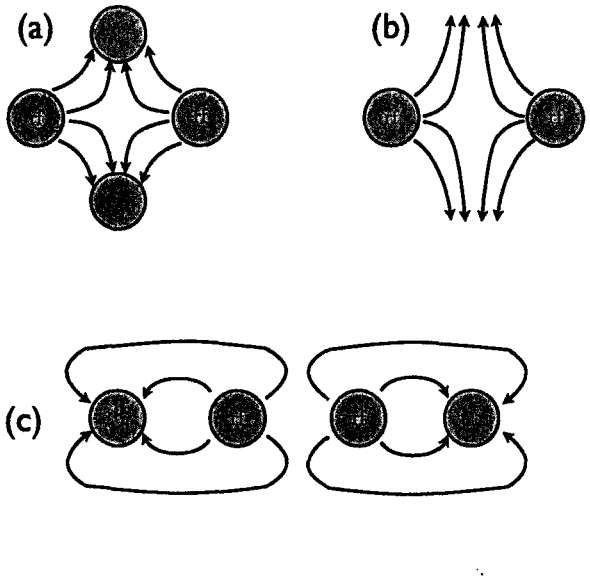

Figure 2.3: (a) Square design. (b) Paul-Straubel design. (c) In-line design.

Inspired by the Paul-Straubel design [36], which removes the end-cap electrodes and keeps only the ring electrodes in a 3-D rf trap, we considered removing the two ground rods. However such a trap has a small value of $|\alpha'|$. As shown in Fig. 2.3(b), the electric field lines near the trap centre go to the infinity in a "flat" manner.

In order to curve the electric field lines more, we can put ground rods in the plane of the rf rods, as shown in Fig. 2.3(c). Since the centres of the four rods stay along a line, we call this configuration the "in-line design". The in-line design has a larger value of $|\alpha'|$ than the trap without ground rods, and the geometry is simpler than the

square design. This geometry could also be useful for a micromachined trap [37, 38, 39] constructed like a strip-line.

We did some numerical calculations of $|\alpha'|$ for different electrode configurations. These calculations are described in Section 2.3.3. The results are shown in Fig. 2.4. We see that $|\alpha'|$ of the in-line design is less than that of the square design, but greater than that of the Paul-Straubel design.

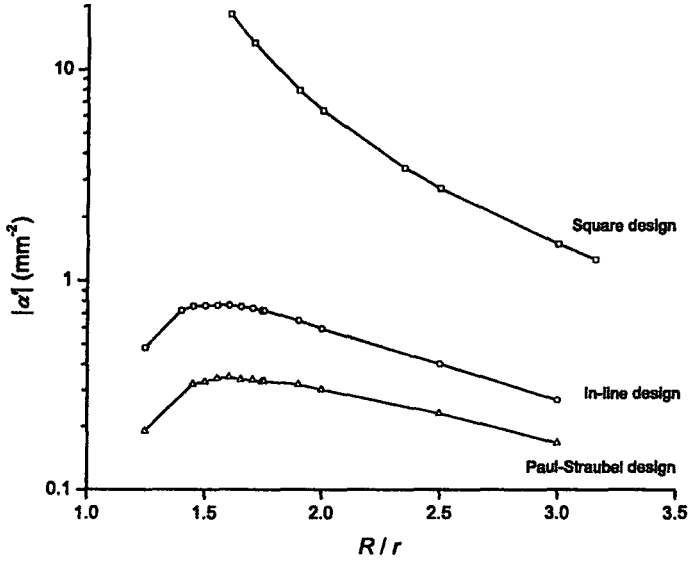

Figure 2.4: The geometric factor $|\alpha'|$ for different electrode configurations. R is the distance from the trap centre to the centre of the rf rod, and r is the radius of the rods. All the calculations are done with r= 0.395 mm.

2.2.2 Axial Trapping

The axial trapping is provided by the static-potential electrodes. If the ion is positively charged, the geometric factor γ needs to be positive. Since $\alpha + \beta + \gamma = 0$,

either α or β is negative or they are both negative. Therefore, the geometric factors related to the static voltages have the properties:

$$\alpha < 0 \quad \text{or} \quad \beta < 0, \quad \gamma > 0.$$

From Eqn. (2.15), the addition of the static potential will weaken the trap frequency in the radial directions because of the negative sign of α or β. For the axial trapping, we need the trap to have a large value of γ and relatively small values of α and β.

The static-potential electrodes can have various configurations. They can be separate sections of the trap rods [29], conically shaped electrodes [40] or parallel plates [41] at both ends of the trap, and rods or needles inserted into the trapping region along the trap axis [28, 42]. These configurations are suitable for both the square design and the in-line design.

There is an elegant configuration for the square design [31], which uses tube electrodes slipped over the ground rods (see Fig. 2.5). The tube electrodes are insulated from the rods by polyimide tubes. This configuration is easy to construct and there is no need for extra mounts for the tube electrodes. We will call this design a "square trap" in the rest of this thesis.

For the in-line design, we can take advantage of the fact that the rf rods and ground rods are in a plane, and use four additional rods as static-potential electrodes (see Fig. 2.6). We will simply call this design an "in-line trap".

2.3 Trap Design

There are two sets of parameters we can control in the trap design: one is the geometric parameters, which include the diameter of the rods, the separation between

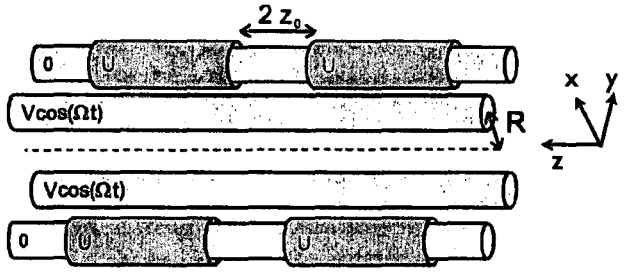

Figure 2.5: Schematic view of the square trap.

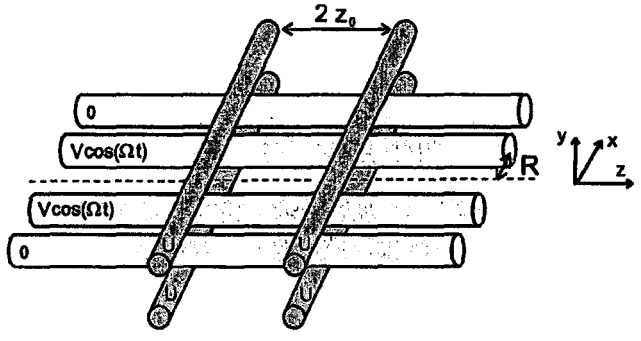

Figure 2.6: Schematic view of the in-line trap.

the rods and the configuration of the static-potential electrodes. These geometric parameters determine the value of the geometric factors α, β, γ and α', β', γ'. Another set is the operating parameters: the static voltage U_0, the rf voltage V_0 and the drive frequency Ω_T. Our job is to choose a reasonable combination of these parameters to optimize the performance of the trap.

We outline the main procedure for trap design in Fig. 2.7. First, we set the initial geometric parameters. The choices are limited by laser access and fluorescence collection. Once the geometric parameters are set, then the geometric factors are calculable using computer programs. These six factors determine the ranges of the operating parameters. Combined with the technical limits of the operating parameters, such as the maximum static and rf voltages we can apply, we can choose the operating parameters to maximize the trap frequency.

2.3.1 Choosing Geometric Parameters

When we reduce the size of the trap, we can get stronger trap frequencies with the same operating parameters. At the same time, standard machining tools are unusable if the size of the trap is less than about 0.1 mm. In real experiments, most traps have millimeter-scale dimensions.

The electrodes need to be mounted on insulating material to hold them in position. In order to use standard machining tools for the mounting holes, we choose the diameter of the electrode rods as 1/32".

The two traps we planned to build were the square trap and the in-line trap. They have relatively simple geometric configurations, and can be constructed nearly entirely with commercial, off-the-shelf components.

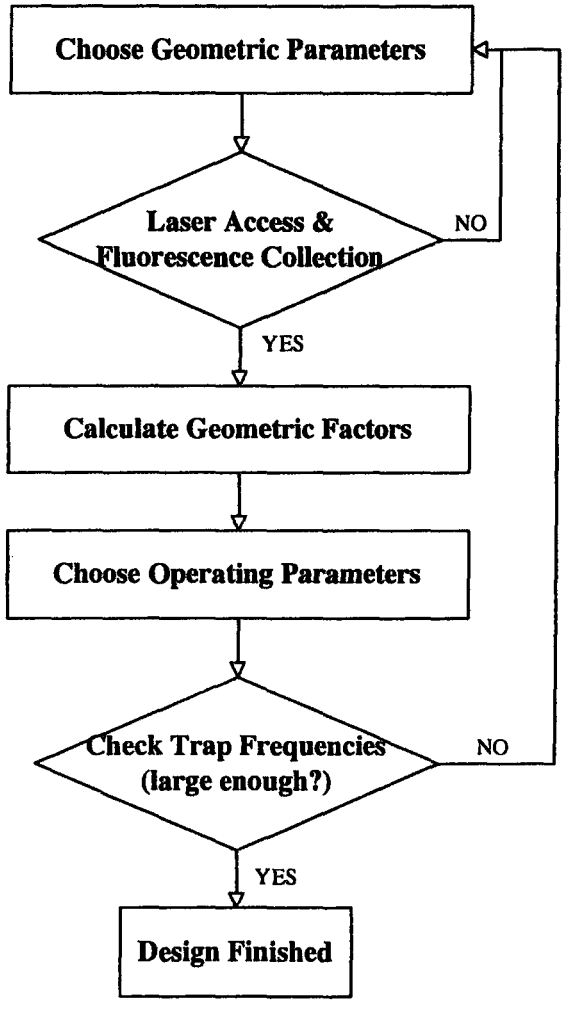

Figure 2.7: The main procedure for trap design.

2.3.2 Laser Access and Fluorescence Collection

In order to laser cool and manipulate the ions, we have lasers coming into the trap. The electrodes should be in a suitable position to ensure that we have laser access to the trapped ions.

To image the ions, a lens is positioned near the trap centre to collect the ions' fluorescence. In principle, we would like to image using $f/1$ lenses, which have a large collecting angle at a not-unreasonable price. The half angle of the $f/1$ lenses is about 30°, so we cannot put the rods too close to each other, or they will block the fluorescence.

For the square trap, the arrangement is straightforward. The lasers come in from one side of the trap and the fluorescence is collected in the direction perpendicular to the incoming lasers. This is shown in Fig. 2.8.

For the in-line trap, a natural setup is to have lasers input from one side of the trap and to collect fluorescence on the other side, as shown in Fig. 2.9(a). However, the laser will shine directly onto the detector in this setup, so we prefer to input lasers and collect fluorescence in two perpendicular directions. A solution is to tilt the whole structure of the in-line trap as shown in Fig. 2.9(b).

2.3.3 Computing Geometric Factors

Once we choose a set of geometric parameters, we need to determine the values of α, β, γ and α', β', γ'. For a complex electrode configuration, there is no analytic solution, so we need computer programs which can calculate the potential distribution with specified boundary conditions.

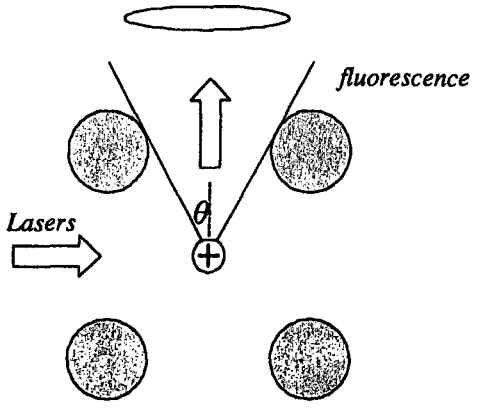

Figure 2.8: The electrode structure for the square trap.

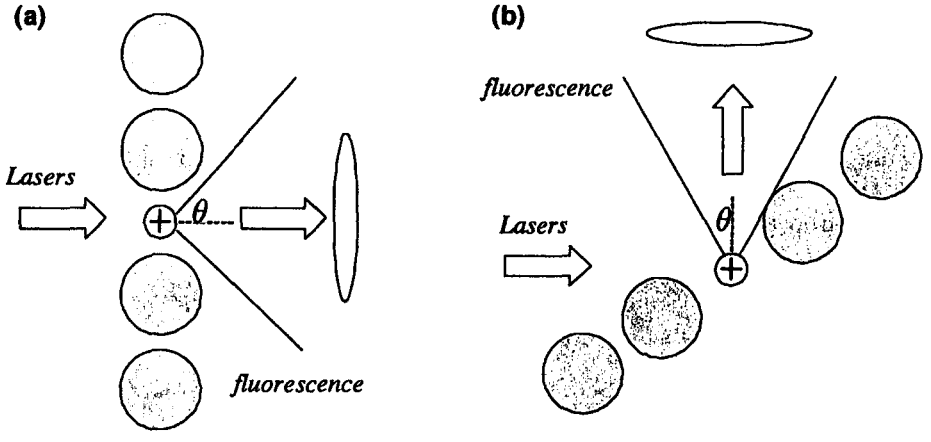

Figure 2.9: The electrode structure for the in-line trap. (a) The directions of the laser beams and fluorescence collection are opposite. (b) The directions are perpendicular to each other.

We have used two different programs during our design. The first one is EPM (Electric Potential Modeller). It was written by Peter Klages, one of the summer students in our group. This program uses a Finite-Difference Method [43, 44] to solve the Laplace equation. This method first divides space into equally spaced points and assigns the initial potential for each point, then uses an iteration method to reach the final solution. A single iteration consists of going through each point in space and averaging the potentials of the nearest points (six points for the 3-D model and four points for the 2-D model). This method uses the fact that the potential is a harmonic function of the space point; thus the potential value at one point is equal to the average of the potential values of all the neighboring points. The accuracy of the result depends on the number of points. The more points used in the calculation, the closer the values are to the analytical solution values. However, the run time increases dramatically when a large number of points are used. For this reason, this program is only suitable for 2-D simulations.

When using the EPM program, an auxiliary boundary has to be set to enclose all the electrodes. This boundary is set to zero potential and represents infinity. The size of this boundary is very crucial. If the size is too small, this boundary will affect the potential distribution; if the size is too large, it may take weeks to finish one simulation.

The second program is CPO[†] (Charged Particle Optics) and it is commercial software. CPO uses a more powerful Boundary Element Method [45]. This method is based on the fact that a system with specified potential distribution on the boundary is equivalent to a system of charge distribution on the boundary which produces the same potential distribution. Charges will only appear on the surfaces of the conducting electrodes when potentials are applied. These surface charges are the

[†]CPO Ltd, Manchester, UK. http://www.electronoptics.com

sources of all the potentials and fields in the free space. In the CPO program, the electrodes are effectively replaced by the surface charges and the potential can be calculated from the surface charges. It is not necessary to create an artificial boundary enclosing the electrodes, like the one required in the Finite-Difference Method. This program is fast and suitable for 3-D simulations.

2.3.4 Choosing Operating Parameters

In this section, we will address the question: given a trap design with specified geometric factors $(\alpha, \beta, \gamma, \alpha', \beta', \gamma')$, which combination of U_0, V_0 and Ω_T can we use? From Eqns. (2.11), we know that a_x and q_x are determined by U_0, V_0 and Ω_T. Once we decide the region of (a_x, q_x) we will work with, then we know the region of the operating parameters.

(I) Stability diagram

The stability of the ion is determined by the stability diagram of the corresponding Mathieu equation. The ratios between q_y and q_x, a_y and a_x are fixed for a given set of geometric factors, so we can map the y-stability diagram to a plot with (q_x, a_x) axes. The situation is similar for the z direction. Since $\gamma' \ll \alpha'$ for a linear trap, we have the relation $q_z \ll q_x$ for the same dc voltage. So when q_x approaches the right boundary of the stability region, q_z is still well inside its stability region. This implies that in the (q_x, a_x) plot, the z-stable region is elongated along the abscissa.

The common part of the lowest x-, y- and z-stable regions is shown in Fig. 2.10 and Fig. 2.11 for the square trap and the in-line trap, respectively. In the region enclosed by the lines with different colors, the ion's trajectories are stable in three directions.

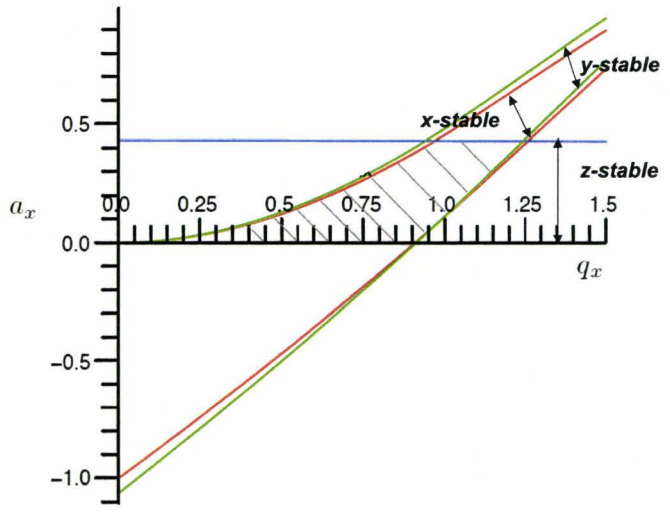

Figure 2.10: Stability diagram for the square trap. Red: x-stable. Green: y-stable. Blue: z-stable. Notice one of the blue lines coincides with the q_x axis.

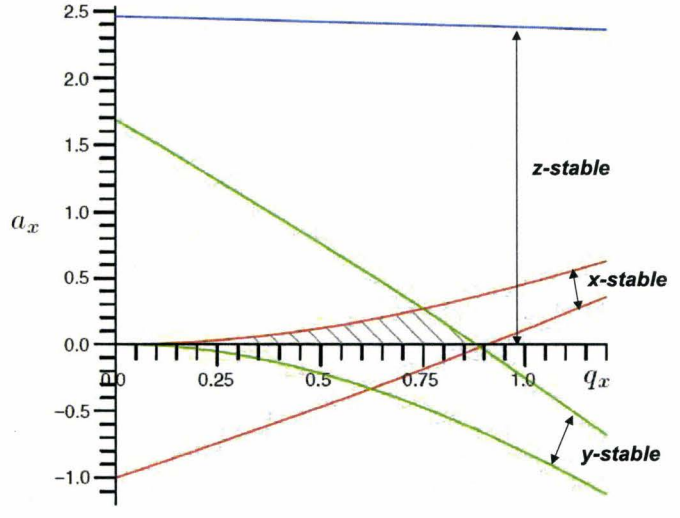

Figure 2.11: Stability diagram for the inline trap. Red: x-stable. Green: y-stable. Blue: z-stable. Notice one of the blue lines coincides with the q_x axis.

For the square trap, the x- and y-stable regions nearly coincide with each other. This is because α and β have the same signs, so the Mathieu equations in the x and y directions have the same form. For the in-line trap, the situation is different since α and β have opposite signs. The stable region of the in-line trap has a triangular shape.

The ion is unstable for most of the part $a_x < 0$ because the negative dc voltage will dispel the positive ion along the axial direction. When we increase the dc voltage to a certain point, in one of the radial directions or both, the dc contribution is negative and its value is greater than the rf contribution (see Eqn. (2.15)). So the trap is also unstable. This sets the upper z-stable boundary in Fig. 2.10 and Fig. 2.11.

(II) Alignment direction of the ions

When trapping several ions, we want the ions to form a string along the z-axis of the trap, instead of a zig-zag structure. This requires the trap frequency in the z direction to be less than that in the x or y directions:

$$\omega_x > s\omega_z, \tag{2.16}$$

where s is an anisotropy parameter depending on the number of trapped ions. For three ions, we can set $s = 2.6$ [46, 47, 48].

Eqn. (2.16) can be written in terms of the dimensionless parameters a and q:

$$\frac{q_x^2}{2} + a_x > s^2 \left(\frac{q_z^2}{2} + a_z \right).$$

The parameters in the x and z direction can be related using the geometric factors, which gives us:

$$a_x < \frac{1}{2} \frac{|\alpha|}{|\alpha'|^2} \frac{|\alpha'|^2 - s^2|\gamma'|^2}{|\alpha| + s^2|\gamma|} q_x^2. \tag{2.17}$$

This equation corresponds to the region below the blue line in Fig. 2.12 and Fig. 2.13.

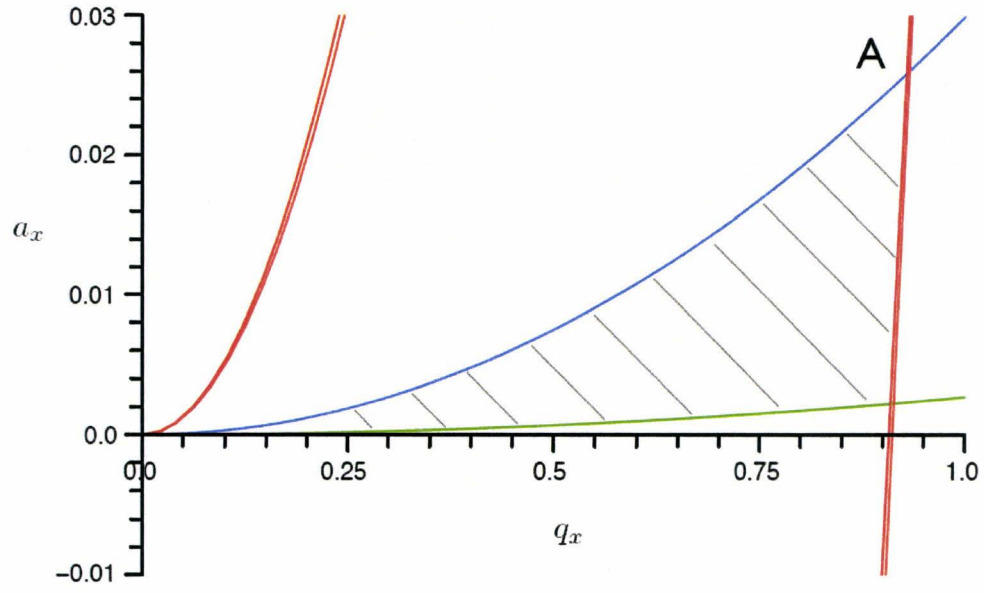

Figure 2.12: a_x-q_x diagram for the square trap. The area between the red lines is the region where ion's motion is stable in all directions. The area below the blue line is the region where $\omega_x > s\omega_z$. The area above the green line is the region where $(\omega_z)_{rf} < t(\omega_z)_s$. We can choose the parameters a_x and q_x from the gray-hatched area.

(III) RF trapping in the z direction

Because of the presence of static-potential electrodes and the limited length of the rods in the axial direction, the ions will experience rf potential in the z direction. In the z direction, the contribution to the trap frequency due to rf voltage should be much less than that due to static voltage:

$$(\omega_z)_{rf} < t(\omega_z)_s, \tag{2.18}$$

where t is a figure-of-merit parameter we choose in running the calculation. Usually we set t to be 0.15. If the rf trapping is large, the ions away from the trap centre will have a large amplitude of micromotion and we lose the advantages of the linear trap.

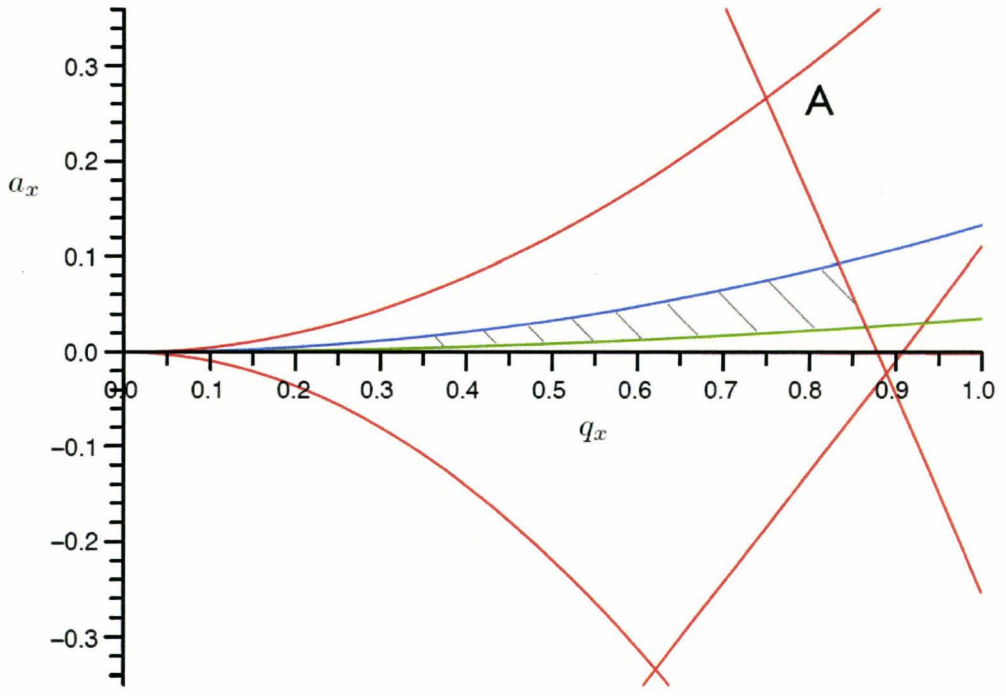

Figure 2.13: a_x-q_x diagram for the in-line trap. The area enclosed by the red lines is the region where ion's motion is stable in all directions. The area below the blue line is the region where $\omega_x > s\omega_z$. The area above the green line is the region where $(\omega_z)_{rf} < t(\omega_z)_s$. We can choose the parameters a_x and q_x from the gray-hatched area.

Writing Eqn. (2.18) in terms of the parameters a_x and q_x, we get

$$a_x > \frac{1}{2t^2}\frac{|\alpha||\gamma'|^2}{|\alpha'|^2|\gamma|}q_x^2. \tag{2.19}$$

This equation corresponds to the region above the green line in Fig. 2.12 and Fig. 2.13.

One important remark is that for a given set of geometric parameters, the minimum value of t is determined by Eqn. (2.17) and (2.19)

$$t_{\min} = \left(\frac{|\gamma'|^2}{|\gamma|}\frac{|\alpha| + s^2|\gamma|}{|\alpha'|^2 - s^2|\gamma'|^2}\right)^{1/2}. \tag{2.20}$$

If $t < t_{\min}$, the green line will be above of the blue line, then there will be no (a_x, q_x) values which satisfy both Eqn. (2.16) and Eqn. (2.18).

(IV) Operating Parameters

From the discussion above, we know that the gray-hatched regions in Fig. 2.12 and Fig. 2.13 are the (a_x, q_x) values we can work with. When we choose the operating parameters, we need to make sure the values of a_x and q_x are inside the working region.

There are also some practical constraints to which we need to pay attention when we choose the operating parameters. First, the maximum rf voltage and static voltage we can apply are about 1000 V and 300 V, respectively. They are limited by the breakdown voltage of the insulating material. Large rf voltages will cause closely spaced electrodes to discharge, even if the electrodes are insulated by the polyimide or vacuum. Second, the rf voltage is created by a helical resonator, so the drive frequency cannot be changed unless we change the helical resonator. We are only free to change V_0 and U_0 during the experiments.

Once we know the maximum rf and static voltages we can work with, we can use these values as point A in Fig. 2.12 and Fig. 2.13 to calculate Ω_T. By changing the values of V_0 and U_0, we have full access to the whole working region.

2.3.5 Checking Trap Frequencies

At this stage, all the parameters have been set and the trap frequencies can be calculated by using Eqn. (2.15). We find that the radial trap frequencies (ω_x and ω_y) are usually greater than 2 MHz, and the axial trap frequency ω_z is generally the bottle neck for the trap performance. If this is the case, we need to come back and change some of the geometric parameters and repeat the whole process again until the axial trap frequency is reasonably large (on the order of 1.0 MHz).

The parameters we plan to use and the corresponding trap frequencies are shown in Table 2.1 and Table 2.2.

Diameter of the rod $2r$	0.79 mm
Distance between the two rf rods $2R$	2.0 mm
Length of the rf and ground rods	60 mm
Inner diameter of the tube electrode	0.88 mm
Outer diameter of the tube electrode	1.05 mm
Distance between the two tube electrodes $2z_0$	3.0 mm
Length of the tube electrode	10 mm
Static voltage U_0	300 V
RF voltage V_0	1000 V
Drive frequency $\Omega_T/2\pi$	25.02 MHz
$\omega_x/2\pi$	8.009 MHz
$\omega_y/2\pi$	7.949 MHz
$\omega_z/2\pi$	1.684 MHz

Table 2.1: Parameters and trap frequencies for square trap.

Diameter of the rod $2r$	0.79 mm
Distance between the two rf rods $2R$	2.0 mm
Length of the rf and ground rods	60 mm
Separation of static rods in z direction $2z_0$	5.0 mm
Separation of static rods in x direction	0.9 mm
Length of the static rod	10 mm
Static voltage U_0	217 V
RF voltage V_0	1000 V
Drive frequency $\Omega_T/2\pi$	13.25 MHz
$\omega_x/2\pi$	2.013 MHz
$\omega_y/2\pi$	4.539 MHz
$\omega_z/2\pi$	1.007 MHz

Table 2.2: Parameters and trap frequencies for in-line trap

During the design work, we tried several different static-potential electrodes configurations. One uses rods inserted into the trapping region along the z axis. For this configuration, $(\omega_z)_{rf}$ is almost the same size as $(\omega_z)_s$, so it is difficult to trap several ions without introducing large micromotion.

Another configuration we considered was to use two conducting plates perpendicular to the four parallel rods. In order to produce a large value of ω_z, these two

plates have to be very close to each other. However, when the plates are near the trap centre, it is difficult to have laser access to the trapped ions.

For the in-line design, we also considered putting tube electrodes over the ground rods. This configuration has a very small value of ω_z. Another alternative is to use rectangular shaped strips as static-potential electrodes instead of rods. This design has similar properties to the in-line design.

Chapter 3

Theory of Trapped Two-Level Atoms Coupled to Light Fields

In order to implement quantum computation, a physical system has to meet several stringent requirements. In 2000, DiVincenzo proposed five criteria for physical system to perform quantum computation [49]:

1. A scalable physical system with well characterized qubits.
2. The ability to initialize the state of the qubits to a simple fiducial state, such as $|000\ldots\rangle$.
3. Long relevant decoherence times, much longer than the gate operation time.
4. A universal set of quantum gates.
5. A qubit-specific measurement capability.

Several physical systems fully or partially satisfy the DiVincenzo criteria; examples include neutral atoms, molecules, cavity QED, quantum dots and many more [50]. Among them, trapped ions are now leading the race to realize quantum computation in a real physical system. In this chapter, we will use $^{25}Mg^{+}$ as an example to discuss some of the techniques needed to perform quantum computation with trapped ions.

In $^{25}Mg^{+}$, we choose two ground-state hyperfine levels as our qubit. The decoherence time can be made extremely long by using two levels which are first-order

independent to magnetic field fluctuations. The ions will be laser cooled to near their ground state of motion, where the quantum nature of this motion starts to be significant. The qubit will be initialized using resonant ultraviolet laser beams, and detection will be achieved by collecting fluorescence emitted from the ion. Due to strong Coulomb coupling between ions, the motion of a string of trapped ions is a collective property of all the ions. This degree of freedom enables us to perform quantum gates between different atomic qubits. The coupling between the qubit states and motional states is induced through two-photon stimulated Raman transitions.

3.1 $^{25}Mg^{+}$ as a Qubit

Fig. 3.1 shows a simplified energy-level diagram of $^{25}Mg^{+}$. This species has only one valence electron so its spectrum is similar to that of hydrogen. The ground states are $1s^2 2s^2 2p^6 3s\ ^2S_{1/2}$. The nuclear spin $I = 5/2$ is responsible for the energy splitting between the two ground-state hyperfine manifolds $F = 2$ and $F = 3$.

The qubit is formed by two ground-state levels: $|^2S_{1/2}, F = 3, m_F = -3\rangle$ and $|^2S_{1/2}, F = 2, m_F = -2\rangle$, abbreviated by $|\downarrow\rangle$ and $|\uparrow\rangle$. They are separated by the hyperfine splitting of 1.79 GHz. The transition between the qubit states is dipole-forbidden, but we can couple them using two-photon stimulated-Raman transitions (see Section 3.5.2).

The first two excited states are $^2P_{1/2}$ and $^2P_{3/2}$. These levels are separated from each other by the fine structure splitting of 2.75 THz: the $^2S_{1/2} \leftrightarrow {}^2P_{1/2}$ transition lies at 280.35 nm whereas the $^2S_{1/2} \leftrightarrow {}^2P_{3/2}$ transition lies at 279.64 nm. Both transitions have radiative linewidth $\gamma/2\pi = 43$ MHz. The $^2P_{1/2}$ level, which has two sublevels $F \in \{2, 3\}$, has a hyperfine splitting ≈ 310 MHz. The $^2P_{3/2}$ hyperfine splitting is about 60 MHz; this level has four sublevels $F \in \{1, 2, 3, 4\}$.

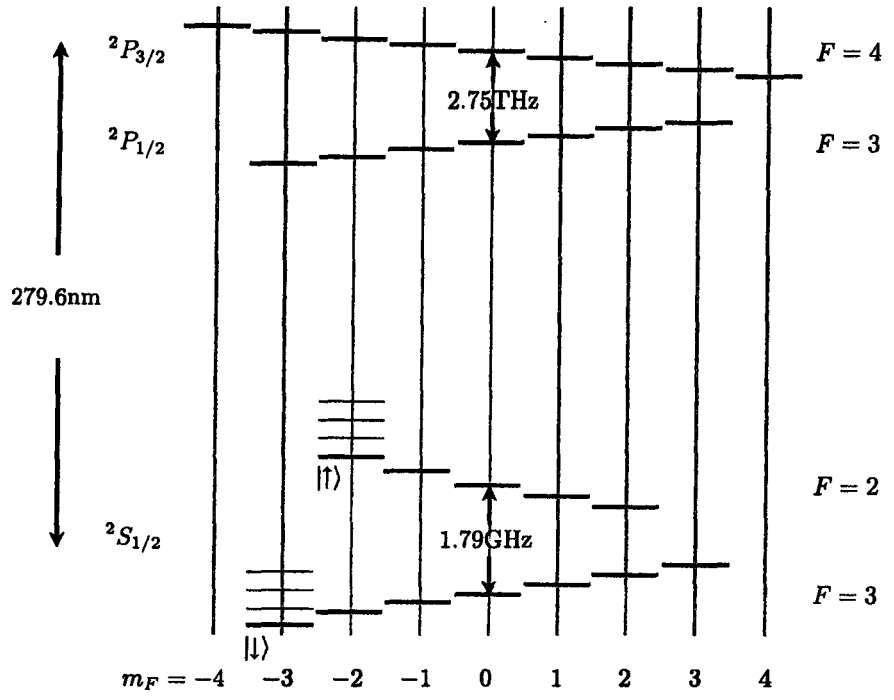

Figure 3.1: Atomic structure of $^{25}Mg^+$ (not to scale). Note that we have omitted hyperfine levels of $3p$ states that are not relevant to our experiments. $|\downarrow\rangle$ and $|\uparrow\rangle$ denote the qubit states. The motional energy levels are indicated for only the qubit states and only for a single mode.

When the ion is trapped in a harmonic potential, and laser-cooled to μK temperature, the kinetic energy of the ion becomes comparable to $\hbar\omega_i$, where ω_i is the trap frequency in the i-th direction. The ion's motion can be quantized and described by quantum harmonic oscillators: the motional eigenstates are characterized by quantum number n_i and the energy for n_i-th motional state is $(n_i + \frac{1}{2})\hbar\omega_i$. Each electronic state now has associated with it a ladder of motional eigenstates with the same energy spacing $\hbar\omega_i$ (See Fig. 3.1).

In a linear ion trap, the ions are strongly confined in the radial direction but loosely trapped in the axial direction. After the ions are cooled to the ground state in

all directions, the radial motion will seem to be frozen because small energy changes are not large enough to excite the radial motion. The motion along the axial direction is a collective property of the whole string of ions. We can use the axial motion to transfer the quantum information from one ionic qubit to another (see Section 3.5). So we will focus on ions' motion in the axial direction in the following sections.

3.2 Decoherence Time

One dominant source of decoherence is induced by fluctuating ambient magnetic fields [51, 52]. To solve this problem, we investigate the long-lived qubit states of $^{25}Mg^{+}$ which are first-order independent of magnetic field fluctuations [53, 54].

Degeneracy of the hyperfine levels is broken by applying a quantization magnetic field B. When the magnetic field is weak, the interaction of the atomic electrons with the external magnetic field can be treated as a perturbation. The Zeeman shift for different m_F level is [55]

$$\Delta E = g_F \mu_B B m_F, \tag{3.1}$$

where g_F is the Landé g-factor and μ_B is the Bohr magneton. The Landé g-factors for the qubit levels $|\downarrow\rangle$ and $|\uparrow\rangle$ are $1/3$ and $-1/3$ respectively. The energy splitting between them $\Delta E \approx 2.3$ MHz/Gauss.

When the magnetic field is strong, the exact energy of each Zeeman level can be calculated by diagonalizing the Hamiltonian in the $|m_I, m_J\rangle$ basis. This work has been done in-group by Laura Toppozini [22]. Fig. 3.2 shows the hyperfine levels structure of the $^2S_{1/2}$ state of $^{25}Mg^{+}$ as a function of quantization magnetic field.

We choose our qubit to be $|^2S_{1/2}, F = 3, m_F = -3\rangle$ and $|^2S_{1/2}, F = 2, m_F = -2\rangle$ states. We can see that fluctuating magnetic fields will cause significant decoherence: the qubit transition depends linearly on the magnetic field with a coefficient of

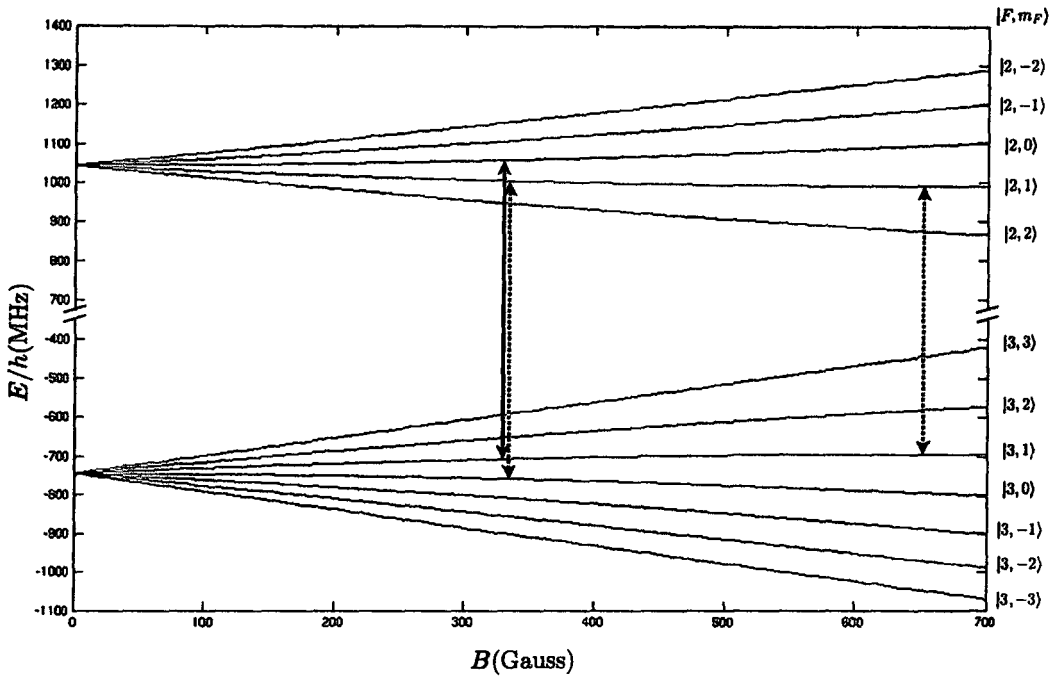

Figure 3.2: Hyperfine level structure of the $^2S_{1/2}$ state of $^{25}Mg^+$. The solid arrow indicates the magnetic-field-independent transition at 325 Gauss; the dashed arrows indicate other useful field-independent transitions at 332 Gauss and 653 Gauss. Figure courtesy of Laura Toppozini.

approximately 0.78 MHz/Gauss. Therefore, for a typical room magnetic field fluctuation of 10^{-3} Gauss, the qubit superposition will be dephased (to a phase uncertainty of 1 rad) in 200 μs.

A natural choice of field-independent transition would be $|F = 3, m_F = 0\rangle \leftrightarrow |F = 2, m_F = 0\rangle$. It has no linear Zeeman shift at zero magnetic field, and the second-order dependence is $(-243$ Hz/Gauss$^2)$ B^2. Coherence times exceeding 10 minutes in $^{171}Yb^+$ have been observed using this type of transition [56]. Unfortunately, the Zeeman sublevels are degenerate at zero magnetic fields.

There are several ground-state choices for magnetic-field-independent transitions in $^{25}Mg^{+}$ at nonzero field, and we will limit ourselves to those in which first-order independence occurs at relatively low magnetic field. Those transitions are listed in Table 3.1. The values are obtained by fitting the energy difference between two ground-state hyperfine levels using a quadratic function.

Upper State	Lower State	B_0 (Gauss)	2nd-order coefficient (Hz/Gauss^2)
$\|F=2,m_F=0\rangle$	$\|F=3,m_F=1\rangle$	325	-239
$\|F=2,m_F=1\rangle$	$\|F=3,m_F=0\rangle$	332	-240
$\|F=2,m_F=1\rangle$	$\|F=3,m_F=1\rangle$	653	-258

Table 3.1: First-order magnetic-field-independent hyperfine ground-state transitions in $^{25}Mg^{+}$.

Given random fluctuations of 10^{-3} Gauss, we expect superpositions of the first pair of qubit states in Table 3.1 to dephase in about 10 minutes. A coherence time of 2.5 seconds has been observed using a first-order magnetic-field-independent hyperfine transition in $^{117}Yb^{+}$ [57], and 10 seconds in $^{9}Be^{+}$ [54].

3.3 Initialization

An ion starts out in a thermal population of all $|F,m_F\rangle$ states. Initialization of the qubit state is done by optically pumping the electronic population into the $|\downarrow\rangle$ state. This is realized by shining two near-resonant laser beams on the ion, the Red Doppler and Repumper.

The Red Doppler (RD, see Fig. 3.3) is tuned to the $|\uparrow\rangle \leftrightarrow |^2P_{3/2}, F=4, m_F=-3\rangle$ transition. From the excited state, the ion can decay back to $|\uparrow\rangle$, to $|\downarrow\rangle$, or to $|^2S_{1/2}, F=3, m_F=-2\rangle$ state. In the latter case, we have to re-pump the ion back to the $|\downarrow\rangle/|\uparrow\rangle$ manifold. This is done by the Repumper (RP, see Fig. 3.4), resonant

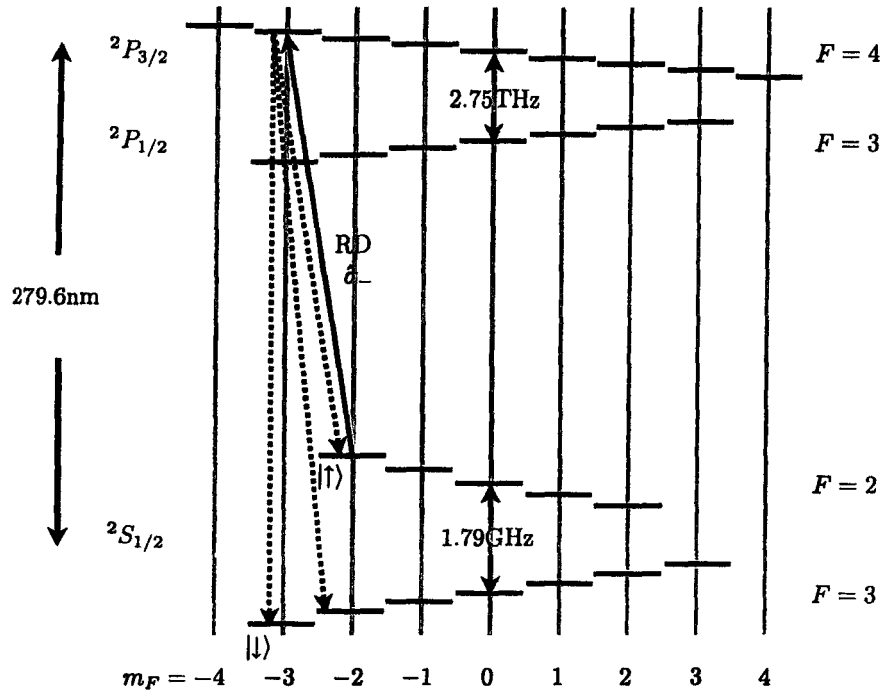

Figure 3.3: The Red Doppler (RD) beam couples $|\uparrow\rangle \leftrightarrow |^2P_{3/2}, F = 4, m_F = -3\rangle$.

with $|^2S_{1/2}, F = 3, m_F = -2\rangle \leftrightarrow |^2P_{1/2}, F = 3, m_F = -3\rangle$ transition, which optically pumps the ion back to the two-level system.

In typical operating conditions, the Zeeman-splitting of the ground-states is small compared to the natural linewidth, so the Red Doppler will couple all the $|^2S_{1/2}, F = 2\rangle$ levels to the $^2P_{3/2}$ states, and the Repumper will couple all the $|^2S_{1/2}, F = 3\rangle$ levels except $|\downarrow\rangle$ to the $^2P_{1/2}$ states. Since both beams are $\hat{\sigma}_-$-polarized, the m_F number will decrease by 1 when the ion absorbs a photon and excites to the $3p$ states. When the ion spontaneously decays back to the ground-states, the average change of m_F is 0. So the overall effect of one cycle is to reduce the m_F number by 1. After scattering several photons, the ion will be optically pumped to the dark state $|\downarrow\rangle$.

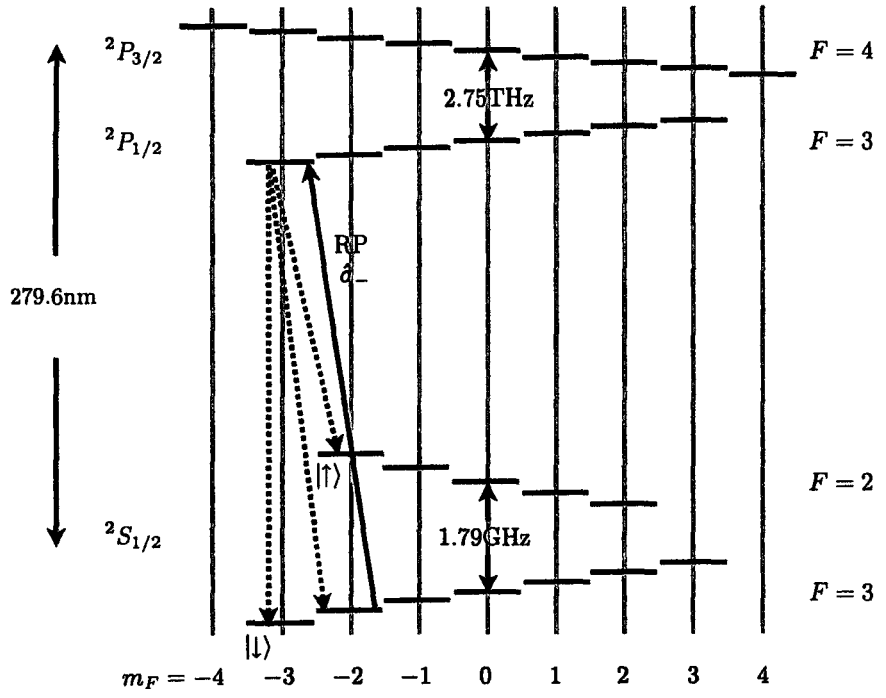

Figure 3.4: The Repumper (RP) couples $|^2S_{1/2}, F = 3, m_F = -2\rangle \leftrightarrow |^2P_{1/2}, F = 3, m_F = -3\rangle$.

3.4 Detection

3.4.1 Basic Detection Method

Detection is achieved with the Cycler beam (CYC, see Fig. 3.5), which drives a cycling transition $|\downarrow\rangle \leftrightarrow |^2P_{3/2}, F = 4, m_F = -4\rangle$. Once the ion is in $|^2P_{3/2}, F = 4, m_F = -4\rangle$, due to the selection rule $\Delta m_F = 0, \pm 1$, it can only decay back to $|\downarrow\rangle$. Thus, if the ion starts in the $|\downarrow\rangle$ state and the polarization of the Cycler is $\hat{\sigma}_-$, the ion will repeatly cycle between these two states, spontaneously emitting a large amount of fluorescence. A portion of the emitted photons, depending on the detection efficiency

of the imaging system (see Section 7.1), is collected with imaging optics and counted with a photon-counting device. The distribution of the photon counts should be a Poissonian.

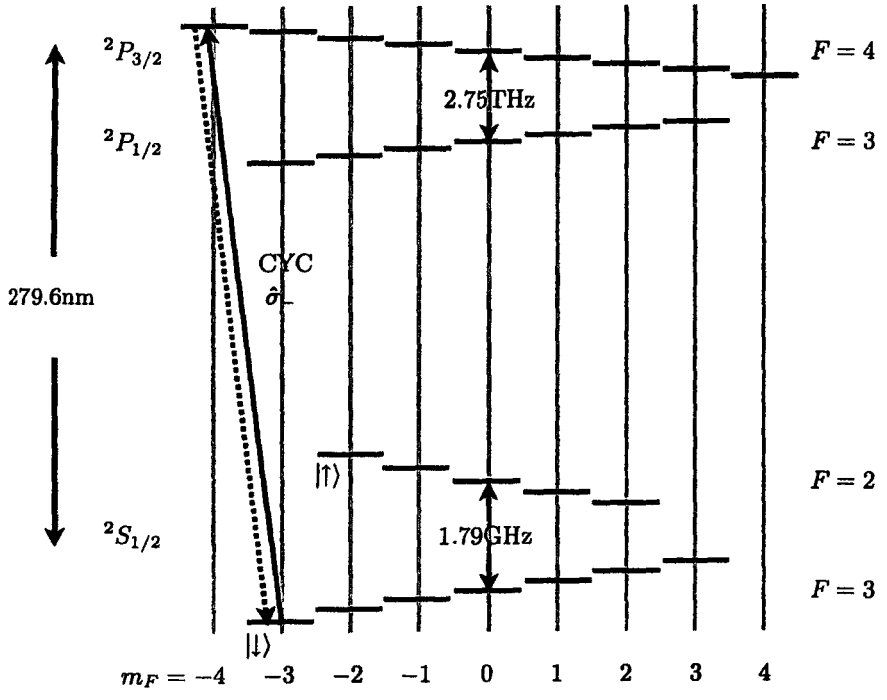

Figure 3.5: The Cycler (CYC) couples $|\downarrow\rangle \leftrightarrow |^2P_{3/2}, F = 4, m_F = -4\rangle$.

If we assume a detuning of δ and the laser polarization is $\hat{\sigma}_-$, the mean number of photons detected from the ion in $|\downarrow\rangle$ state is [58]

$$\bar{m}_0 = t_D \zeta \frac{s\frac{\gamma}{2}}{1 + s + (\frac{2\delta}{\gamma})^2}, \tag{3.2}$$

where t_D is the detection time, ζ is the photon detection efficiency, $\gamma/2\pi = 43$ MHz is the radiative linewidth of the $^2P_{3/2}$ state, and $s = I/I_{\text{sat}}$ is the laser saturation parameter. The saturation intensity is given by [59]

$$I_{\text{sat}} = \frac{h\pi c\gamma}{3\lambda^3} \approx 0.255\text{W/cm}^2 \quad (\text{for } \text{Mg}^+).$$

We typically run the experiments with $s \leq 1$.

In contrast, when the ion is in the $|\uparrow\rangle$ state, the laser is no longer resonant with the transition to any excited state. The nearest allowed transition is to $|^2P_{3/2}, F = 3, m_F = -3\rangle$ which is detuned by $\Delta = \omega_{\mathrm{HFS}} - \omega_{\mathrm{HFP}} \approx 1.7$ GHz, where ω_{HFP} is the hyperfine splitting of the $^2P_{3/2}$ states, so an ion in the $|\uparrow\rangle$ scatters almost no photons. Thus, we can determine the state of the qubit with high fidelity by applying the $\hat{\sigma}_-$-polarized Cycler and counting the number of photons that arrive at the detector.

In practice, two factors limit the detection fidelity. The first one is off-resonant pumping [60, 61]: since the ground-state hyperfine splitting is only about 43 times the linewidth of the excited state, spontaneous emission after off-resonant transition from $|\uparrow\rangle$ to the excited state can transfer population from $|\uparrow\rangle$ into the cycling transition. This is fundamentally due to the atomic structure of $^{25}Mg^+$ ion. The detection fidelity also depends on the degree to which Cycler beam is pure $\hat{\sigma}_-$. Since the hyperfine splitting in the $^2P_{3/2}$ state is negligible, any $\hat{\pi}$- and $\hat{\sigma}_+$-polarization of the Cycler will couple $|\downarrow\rangle$ to different excited states, from which the ion can decay to $F = 2$ manifolds. If this occurs the fluorescence ceases. We will discuss these two factors in the following sections.

3.4.2 Off-resonant Pumping

The energy levels relevant for our discussion are shown in Fig. 3.6. The frequency of the Cycler is tuned to the $|\downarrow\rangle \leftrightarrow |^2P_{3/2}, F = 4, m_F = -4\rangle$ transition and the laser polarization is pure $\hat{\sigma}_-$. Here we neglect the hyperfine splitting of $^2P_{3/2}$ states. The probability that the ion is driven from $|\uparrow\rangle$ to the other ground states is

$$\beta_1 |\langle f|e\rangle\langle e|^2 S_{1/2} F = 2, m_F = -2\rangle|^2,$$

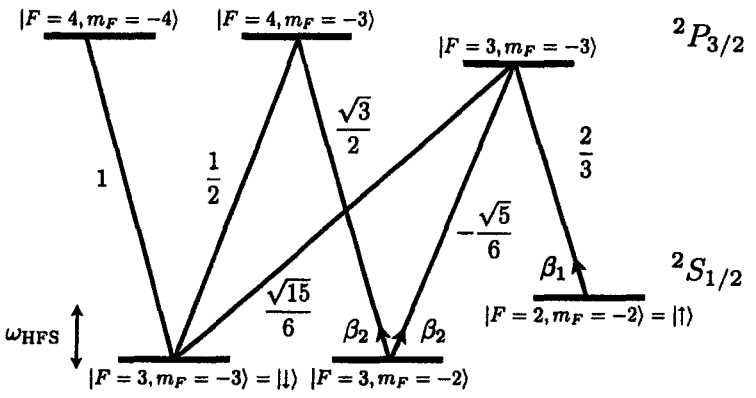

Figure 3.6: The energy levels relevant to off-resonant pumping. The lines connecting different levels represent the dipole-allowed transitions, and the numbers beside the lines are Clebsch-Gordon coefficients between the two connected levels.

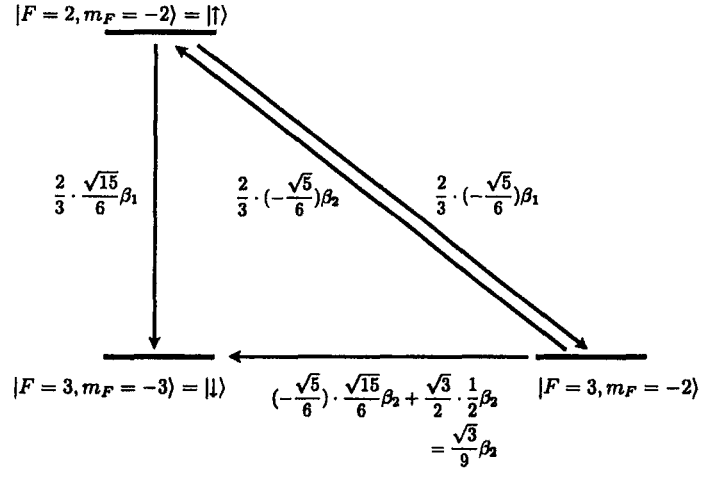

Figure 3.7: Simplified energy levels for off-resonant pumping. Only the ground-states are left here.

where $\langle\psi|\psi'\rangle$ is the Clebsch-Gordon coefficient between states $|\psi\rangle$ and $|\psi'\rangle$, $|e\rangle$ and $|f\rangle$ are the intermediate excited state and the final ground state, and β_1 is the off-resonant scattering rate given by

$$\beta_1 = \frac{s\frac{\gamma}{2}}{1+s+4(\frac{\omega_{\rm HFS}+\delta}{\gamma})^2} \approx s\frac{\gamma}{2}\Big(\frac{\gamma}{2\omega_{\rm HFS}}\Big)^2. \tag{3.3}$$

The approximation is made because $\omega_{\rm HFS} \gg \gamma, \delta$ and $(\omega_{\rm HFS}/\gamma)^2 \gg 1+s$.

The situation is the same when the ion starts in the $|^2S_{1/2}, F=3, m_F=-2\rangle$ state except the scattering rate is given by

$$\beta_2 = \frac{s\frac{\gamma}{2}}{1+s+(\frac{2\delta}{\gamma})^2}. \tag{3.4}$$

The Clebsch-Gordon coefficient can be evaluated from a formula derived from [62]:

$$\begin{aligned}\langle\psi|\psi'\rangle &= (-1)^{\frac{1}{2}q(1+q)+1+2F-m_F+I+J'+S+L'+J}\delta_{II'}\delta_{SS'} \\ &\times \sqrt{(2F+1)(2F'+1)(2J+1)(2J'+1)(2L+1)} \\ &\times \begin{pmatrix} F & 1 & F' \\ -m_F & q & m'_F \end{pmatrix} \begin{Bmatrix} J & F & I \\ F' & J' & 1 \end{Bmatrix} \begin{Bmatrix} L & J & S \\ J' & L' & 1 \end{Bmatrix},\end{aligned} \tag{3.5}$$

where $|\psi\rangle = |LSJIFm_F\rangle$ is the excited state and $|\psi'\rangle = |L'S'J'I'F'm'_F\rangle$ is the ground-state. $q = M_F - M'_F$ can only be $0, \pm 1$; this corresponds to the dipole selection rule $\Delta M_F = 0, \pm 1$. () and {} are 3-j symbols and 6-j symbols. Their values can be calculated using Mathematica or from tables in atomic physics books [63, 64].

Using the numbers shown in Fig. 3.6, we can eliminate the excited state levels, and get the simplified level structure of Fig. 3.7. An interesting point that can be made here is that starting from $|^2S_{1/2}, F=3, m_F=-2\rangle$ state, there are two paths to arrive in the $|\downarrow\rangle$ state. These two routes destructively interfere with each other.

Returning to the $|\uparrow\rangle$ state, we can write down the rate equation for the population using the numbers shown in Fig. 3.7:

$$\dot{P}_\uparrow = -\left[(\frac{\sqrt{15}}{9})^2\beta_1 + (\frac{\sqrt{5}}{9})^2\beta_1\frac{(\frac{\sqrt{5}}{9})^2\beta_2}{(\frac{\sqrt{5}}{9})^2\beta_2+(\frac{\sqrt{3}}{9})^2\beta_2}\right]P_\uparrow = -\frac{145}{648}\beta_1.$$

Thus, $P_\uparrow(t) = P_\uparrow(0)\exp(-\frac{145}{648}\beta_1 t)$. This equation describes the average dynamics of state $|\uparrow\rangle$; when we talk about one ion initially in $|\uparrow\rangle$, the probability it leaves $|\uparrow\rangle$ at time t_p is

$$p(t_p)\mathrm{d}t = \frac{1}{\tau_{p1}} e^{-\frac{t_p}{\tau_{p1}}}\mathrm{d}t, \tag{3.6}$$

where $\tau_{p1} = \frac{648}{145\beta_1}$.

To reiterate, when the ion is in the $|\uparrow\rangle$ state at $0 < t < t_p$, we see no photons. At some random time t_p the ion is off-resonantly pumped into the cycling transition. Then, we observe a Poissonian distribution with mean photon number

$$\bar{m} = \bar{m}_0(1 - \frac{t_p}{t_D}), \tag{3.7}$$

where $\bar{m}_0$ is given by Eqn. (3.2). We want to derive the probability distribution $\rho(\bar{m})$, which is the probability of one ion, initially in the $|\uparrow\rangle$ state, producing a Poissonian distribution of collected photons with mean $\bar{m}$. Here we follow the derivation from Ref. [60], Appendix A.

The probability distribution $\rho(\bar{m})$ is equal to the derivative of the cumulative distribution $F(\bar{m})$, which is the probability of detecting less than $\bar{m}$ photons:

$$F(\bar{m}) = \mathrm{Prob.}(M \leq \bar{m}) = \int_{M(t_p)<\bar{m}} p(t_p)\mathrm{d}t_p, \tag{3.8}$$

where M is the number of photons detected. From Eqn.(3.7), the domain of integration $M(t_p) < \bar{m}$ can be written as

$$t_p > (1 - \frac{\bar{m}}{\bar{m}_0})t_D.$$

Eqn. (3.8) becomes

$$F(\bar{m}) = \int_{t_p>(1-\frac{\bar{m}}{\bar{m}_0})t_D} p(t_p)\mathrm{d}t_p = e^{-\frac{t_p}{\tau_{p1}}(1-\frac{\bar{m}}{\bar{m}_0})}. \tag{3.9}$$

Then the probability distribution $\rho(\bar{m})$ can be calculated by differentiating $F(\bar{m})$:

$$\rho(\bar{m}) = \frac{\partial F(\bar{m})}{\partial \bar{m}} = \left(\frac{t_p}{\bar{m}_0\tau_{p1}}\right)e^{-\frac{t_p}{\tau_{p1}}(1-\frac{\bar{m}}{\bar{m}_0})} + e^{-\frac{t_p}{\tau_{p1}}}\delta(\bar{m}). \tag{3.10}$$

The integral is discontinued at $t_p = 0$ so there is a δ-function in the result.

The distribution $P_1(m)$ of collecting m photons can be written as a convolution of a Poissonian $P(m|\bar{m})$ with mean $\bar{m}$ and a probability distribution $\rho(\bar{m})$:

$$P_1(m) = \int P(m|\bar{m})\rho(\bar{m})\mathrm{d}\bar{m}. \tag{3.11}$$

Using the calculated probability distribution $\rho(\bar{m})$ and the well-known Poissonian distribution $P(m|\bar{m}) = \frac{e^{-\bar{m}}\bar{m}^m}{m!}$, we can calculate $P_1(m)$ from Eqn. (3.11):

$$P_1(m) = e^{-\frac{t_D}{\tau_{p1}}}\delta_{m,0} + \frac{t_D e^{-\frac{t_D}{\tau_{p1}}}}{\tau_{p1}\bar{m}_0 m!}\int_{\epsilon\to 0^+}^{\bar{m}_0} e^{(\frac{t_D}{\tau_{p1}\bar{m}_0}-1)\bar{m}}\bar{m}^m\mathrm{d}\bar{m}. \tag{3.12}$$

$P_1(m)$ can be re-expressed in terms of the incomplete Gamma function [33]:

$$P_1(m) = e^{\alpha_1\bar{m}_0}\left[\delta_{m,0} + \frac{\alpha_1}{(1-\alpha_1)^{m+1}}\mathcal{P}(n+1,(1-\alpha_1)\bar{m}_0)\right], \tag{3.13}$$

where

$$\alpha_1 = \frac{t_D}{\tau_{p1}\bar{m}_0} \quad \text{and} \quad \mathcal{P}(a,x) \equiv \frac{1}{(a-1)!}\int_0^x e^{-y}y^{a-1}\mathrm{d}y. \tag{3.14}$$

For a perfect scheme that discriminates $|\uparrow\rangle$ from $|\downarrow\rangle$, we would expect to observe no photons in detection time t_D when the ion starts in the state $|\uparrow\rangle$. This ideal case corresponds to $P_1(0) = 1$. The effect of the off-resonant pumping is to make $P_1(0)$ differ from unity:

$$P_1(0) = e^{-\alpha_1\bar{m}_0} = \exp(-\frac{t_D}{\tau_{p1}}\bar{m}_0), \tag{3.15}$$

where

$$\alpha_1 = \frac{145}{648\zeta}\left(\frac{\gamma}{2\omega_{\mathrm{HFS}}}\right)^2. \tag{3.16}$$

α_1 is calculated using Eqn.(3.3) and (3.14) in which we have assumed $s+(2\delta/\gamma)^2 \ll 1$ in (3.2).

For $^{25}Mg^+$, we have that $\alpha_1 \approx \frac{3.26\times10^{-5}}{\zeta}$. With the detection efficiency of our imaging system $\zeta \approx 3\times10^{-3}$ (see Section 7.1) and $\bar{m}_0 = 5$, we have $P_1(0) \approx 0.95$. This

is the upper limit to the accuracy of distinguishing $|\uparrow\rangle$ from $|\downarrow\rangle$ due to off-resonant pumping. One way to improve the state-detection efficiency is to use quantum information processing [65].

3.4.3 Polarization Impurity

Another factor limiting our detection fidelity is the polarization impurity of the cycler beam. An ion can be driven out of the cycling transition because of imperfect laser polarization. In our case, the dark states are the $F = 2$ manifold and once the ion falls into $F = 2$ manifold, the laser frequency is off resonant by ω_{HFS}. As before, the collected photon distribution will be a convolution of Poissonian and exponential distribution, but now reversed: at the beginning, the ion scatters photons at a rate β_2; then at some random time t_p, it is pumped into the dark states and emits no photons. Of course there is the possibility that the ion is pumped back to the cycling transition from the dark states, but it is a second-order effect so it can be neglected.

Similarly to Section 3.4.2, we can define the average leak time from the cycling transition into the dark state as τ_{p2}, and derive $P_2(m)$, the probability of observing m photons in a detection time t_D, given that the ion is in the state $|\downarrow\rangle$ at $t = 0$. The derivation is similar to the one described in Section 3.4.2, so we will just cite the result from Ref. [61]:

$$P_2(m) = \frac{e^{-(1+\alpha_2)\bar{m}_0}\bar{m}_0^m}{m!} + \frac{\alpha_2}{(1+\alpha_2)^{m+1}}\mathcal{P}(m+1,(1+\alpha_2)\bar{m}_0), \qquad (3.17)$$

where $\alpha_2 = \frac{t_D}{\tau_{p2}\bar{m}_0}$.

The probability consists of two parts: the first term comes from the ion staying in the cycling transition, and the second term is due to the cases where the ion is pumped into the dark states at some random time.

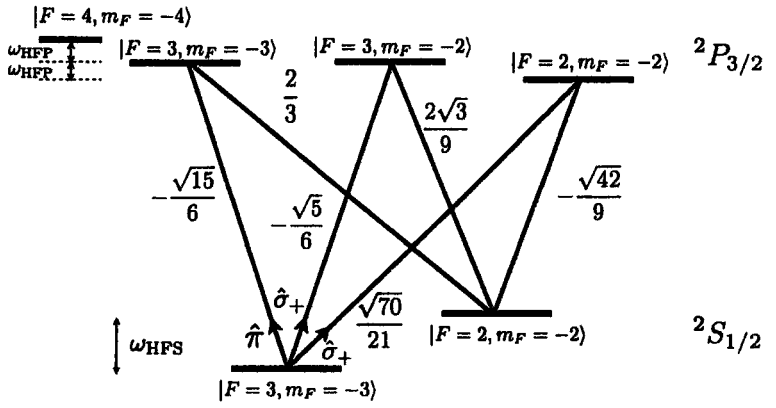

Figure 3.8: The energy levels relevant to the polarization impurity of the Cycler. The lines connecting different levels represent the dipole-allowed transitions, and the numbers beside the lines are Clebsch-Gordon coefficients between the two connected levels.

From Fig. 3.8, we can see there are three leakage paths out of the cycling transition: (1) coupling through the $|^2P_{3/2}, F=3, m_F=-3\rangle$ state due to $\hat{\pi}$-polarized laser light; (2) coupling through the $|^2P_{3/2}, F=3, m_F=-2\rangle$ state due to $\hat{\sigma}_+$-polarized laser light; (3) coupling through the $|^2P_{3/2}, F=2, m_F=-2\rangle$ state due to $\hat{\sigma}_+$-polarized laser light. Suppose the fraction of the imperfectly polarized laser powers are P_π and P_+. We can calculate the contribution due to each path for the average leak time τ_{p2} and then combine them together:

$$\frac{1}{\tau_{p2}} = \frac{1}{1+s+\left[\frac{2(\omega_{HFP}+\delta)}{\gamma}\right]^2}\frac{\frac{5}{27}P_\pi}{1-P_\pi-P_+} + \frac{1}{1+s+\left[\frac{2(\omega_{HFP}+\delta)}{\gamma}\right]^2}\frac{\frac{5}{243}P_+}{1-P_\pi-P_+}$$
$$+\frac{1}{1+s+\left[\frac{2(2\omega_{HFP}+\delta)}{\gamma}\right]^2}\frac{\frac{20}{243}P_+}{1-P_\pi-P_+},$$

where $\omega_{\mathrm{HFP}}/2\pi \approx 60$ MHz is the hyperfine splitting of the $^2P_{3/2}$ state. Therefore,

$$\alpha_2 = \frac{1}{\zeta}\left\{\frac{1+s+(\frac{2\delta}{\gamma})^2}{1+s+\left[\frac{2(\omega_{\mathrm{HFP}}+\delta)}{\gamma}\right]^2}\frac{\frac{5}{27}P_\pi+\frac{5}{243}P_+}{1-P_\pi-P_+}+\frac{1+s+(\frac{2\delta}{\gamma})^2}{1+s+\left[\frac{2(2\omega_{\mathrm{HFP}}+\delta)}{\gamma}\right]^2}\frac{\frac{20}{243}P_+}{1-P_\pi-P_+}\right\}, \tag{3.18}$$

which characterizes the leak probability from the cycling transition to the dark states per emitted photon. If $P_\pi = P_+ = 0.01$, and the laser is adjusted to well below the saturation intensity ($s \ll 1$) and near resonance ($\delta = 0$), we calculate $\alpha_2 \approx \frac{2.65\times10^{-4}}{\zeta}$ for $^{25}Mg^+$.

3.5 Coherent Control and Entanglement

The key point in the Cirac-Zoller gate [14] for quantum computation, and other schemes that rely on the ions' motion, is to couple a spin qubit with the motion in a spin-state-dependent way. Since the motion is shared by all the ions in the ion chain, it provides a way to transfer quantum information from one ionic qubit to another. In order to better understand the coupling between the spin and motion, we have to consider the interaction hamiltonian.

3.5.1 Interaction Hamiltonian

For simplicity, we will assume the spin states $|\downarrow\rangle$ and $|\uparrow\rangle$ can be coupled by an electric dipole transition, but this can be extended to the Raman transitions used in our experiment easily. The interaction between an ion and the electric field of a laser beam can be written as

$$\hat{H}_I = -\hat{\mu}\cdot\frac{E_0}{2}\hat{\epsilon}_L[\exp(k\hat{z}-\omega_L t+\phi)+\text{c.c.}], \tag{3.19}$$

where $\hat{\mu} = e\hat{r}$ is the electric dipole operator. $\hat{\mu}$ is proportional to $\sigma^+ + \sigma^-$, where $\sigma^+ \equiv |\uparrow\rangle\langle\downarrow|$, $\sigma^- \equiv |\downarrow\rangle\langle\uparrow|$. For simplicity, we will consider only one single mode in the z direction; $\hat{z}$ is the ion's displacement operator. For the laser beam, E_0 is the amplitude of the laser electric field; ω_L is the laser frequency; ϕ is the phase of the laser beam; and $\hat{\epsilon}_L$ is the laser polarization. In general, the polarization is a combination of three different polarizations: $\hat{\epsilon}_L = e_-\hat{\sigma}_- + e_0\hat{\pi} + e_+\hat{\sigma}_+$ with $|e_-|^2 + |e_0|^2 + |e_+|^2 = 1$.

Normally, the ion will be cooled to near the motional ground-state, in which case the extent of the ion's motion is much less than the laser wavelength. We can characterize the motional ground state by introducing the Lamb-Dicke parameter:

$$\eta = kz_0 = k\sqrt{\frac{\hbar}{2m\omega_z}}, \tag{3.20}$$

where z_0 is the extent of the motional ground-state wave function. We say the ion is in the Lamb-Dicke limit if $\eta \ll 1$. We can also rewrite the displacement operator as $\hat{z} = z_0(a + a^+)$, where a and a^+ are the annihilation and creation operators for the harmonic oscillator of frequency ω_z produced by the trap potential.

We can transform Eqn. (3.19) into the interaction picture and use the rotating-wave approximation [20]:

$$\hat{H}_{\mathrm{LD}} = \hbar\Omega\sigma^+ \exp\{i\eta(ae^{-i\omega_z t} + a^+ e^{i\omega_z t})\}e^{i(\phi-\delta t)} + \mathrm{H.c.} \tag{3.21}$$

Here, $\Omega = -E_0\langle\uparrow|\hat{\mu}\cdot\hat{\epsilon}_L|\downarrow\rangle/2\hbar$ is the Rabi frequency and $\delta = \omega_0 - \omega_L$ is the detuning. If the Lamb-Dicke limit is satisfied, the exponent in Eqn. (3.21) can be expanded to the lowest order in η:

$$\hat{H}_{\mathrm{LD}} = \hbar\Omega\sigma^+\{1 + i\eta(ae^{-i\omega_z t} + a^+ e^{i\omega_z t})\}e^{i(\phi-\delta t)} + \mathrm{H.c.} \tag{3.22}$$

For certain choices of ω_L, one term in Eqn.(3.22) will be dominant and the spin and motion can be coupled efficiently. There are three resonances in Eqn.(3.22):

1. **Carrier,** $\delta = 0$,

$$\hat{H}_{\text{car}} = \hbar\Omega(\sigma^+ e^{i\phi} + \sigma^- e^{-i\phi}) \tag{3.23}$$

coupling $|n\rangle|g\rangle \leftrightarrow |n\rangle|e\rangle$ with $\Omega_{n,n} = \Omega$.

2. **First red sideband,** $\delta = -\omega_z$,

$$\hat{H}_{\text{rsb}} = \hbar\Omega\eta(a\sigma^+ e^{i\phi} + a^+\sigma^- e^{-i\phi}) \tag{3.24}$$

coupling $|n\rangle|g\rangle \leftrightarrow |n-1\rangle|e\rangle$ with $\Omega_{n,n-1} = \Omega\sqrt{n}\eta$.

3. **First blue sideband,** $\delta = \omega_z$,

$$\hat{H}_{\text{bsb}} = \hbar\Omega\eta(a^+\sigma^+ e^{i\phi} + a\sigma^- e^{-i\phi}) \tag{3.25}$$

coupling $|n\rangle|g\rangle \leftrightarrow |n+1\rangle|e\rangle$ with $\Omega_{n,n+1} = \Omega\sqrt{n+1}\eta$.

The spin and motion coupling can be implemented using the red and blue sideband transitions, and the carrier transition can be used to perform single qubit gates.

3.5.2 Raman Transitions

In our experiments, we use two ground-state hyperfine levels as a qubit. Coherent transitions between levels can be implemented with two-photon stimulated-Raman transitions: two laser beams shining onto an ion at the same time drive the transition from $|\downarrow\rangle$ to $|\uparrow\rangle$ and vice versa via a virtual level $|v\rangle$, which is blue-detuned with respect to the $^2P_{1/2}$ level by Δ. We can picture the two-photon stimulated-Raman transition as the absorption of a photon from one beam and stimulated emission of one photon into the other. During the whole process we wish to alter the m_F number by 1, so one of the lasers must have $\hat{\sigma}_-$ polarization and the other must be polarized $\hat{\pi}$.

In the two-photon stimulated-Raman case, in Eqn. (3.22), k must be replaced by the difference $\Delta k = |\mathbf{k}_1 - \mathbf{k}_2|$ between k-vectors for the two Raman beams, ω_L and ϕ

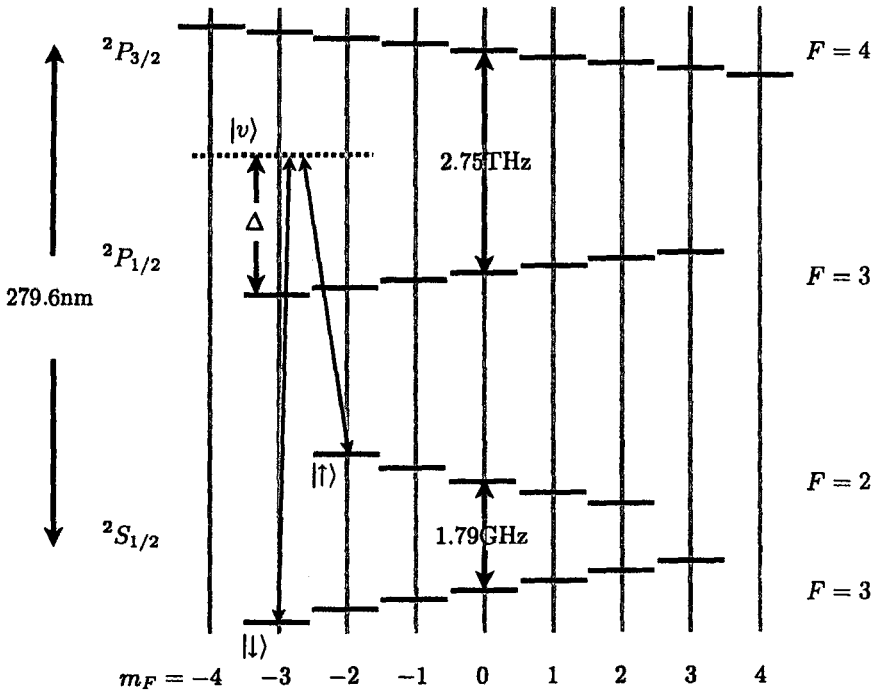

Figure 3.9: Two-photon stimulated-Raman transition for $^{25}Mg^+$. $|\downarrow\rangle$ and $|\uparrow\rangle$ are coupled through a virtual level $|v\rangle$, which is blue-detuned with respect to the $^2P_{1/2}$ level by Δ.

must be replaced by $\omega_1 - \omega_2$ and $\phi_1 - \phi_2$, and $\Omega e^{i\phi}$ must be replaced by the resonant two-photon Raman Rabi frequency [66]

$$\Omega e^{i\phi} \leftrightarrow \frac{e^{i(\phi_1-\phi_2)}}{4\hbar^2} \sum_i \frac{\langle\uparrow|\hat{\mu}\cdot E_2\hat{\epsilon}_2|i\rangle\langle i|\hat{\mu}\cdot E_1\hat{\epsilon}_1|\downarrow\rangle}{\Delta_i}. \tag{3.26}$$

The two-photon Raman scheme has several advantages compared to driving the transition directly:

- The frequency difference between the two lasers can be adjusted very accurately using acoustic-optic modulators.

- By adjusting the phase of the rf source which drives the acoustic-optic modulators, we can keep the phase difference stable.
- Small frequency shifts of the Raman lasers do not affect the Rabi frequency as long as the difference remains unchanged.
- Although the effective Rabi frequency is in the radio-frequency range, we can enjoy the strong electric field gradients provided by the ultra-violet laser beam.
- The Rabi frequency can be adjusted not only by changing the intensity of the two Raman lasers but also by detuning from the virtual Raman level.

The frequency difference between two Raman beams can be tuned to resonance with the red or blue sidebands or the carrier. The interaction (3.22) will drive the transitions

$$|\downarrow\rangle|n\rangle \rightarrow \cos(\Omega_{n,n'}t)|\downarrow\rangle|n\rangle - ie^{i\phi}\sin(\Omega_{n,n'}t)|\uparrow\rangle|n'\rangle \tag{3.27}$$

and

$$|\uparrow\rangle|n'\rangle \rightarrow -ie^{-i\phi}\sin(\Omega_{n,n'}t)|\downarrow\rangle|n'\rangle + \cos(\Omega_{n,n'}t)|\uparrow\rangle|n'\rangle, \tag{3.28}$$

where $\Omega_{n,n'} = \eta\Omega\sqrt{n_>}$ for $n' = n \pm 1$. $n_>$ is the greater of n or n'. A red-sideband transition for $n = 1$ is shown in Fig. 3.10.

The carrier transition can also be described as $n = n'$ and $\Omega_{n,n'} = \Omega$. It is used to realize single qubit gates. In the basis of $\{|\downarrow\rangle, |\uparrow\rangle\}$, the carrier transition can be written in the matrix form:

$$O(\theta,\phi) = \begin{bmatrix} \cos\theta & -ie^{i\phi}\sin\theta \\ -ie^{-i\phi}\sin\theta & \cos\theta \end{bmatrix}, \tag{3.29}$$

where $\theta = \Omega t$. A laser pulse with its duration satisfied $\theta = \Omega t$ will be called 2θ-pulse. Any unitary operation on a single qubit can be implemented by choosing a right combination of the laser pulse length and the phase difference.

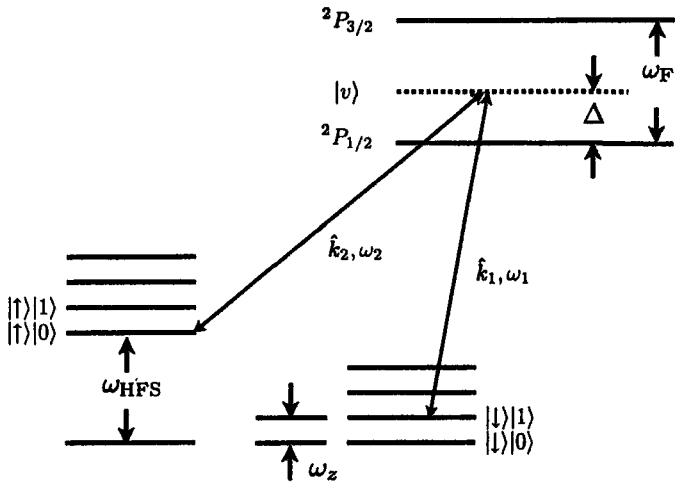

Figure 3.10: Schematic of relevant energy levels for stimulated-Raman transition (not to scale). A red-sideband transition for $n = 1$ is shown here. Typically, $\Delta \gg \omega_{HFS} \gg \omega_z$.

Two-qubit gates can be realized by sequentially applying several pulses of the Raman beams. Here, we will demonstrate a controlled-NOT gate on the basis $|n\rangle|j\rangle$, where $n \in \{0, 1\}$ is ion's motional qubit, and $j \in \{\downarrow, \uparrow\}$ is the internal ionic qubit, following the recipe from Ref. [15].

The operation of the controlled-NOT gate is simple: if the first qubit is set to $|1\rangle$ then the second qubit is flipped, otherwise the second qubit is left alone. The matrix form of the controlled-NOT gate is

$$\text{CNOT} = \begin{bmatrix} 1 & 0 & 0 & 0 \\ 0 & 1 & 0 & 0 \\ 0 & 0 & 0 & 1 \\ 0 & 0 & 1 & 0 \end{bmatrix}. \tag{3.30}$$

The controlled-NOT gate can be realized by three pulses:

(1) A $\pi/2$ pulse on the carrier transition. This pulse only affects the internal ionic qubit. The laser parameters are chosen such that $\theta = \pi/4$ and $\phi = 0$ in Eqn. (3.29). In the basis of $|n\rangle|j\rangle$, the operation can be written as

$$O_1 = \frac{1}{\sqrt{2}} \begin{bmatrix} 1 & -i & 0 & 0 \\ -i & 1 & 0 & 0 \\ 0 & 0 & 1 & -i \\ 0 & 0 & -i & 1 \end{bmatrix}. \tag{3.31}$$

(2) A 2π pulse on the blue sideband transition between $|\uparrow\rangle$ and an auxiliary atomic level $|aux\rangle$. This pulse only affects the state $|1\rangle|\uparrow\rangle$ and reverses the sign of this state. This operation is written in the matrix form as

$$O_2 = \begin{bmatrix} 1 & 0 & 0 & 0 \\ 0 & 1 & 0 & 0 \\ 0 & 0 & 1 & 0 \\ 0 & 0 & 0 & -1 \end{bmatrix}. \tag{3.32}$$

(3) A $\pi/2$ pulse on the carrier transition, with phase shift of π respect to step (1). So $\theta = \pi/4$, $\phi = \pi$ and the operation can be written as

$$O_3 = \frac{1}{\sqrt{2}} \begin{bmatrix} 1 & i & 0 & 0 \\ i & 1 & 0 & 0 \\ 0 & 0 & 1 & i \\ 0 & 0 & i & 1 \end{bmatrix}. \tag{3.33}$$

It is easy to see that the overall effect is the controlled-NOT gate:

$$\text{CNOT} = O_3 \cdot O_2 \cdot O_1.$$

The controlled-NOT gates, combined with the single qubit gates, provide the universal set of quantum gates required by the DiVincenzo criteria [49]. It has been proven that any unitary operations on a serial of qubits can be composed of the two-qubit controlled-NOT gate and single qubit gates [67, 68].

3.5.3 Rabi Frequency

In this section we will calculate the Rabi frequency for $^{25}Mg^{+}$. In the case $\omega_1 - \omega_2 \approx \omega_{HFS}$, we will call $\omega_1 = \omega_b$ the blue Raman beam frequency and $\omega_2 = \omega_r$ the red Raman beam frequency. Similarly, we also write the electric fields of the lasers as $E_1\hat{\epsilon}_1 = E_b\hat{\epsilon}_b = E_b(b_-\hat{\sigma}_- + b_0\hat{\pi} + b_+\hat{\sigma}_+)$ and $E_2\hat{\epsilon}_2 = E_r\hat{\epsilon}_r = E_r(r_-\hat{\sigma}_- + r_0\hat{\pi} + r_+\hat{\sigma}_+)$. In our $^{25}Mg^{+}$ experiments, we consider Raman transitions between the $^2S_{1/2}$ hyperfine states $|F = 3, m_F = -3\rangle \equiv |\downarrow\rangle$ and $|F = 2, m_F = -2\rangle \equiv |\uparrow\rangle$. In calculating the Rabi frequency, the hardest part is to evaluate the matrix elements $\langle i|\hat{\mu}\cdot E_j\hat{\epsilon}_j|\downarrow,\uparrow\rangle$. The formula can be derived from [62]:

$$\begin{aligned}\langle\psi|\hat{\mu}\cdot E\hat{\epsilon}|\psi'\rangle &= (-1)^{\frac{1}{2}q(1+q)+1+2F-m_F+I+J'+S+L'+J}\delta_{II'}\delta_{SS'} \\ &\times \sqrt{(2F+1)(2F'+1)(2J+1)(2J'+1)(2L+1)} \\ &\times \begin{pmatrix} F & 1 & F' \\ -m_F & q & m'_F \end{pmatrix}\begin{Bmatrix} J & F & I \\ F' & J' & 1 \end{Bmatrix}\begin{Bmatrix} L & J & S \\ J' & L' & 1 \end{Bmatrix}\left(\frac{3\varepsilon_0\hbar\lambda^3\gamma E^2}{8\pi^2}\right)^{\frac{1}{2}},\end{aligned}$$

where $|\psi\rangle = |LSJIFm_F\rangle$ is the excited state and $|\psi'\rangle = |L'S'J'I'F'm'_F\rangle$ is the ground-state; $q = -1, 0, 1$ for $\hat{\epsilon} = \hat{\sigma}_-$, $\hat{\pi}$, $\hat{\sigma}_+$ polarization; λ is the transition wavelength; γ is the linewidth of the transition; and E is the laser field strength.

The relevant excited states are the $3p$ fine structure levels. Using the formula above to calculate the matrix elements $\langle i|\hat{\mu}\cdot E_j\hat{\epsilon}_j|\downarrow,\uparrow\rangle$ in Eqn.(3.26), we can derive the carrier Rabi frequency:

$$\Omega_{\downarrow\uparrow} = \frac{\sqrt{15}}{9}g_b g_r(b_0 r_+ + b_- r_0)\frac{\omega_F}{\Delta(\Delta - \omega_F)}, \tag{3.34}$$

where the fine structure splitting $\omega_F/2\pi \approx 2.75$ THz for $^{25}Mg^+$ and

$$g_{b,r} = \frac{E_{b,r}}{2\hbar}|\langle {}^2P_{3/2}, F = 4, m_F = -4|\hat{\mu}\cdot\hat{\sigma}_-|\downarrow\rangle|,$$

which is the Rabi frequency for the cycling transition. Here we have neglected the hyperfine splitting of the $3p$ excited states.

3.5.4 AC Stark Shifts

The strong alternating electric field in each Raman beam will cause an energy shift of the qubit states, even if the lasers are off-resonant. This effect is called the AC Stark shift. In the limit that the detuning Δ_i is much larger comparing to the transition linewidth γ, the Stark shift of the Zeeman sublevel m_F due to j-th laser beam is [66]

$$\delta(m_F, j) = \frac{1}{4\hbar^2}\sum_i \frac{|\langle i|\hat{\mu}\cdot E_j\hat{\epsilon}_j|m_F\rangle|^2}{\Delta_i}. \tag{3.35}$$

In general, both $|\downarrow\rangle$ and $|\uparrow\rangle$ states will be shifted by all laser beams which are present. Assuming that the Zeeman levels are not resolved and the hyperfine splitting of $^2P_{1/2}$ and $^2P_{3/2}$ are negligible comparing with Δ_i, we can write down the net AC Stark shift:

$$\begin{aligned}\delta(\uparrow) - \delta(\downarrow) \;=\; & g_b^2\left[\frac{\frac{1}{9}b_+^2 + \frac{1}{3}b_0^2 + \frac{5}{9}b_-^2}{\Delta + \omega_{\rm HFS}} + \frac{\frac{8}{9}b_+^2 + \frac{2}{3}b_0^2 + \frac{4}{9}b_-^2}{\Delta + \omega_{\rm HFS} - \omega_{\rm F}}\right. \\ & \left. - \frac{\frac{2}{3}b_+^2 + \frac{1}{3}b_0^2}{\Delta} - \frac{\frac{1}{3}b_+^2 + \frac{2}{3}b_0^2 + b_-^2}{\Delta - \omega_{\rm F}}\right] \\ & + g_r^2\left[\frac{\frac{1}{9}r_+^2 + \frac{1}{3}r_0^2 + \frac{5}{9}r_-^2}{\Delta} + \frac{\frac{8}{9}r_+^2 + \frac{2}{3}r_0^2 + \frac{4}{9}r_-^2}{\Delta - \omega_{\rm F}}\right. \\ & \left. - \frac{\frac{2}{3}r_+^2 + \frac{1}{3}r_0^2}{\Delta - \omega_{\rm HFS}} - \frac{\frac{1}{3}r_+^2 + \frac{2}{3}r_0^2 + r_-^2}{\Delta - \omega_{\rm F} - \omega_{\rm HFS}}\right].\end{aligned} \tag{3.36}$$

In the limit of $\omega_{\rm HFS} \ll \Delta, \omega_{\rm F}$, Eqn.(3.36) can be simplified to

$$\delta(\uparrow) - \delta(\downarrow) \approx [g_b^2(b_+^2 - b_-^2) + g_r^2(r_+^2 - r_-^2)]\frac{5\omega_{\rm F}}{9\Delta(\Delta - \omega_{\rm F})}. \tag{3.37}$$

The Stark shifts vanish if $\hat{\pi}$-polarized laser beams are used for driving the Raman transition, or the polarization of the Raman beams satisfies $b_+ \approx b_-$, $r_+ \approx r_-$.

3.5.5 Spontaneous Emission

In our Raman scheme, even the virtual state is well-detuned from the $3p$ excited states, the possibility still exists for the ion to be excited and spontaneously decay back to the ground-states. The coherence of the atomic qubit will be destroyed if spontaneous emission happens. In this section, we will try to calculate the total spontaneous emission rate R_{SE} from the $3p$ levels. This rate is equal to the sum of $P_i\gamma_i$, where P_i is the probabilities that each intermediate excited state is occupied and γ_i is the linewidth of the same state [66],

$$R_{\mathrm{SE}} = \sum_i \gamma_i P_i = \frac{1}{4\hbar^2} \sum_i \sum_{j=r,b} \sum_{m_F=\downarrow,\uparrow} \frac{P_{m_F}\gamma_i |\langle m_F|\hat{\mu}\cdot E_j\hat{\epsilon}_j|i\rangle|^2}{\Delta_i^2}. \tag{3.38}$$

P_{m_F} is the probability of being in the m_F ground state. For $^{25}\mathrm{Mg}^+$, we find

$$\begin{aligned} R_{\mathrm{SE}} &= \gamma P_\downarrow \left[\frac{g_b^2(\frac{2}{3}b_+^2 + \frac{1}{3}b_0^2)}{\Delta^2} + \frac{g_b^2(\frac{1}{3}b_+^2 + \frac{2}{3}b_0^2 + b_-^2)}{(\Delta-\omega_{\mathrm{F}})^2} \right. \\ &\qquad \left. + \frac{g_r^2(\frac{2}{3}r_+^2 + \frac{1}{3}r_0^2)}{(\Delta-\omega_{\mathrm{HFS}})^2} + \frac{g_r^2(\frac{1}{3}r_+^2 + \frac{2}{3}r_0^2 + r_-^2)}{(\Delta-\omega_{\mathrm{F}}-\omega_{\mathrm{HFS}})^2} \right] \\ &+ \gamma P_\uparrow \left[\frac{g_b^2(\frac{1}{9}b_+^2 + \frac{1}{3}b_0^2 + \frac{5}{9}b_-^2)}{(\Delta+\omega_{\mathrm{HFS}})^2} + \frac{g_b^2(\frac{8}{9}b_+^2 + \frac{2}{3}b_0^2 + \frac{4}{9}b_-^2)}{(\Delta+\omega_{\mathrm{HFS}}-\omega_{\mathrm{F}})^2} \right. \\ &\qquad \left. + \frac{g_r^2(\frac{1}{9}r_+^2 + \frac{1}{3}r_0^2 + \frac{5}{9}r_-^2)}{\Delta^2} + \frac{g_r^2(\frac{8}{9}r_+^2 + \frac{2}{3}r_0^2 + \frac{4}{9}r_-^2)}{(\Delta-\omega_{\mathrm{F}})^2} \right], \end{aligned} \tag{3.39}$$

where $\gamma/2\pi = 43$ MHz. We have neglected the hyperfine splitting of the $3p$ excited states. In order to suppress AC Stark shifts, we will use $b_+ \approx b_-$ and $r_+ \approx r_-$. Substituting them into Eqn. (3.39), we find that all the terms in the round brackets in the numerators sum to 1.

We also want to minimize the probability of spontaneous emission during qubit operations. One of the important qubit operations is the π-pulse on the carrier tran-

sition, in which case $\Omega\tau_\pi = \frac{1}{2}\pi$. We can then calculate the probability of spontaneous emission for the time τ_π. During the π-pulse transition, the average time the ion spends in each qubit state is 1/2. We can also safely ignore $\omega_{\mathrm{HFS}} = 1.79$ GHz compared to ω_{F} and Δ which are on the order of THz. Using these assumptions, we can calculate the probability of spontaneous emission for the time τ_π from Eqn. (3.39):

$$P_{\mathrm{SE}} = R_{\mathrm{SE}}\tau_\pi \approx \frac{\pi\gamma}{6|\Omega_{\downarrow\uparrow}|}(g_b^2 + g_r^2)\left[\frac{1}{\Delta^2} + \frac{2}{(\Delta - \omega_{\mathrm{F}})^2}\right]. \tag{3.40}$$

The conditions to minimize P_{SE} are $\Delta = (\sqrt{2} - 1)\omega_{\mathrm{F}} \approx 1.21$ THz, $g_b = g_r$ and $b_0 = 1$, $b_+ = b_- = 0$, $r_+ = r_- = 1/\sqrt{2}$, $r_0 = 0$. The minimum probability is

$$P_{\mathrm{SE}} = \frac{12\pi}{\sqrt{15}}\frac{\gamma}{\omega_{\mathrm{F}}} \approx 1.5 \times 10^{-4}. \tag{3.41}$$

This probability will be increased by $1/\eta$ for sideband transitions because the Rabi frequency in Eqn. (3.40) needs to be replaced by $\eta\Omega$. Since quantum error correction (QEC) is required to build a robust quantum computer and this demands that the error during a gate operation be less than 10^{-4} * [69], a choice of the virtual state that is blue of the $^2P_{1/2}$ state and red of the $^2P_{3/2}$ state may not allow fault-tolereant QEC for $^{25}Mg^+$ ions.

Another choice would be to detune the virtual state blue of both the $^2P_{3/2}$ state and the $^2P_{1/2}$ state. As long as we detune the virtual state far enough from the $^2P_{3/2}$ state, we can make the spontaneous emission rate arbitrarily small. But the Rabi frequency is inversely proportional to Δ^2 for large detuning, as shown by Eqn. (3.34), so we need to increase the laser power by a large amount in order to keep the Rabi frequency the same as we increase the detuning.

*The error threshold for QEC depends on the noise model, but it is generally believed to be on the order of 10^{-4}.

Chapter 4

Trap Assembly

Theory has shown that trapped ions are one of the strongest candidates to realize quantum computation, but that doesn't mean building a quantum computer is an easy task. "Quantum phenomena do not occur in a Hilbert space; they occur in a laboratory." [70]. A lot of hands-on work has been done in order to build a trapped-ion apparatus in our lab. In this and subsequent chapters, we will describe the details of various systems which are essential for our ion-trapping. Sometimes, they may seem trivial and tedious, but that's just what experimental physics is all about. Every detail has to be perfect to make the big machine work.

This chapter is devoted to the trap assembly. We will describe the actual trap, the magnesium ovens and the electron guns. The voltage supplies, both DC and RF, will also be described in this chapter. The vacuum system is the topic of Chapter 5. The final pressure should be on the order of 10^{-11} torr, so it is essential to make sure that everything is as clean as possible during the vacuum cleaning and assembling. Various laser beams needed to address and manipulate magnesium ions are discussed in Chapter 6. We have developed laser sources at ultraviolet wavelengths to drive the transitions of magnesium ions, and also set up Doppler-free saturated absorption spectroscopy of iodine as a frequency reference. Finally, we will describe the imaging system in Chapter 7. The imaging system is used to collect the fluorescence from trapped ions and form an image of the trapped ions.

4.1 Ion Trap

The trap we have built is a square trap, as described in Section 2.2.2. It is similar to the one described in Ref. [31]. Table 4.1 is a list of parts for our trap.

The trap holder is made of macor and machined by the Machine Shop*. The four 0.032" diameter holes were drilled first and then the macor was cut into a U shape, which ensured that the holes on each arm of the holder were aligned. In order to prevent extra charges accumulating on the dielectric, we also machined a set of stainless steel shields to cover the trap holder. The trap holder is mounted to the base plate using 1/2" long 4-40 screws.

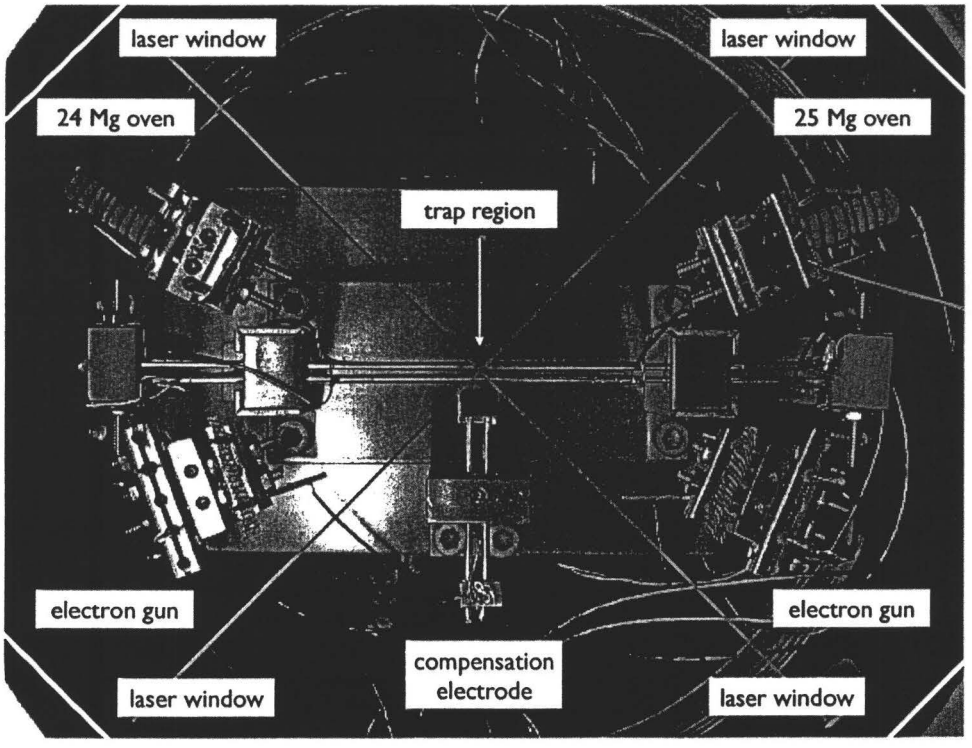

Figure 4.1: Trap assembly inside the vacuum chamber. The two lines show the laser beams passing through the trap centre.

*Science and Engineering Machine Shop, JHE, contact Yosh Kitamura (ext. 24296)

Item	Company	Part Number	Quantity
macor trap holder, machined by Machine Shop	Technical Products		1
s/s holder shields, machined by Machine Shop			3pc
macor constraint brackets, machined by Machine Shop	Technical Products		2
rod electrodes, need electropolishing	Small Parts	GWX-330-30	4
tube electrodes, need electropolishing	Small Parts	HTX-19X-24	4
polyimide tubes	MicroLumen	320-I	4
s/s shim constraints	McMaster CARR	2317K15	4
3/8" long 4-40 screws, for trap holder	McMaster CARR	92200A108	4
1/2" long 4-40 screws, for all the other	McMaster CARR	92200A110	10
1/16" long 4-40 nuts	McMaster CARR	90730A005	
3/4" long 4-40 threaded rods	McMaster CARR	95412A867	6
base plate, 0.025" thick s/s, machined by Machine Shop			1
1/2" long 0-80 threaded rods	Kimball	SS-TR-0-80	2
0-80 nuts	McMaster CARR	90730A001	4
lock washers for 4-40 screw	McMaster CARR	91475A018	
alumina spacer for compensation electrode	Alfa Aesar	32914	1
0.032" s/s rods, leads for compensation electrode	Small Parts	GWX-320-30	2
compensation electrode, 0.01" thick s/s shim	McMaster CARR	2317K17	1
5/32" long 0-80 set screws	McMaster CARR	92311A053	1
Kapton insulating wires, 0.25 mm diameter	ISI	9943100	

Table 4.1: Checklist for the trap parts

The rod electrodes are made from 0.033" diameter stainless steel rods, approximately 2.8" long. The diameter is slightly larger than the holes in the trap holder because the diameter will be reduced after electropolishing. The position of the rods is fixed using constraints made of stainless steel shim, the constraint then is tightened to the macor L-shape constraint. Electrical connection to the rod is made by simply spot welding 0.25 mm diameter wire to its ends.

The tube electrodes are cut by the Machine Shop to prevent burrs. The tubes have 0.035" inner diameter and 0.042" outer diameter. They are insulated from the rod electrodes by polyimide (Kapton^{TM}) tubes whose wall thickness is 25 μm. On the trap side, these insulating tubes are completely covered by the stainless steel tubes to prevent any charges accumulating on the polyimide. During assembly, a microscope should be used to inspect if any polyimide is sticking out. The tube end that is away from the trap is slightly crimped in order to hold the tube electrode in place. It is difficult to spot weld wires to the tube electrodes directly, so tabs about 5 mm long are cut from the tube ends and the wires are spot welded to these tabs.

The compensation electrode is used to adjust the position of the dc minimum to coincide with the position of the rf null, which is important for minimizing the micromotion. It is a 4 mm $\times$ 6 mm rectangular electrode made of 0.5 mm thick stainless steel shim. It is positioned about 5 mm away from the trap centre along a line connecting the rf rods.

4.2 Magnesium Ovens and Electron Guns

Table 4.2 is a list of parts for the magnesium ovens and electron guns. We have one ^{24}Mg oven and one ^{25}Mg oven in our vacuum chamber. These ovens each have their own electrical connections to the dc feedthrough but they share a common ground.

Neutral magnesium atoms are produced by resistively heating the oven to about 175 °C.

Item	Company	Part Number	Quantity
s/s holders, machined by Machine Shop			4
leads for oven, e-gun and accelerator, made of 0.032 " diameter s/s rods	Small Parts	GWX-0320-30	12
leads for collimator, made of 1/16 " diameter s/s rods	Small Parts	ZRXX-01-36	4
s/s clamps, eV Parts	Kimball	SS-SC-B3M	12
s/s clamps, eV Parts	Kimball	SS-SC-B5M	4
alumina split tubes, eV Parts	Kimball	AL2O3-XT-B-250	24
alumina spacers	Alfa Aesar	32915	2
ceramic cement	SIS	SCC8	
tungsten wires for oven, 0.015" diameter	Jim Garrett, BIMR		2
thermocouple wires	Omega		2
s/s shims for collimator, 0.01 " thick	McMaster CARR	2317K17	2
thoriated tungsten wire	GoodFellow	306-320-71	
s/s grids for accelerator	McMaster CARR	9230T522	2
1/16" long 0-80 set screws	McMaster CARR	92311A050	8

Table 4.2: Checklist for ovens and electron-guns

We have explored two different oven designs during our experiments. The first design uses tantalum tubing of inner diameter 0.86 mm and a wall thickness 0.08 mm with a length close to 1 cm [22]. A hole of $\approx$ 1 mm diameter is poked in the middle of the tube to let the vaporized magnesium through. One end of the tube is then crimped shut. Several mm-sized or smaller chunks of magnesium are cut from larger pieces and placed into the tube through the other open end, which is pinched off afterwards to close the tube. The ends are folded on the side without the hole. Both ends of the oven are then spot welded to 1/32" diameter stainless steel rods. Electrical connections to the oven are made by simply spot welding 0.25 mm diameter

wire to the stainless steel rods. When a current of roughly 1.6 A is passed through the oven, the tube is heated and vaporizes the neutral magnesium. An aperture made of a 1 cm $\times$ 1 cm $\times$ 1 cm box is also placed in front of the oven. The box is made from stainless steel shim and has a 1 mm hole facing the trap. The oven, the hole, and the trap centre are carefully aligned such that after the box, the neutral magnesium beam is roughly collimated and passes through the trap centre.

This oven design has a very low thermal mass and can be heated very quickly. During our experiments we found it is useful to know the temperature of the oven, since the ionization rate inside the trap depends on the neutral atom flux, which is a function of the temperature of the oven. In order to achieve this goal, we switched to another oven design based on a design by the NIST Ion Storage group. The oven is made of a 10 mm long alumina spacer of 4 mm outer diameter. The spacer has four 0.80 mm diameter holes. One of the holes is filled with magnesium foil, and cemented closed on one end. A type K thermocouple is threaded through another hole to measure the temperature. The other two holes are left empty. The spacer is tightly wrapped using tungsten wire. When current passes through the tungsten wire, the tungsten wire and the spacer heat up and this sends neutral magnesium in the direction of the trap. The atomic beam is also roughly collimated using a stainless steel plate with a hole of $\approx$ 1.5 mm diameter on it.

One way to produce magnesium ions is electron-impact ionization, in which case high-energy electrons collide with neutral magnesium atoms and knock one valence electron out. The high-energy electrons are produced by an electron gun made by winding an approximately 3 cm length of 25-μm-diameter thoriated tungsten wire into an approximately 1 cm long form. We prefer thoriated tungsten because it has a higher current-carrying capacity, a longer electrode lifetime and a lower work function comparing to normal tungsten. The small diameter of the thoriated tungsten gives

a large resistance and small thermal mass, so the electron gun can be heated up and cooled down quickly. The wire is spot welded to two 1/32" diameter stainless steel rods and the rods are connected to the electrical feedthroughs using 0.25 mm wires. When a current of $\approx$ 0.5 A is passed through the electron gun, the wire heats up and the electrons become energetic enough to leave the tungsten surface. The free electrons are then directed to the trap centre by a positively biased stainless steel wire grid located in between the electron gun and the trap centre. A voltage of 15 V is applied to the grid to give the electron an energy of $\approx$ 15 eV, at which the cross section for electron-impact ionization is maximized [71].

An alternative way to produce ions from neutral atoms is photoionization [72]. For magnesium, the photoionization is a two-photon process: the neutral magnesium is excited to the $^1P_1$ state by absorbing a resonant photon at 285 nm, and then from the excited state, one outer electron can absorb another photon and gain enough energy to become free. For typical experiments, photoionization has several advantages over electron-impact ionization. By adjusting the frequency of the laser, only the desired isotope is loaded into the trap. Photoionization is also more effective than electron-impact ionization, which allows much lower flux of neutral atoms in the trap region, greatly reducing the plating on the trap electrodes and the load on the vacuum pumps. Since no electron beams are involved, there is no charging of dielectric parts. These factors lead to a longer ion lifetime.

The photoionization laser will be described in Chapter 6. Given the positions of the ovens with respect to the windows, neutral magnesium beam will intersect the photoionization laser beam with a 22.5° or 67.5° angle in present setup (see Fig. 4.1). This will introduce significant Doppler broadening which will prevent us from selectively ionizing different isotopes. It is better to have a design where the neutral beam and laser beam are perpendicular to each other. However, this

presents challenges because we have other laser beams coming in perpendicular to the photoionization laser.

4.3 Vacuum Chamber, Viewports and Feedthroughs

The vacuum chamber into which the trap is placed is a Kimball Physics spherical octagon with eight 2.75" ConFlat (CF) vacuum ports along its walls and 6 " CF ports on its top and bottom. The bottom flanges have grooves into which two "groove grabber" clamps (Kimball Physics Part No. MCF600-GG-CR04) are placed on opposite side of the chamber. The groove grabbers are used to mount the base plate on which the trap is bolted.

Table 4.3 is a list of all the parts to assemble the vacuum chamber.

Item	Company	Part Number	Quantity
Vacuum chamber	Kimball	MCF600-S0200800-A	1
Re-entrant flange	Kimball	Custom-made	1
slotted bolts, 2-3/4 CF, tapped hole, not silver-plated, for re-entrant flange	Duniway	BX-28-087	6
s/s grid	McMaster CARR	9230T522	1
Fused silica viewport (AR-coated)	Ceramaseal	11466-01-CF	5
Sapphire viewport (regular)	Varian	FVS0100	1
rf feedthrough	ISI	9222002	1
rf connectors	ISI	9924003	1
dc feedthrough	ISI	9132005	1
dc connectors	ISI	9923014	20

Table 4.3: Parts to assemble the vacuum chamber.

The magnesium ion used in this research has cycling transitions in the ultraviolet ($\approx$ 280 nm). Because normal glass strongly absorbs UV light, fused silica viewports are used. The viewports are purchased from Ceramaseal. They are anti-reflection

coated and have less than 1% reflection at 280 nm . A regular viewport from Varian is also used on the port opposite to the pump port in the vacuum chamber; this part is for visual inspection – no UV laser beams pass through it. Each viewport can only handle temperatures up to 200 °C.

The rf feedthrough was purchased from Insulator Seal. It has two grounded shielded MHV connectors. The voltage and current rating are 5000 VDC and 3 A. It can be baked to 450 °C. The dc feedthrough is also from Insulator Seal. It has 20 pins, each of which can handle 700 VDC and 10 A. It can also be baked to 450 °C. The vacuum-side connectors are cut to 1.25" length. The air-side connector is a circular MS connector.

The vacuum chamber has eight 2.75" CF flanges. Five of them are closed by the viewports, one by the rf feedthrough and one by the dc feedthrough. The last one is connected to a cross which connects to the vacuum pumps. A 6" blank flange closes the bottom of the chamber, and a custom-made re-entrant flange closes the top.

The re-entrant flange enables us to put our objective lens (see Chapter 7) close to the trap centre. The working distance of the objective is only 15 mm, which is less than half of the chamber's height. The re-entrant flange was custom-made by Kimball Physics. It is basically a 6" to 2.75" flange adaptor. The 6" flange fits the top of the chamber, and the 2.75" flange is closed by a viewport. The bolts that tighten the 2.75" flange are on the vacuum side, so they have to be slotted to prevent trapping air in the tapped holes; they should not be of the silver-plated variety. We also put a stainless steel wire mesh on the viewport to prevent charges accumulating on the dielectric window and to shield any accumulated charges.

4.4 Tools

Table 4.4 is a list of tools needed to assemble the trap. All tools have to be vacuum-clean (see Section 5.3).

0.050 " Allen Key for 0-80 screws
3/32 " Allen Key for 4-40 screws
3/32 " ball driver for 4-40 screws
1/8 " box wrench for 0-80 nuts
3/32 " box wrench for 4-40 nuts
3/32 " hex nutdriver for 4-40 nuts
adjustable wrench
fine tweezers
nonmarring precision-tip tweezers (McMaster CARR 6182A24)
wire cutter (McMaster CARR 3730A5)
diagonal cutters
pliers
round-nose pliers
stainless steel rule, 1/100" scale
stainless steel rule, 0.5 mm scale

Table 4.4: Checklist for the tools

4.5 Voltage Supplies

As mentioned in Chapter 2, the ion trap needs both RF voltage and DC voltage. The voltages are delivered to the trap through the electrical feedthroughs in the vacuum system.

4.5.1 RF Helical Resonator

The RF voltage applied to the trap needs to be about 500 V with frequency $\approx$ 10-20 MHz. One way to realize this is to use a helical resonator. The design and construction of such a resonator are discussed in Refs [73, 74, 75]. For a given frequency, diameter of the outer conductor and quality factor Q, we can calculate the

inner conductor diameter, the number of windings, the winding pitch and the coil length. The resonators were designed and built in-group by Jason Nguyen and Sarah Dyck.

The rf signal is produced by a HP-8662A signal generator. An rf amplifier (AR 25A250A) is used to increase the rf power by about 40 dB. The output from the amplifier is then inductively coupled into the resonator using a small closed loop of bare wire.

The resonator we are using at the moment has resonant frequency 22 MHz with trap attached and $Q \approx 400$. The amplitude of the voltage at the trap V_{rf} is related to the input power P and the quality factor Q of the resonator:

$$V_{\text{rf}} = \zeta\sqrt{PQ}$$

where ζ is a scale factor depending on the geometry of the design. For a helical resonator ζ is on the order of 10. We can calculate the required power for various rf voltages. For example, in order to get 200 V rf voltage at the trap, we need 1 W of rf power delivered to the resonator.

4.5.2 Static Voltage Supplies

The dc voltages applied to the trap pass through a filter box before connecting to the DC feedthrough. The reason for the filter box is that the rf will introduce an oscillating voltage in the dc electrodes if the dc electrodes are not kept at rf ground. The filter is a low pass filter (see Fig. 4.2) consisting of a 1 kΩ resistor and a 0.22 μF capacitor in series.

The voltage is supplied by two power supplies. A Bertan 225-10R with maximum 10 kV output and 1 V resolution provides the coarse adjustment, and a four-output

HP-6627A, biased by the Bertan, provides the fine adjustment 50 mV (effective precision). The HP-6627A can be biased up to 240 V and has maximum output of 50 V. Both power supplies are used for the four tube electrodes. Another Bertan 225-10R is used for the compensation electrode. A LabView program controls the voltage supplies through the GPIB bus.

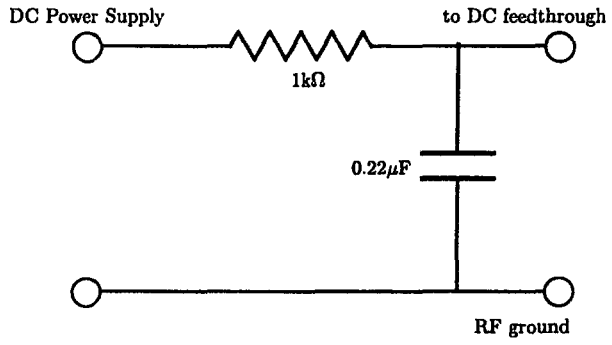

Figure 4.2: Filter box for DC voltage supply.

Chapter 5

Vacuum System

Trapped-ion experiments require ultra-high vacuum (UHV) conditions in order to ensure that background collisions do not affect the ions during experiments. Practically, this means that pressure on the order of 10^{-11} torr is needed. At this pressure, the collision rate with background gas is low enough (about one collision every ten minutes for 3×10^{-11} torr pressure) that experiments repeated at a kHz rate are not affected by background collisions.

Thus, the vacuum system must be capable of maintaining this UHV environment. The basic procedure that will ensure the system reaches UHV conditions involves

- using only oil-free vacuum pumps to maintain a clean vacuum system,
- pre-baking all stainless steel parts used in the system,
- vacuum cleaning all parts that will be used to assemble the vacuum system,
- maintaining a clean environment while assembling the system,
- using only bakeable parts in the system and baking the whole system at 200 °C for a long enough period of time in order to remove the water vapor stored on the stainless steel.

All of the points will be discussed in the following sections.

5.1 Pumps and Gauges

Table 5.1 contains a list of the vacuum pumps and gauges which are used in our system.

Item	Company	Part Number
Ion pump, StarCell, 20L/s	Varian	9191145
Ion pump controller, MidiVac	Varian	9295000
Ion pump HV cable, bakeable	Varian	9290708
TSP cartridge	Varian	9160050
TSP controller	Varian	9290022
TSP cable	Varian	9240730
Turbo pump, Turbo-V 70LP	Varian	9699368
Turbo pump controller	Varian	9699505
Dry scroll pump, SH-100	Varian	SH01001UNIV
Nude ion gauge	Duniway	I-NUDE-F
Nude ion gauge controller	Duniway	Terranova 934-UHV
Nude ion gauge cable, bakeable	Duniway	8100-0935-20
Glass ion gauge	Varian	K2471303
Glass ion gauge controller	Varian	LP1203010100
Glass ion gauge cable	Varian	L64553010

Table 5.1: Vacuum pumps and gauges

The primary vacuum pump for the chamber is a 20 L/S StarCell ion pump, which has a maximum starting pressure 5×10^{-2} torr and can reach an ultimate pressure lower than 1×10^{-11} torr. The maximum baking temperature for the pump is 350 °C with the magnet and 400 °C without. This pump does a good job of removing background helium and hydrogen and can maintain an environment of 10^{-11} torr. It is oil-free and has no moving parts which provides a clean and vibration-free experimental environment. The MidiVac ion pump controller has three voltage settings (3kV, 5kV and 7kV). It is easier to start the ion pump with 7kV setting and we normally use 5kV after the pump starts.

In addition to the ion pump, a titanium sublimation pump (TSP) is included in the vacuum system. Pumping is accomplished by coating the inner surfaces of

the vacuum parts with a titanium film. A fresh titanium film can react with most gas molecules (except noble gases) and form low vapor pressure compounds, thereby reducing the pressure. The normal operation current is 47-48 A for 1 minute. After the filament is on, the pressure at first will increase because the filament will be heated up and residue gas will be driven away from the filament. Subsequently the pressure will drop since the fresh titanium film will begin to react with the background gas. After a while, the pressure will increase again because the vacuum wall starts to heat up and degas. In order to reduce the burst of gas released when power is applied, the filament needs to be degassed at current 37-42 A for at least 1 minute after being exposed to the air. The TSP only needs to be run occasionally. We normally turn it on once a week.

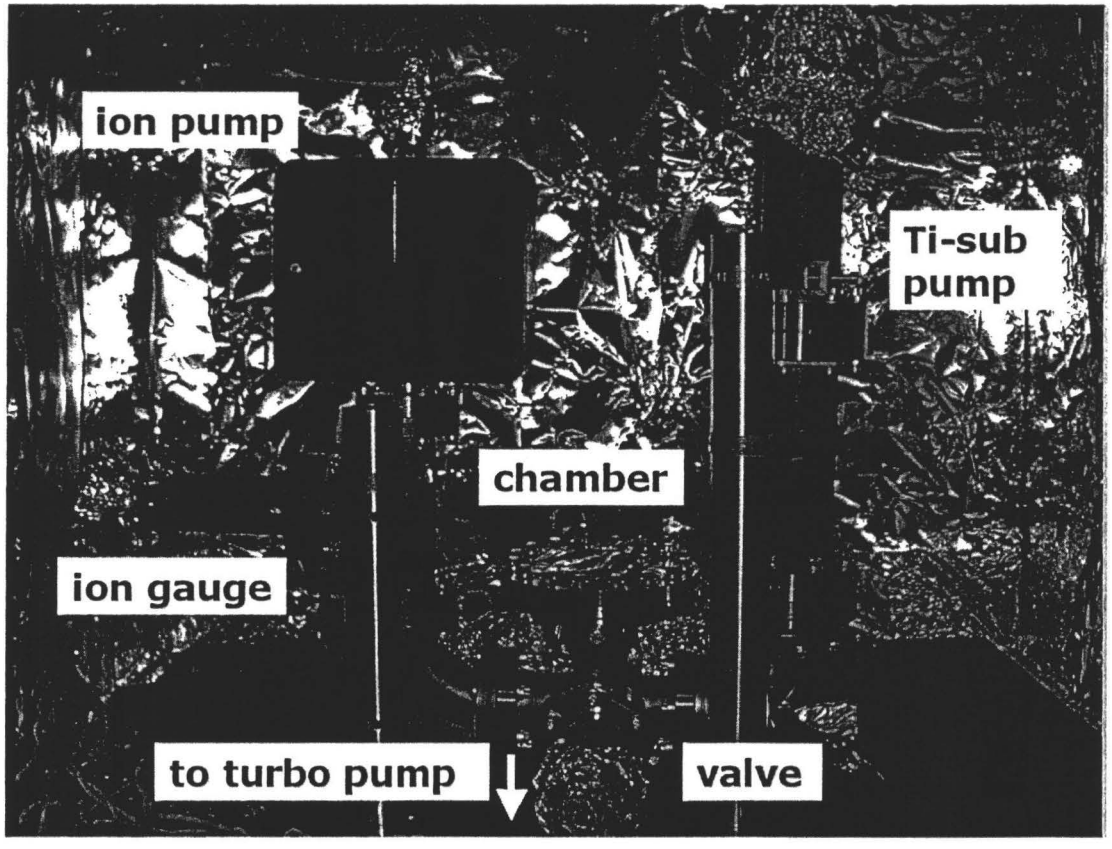

Figure 5.1: Vacuum system inside the furnace.

A nude ion gauge from Duniway is used to monitor the pressure inside the vacuum system. The maximum starting pressure is 1×10^{-3} torr and lowest pressure it can measure is 2×10^{-11} torr.

We also use a turbo pump backed by a dry scroll pump to pre-pump the system before the second stage of bake-out. A glass Bayard-Alpert type ion gauge is used to measure the pressure at the same time. The maximum operating pressure for this gauge is 1×10^{-3} torr.

5.2 Pre-bake

Table 5.2 contains a list of the vacuum hardware for our system. All the parts before the zero-length adaptors in the table, and two of the zero-length adaptors must be pre-baked. This will turn the stainless steel from a silver color to more of a gold-bronze color, an indication of a chromium-oxide layer formed. This reduces the water diffusion and hydrogen desorption from the stainless steel parts.

Item	Company	Part Number	Quantity
vacuum chamber, spherical octagon	Kimball	MCF600-S0200800-A	1
re-entrant flange, custom made	Kimball		1
UHV all-metal valve, 2-3/4 CF	Varian	9515027	1
blank flange, 6 CF	Duniway	F600-000N	1
cross, 2-3/4 CF	Duniway	CR-275	1
elbow, 2-3/4 CF	Varian	FE0150	2
tee, 2-3/4 CF	Varian	FT0150	1
nipple, 3-3/8 CF	Varian	FNF0200	2
zero-length adaptor, 3-3/8 CF to 2-3/4 CF, 2 for TSP, 2 for bellow	Duniway	A338TX275T	4
bellow, 3-3/8 CF	Duniway	FX-338	1
nipple, 2-3/4 CF	Duniway	NP-275	1
reducing nipple 4-1/2 CF to 2-3/4 CF	Varian	FA04500275L	1

Table 5.2: Vacuum hardware

The parts are pre-cleaned with acetone and Kimwipes. They are then wrapped with oil-free aluminum foil (Fisher Part No. 01-213-102). The shiny side of the foil should face toward the parts. They are then baked at 400 °C for about 2-3 days. Care must be taken when baking to not damage the knife edges on the parts.

We have used three different furnaces to pre-bake the vacuum parts. The first one is a small furnace in ABB 439* with a volume of about 1 ft^3. It was used to bake all the small parts, but it was too small for the vacuum chamber. The second furnace is located in ABB 444* and big enough for the chamber, but the controller is broken so we had to use a thermocouple to monitor the temperature and manually control the temperature. The third one is located in Accelerator Building and has a size of 5 ft× 5 ft× 5 ft. One should contact Chris Brooks in Engineering Physics to use it.

Vacuum viewports and feedthroughs are normally not pre-baked.

5.3 Vacuum Cleaning

Vacuum cleaning is the most important step in reaching UHV. If the cleanness of one part is suspicious, it must be cleaned again. All the cleaning except pre-cleaning must be done under a fume hood (we used the one in ABB 245 †).

Following is a set of instructions for cleaning the parts.

5.3.1 Pre-cleaning and Degreasing

I. Detergent immersion with ultrasonic agitation

*contact Jim Garret in BIMR to use it.

†contact Andy Duncan, ext 26893.

Put the parts to be cleaned into a large, clean beaker. The beaker should be rinsed with tap water and wiped with methanol and Kimwipes. Cover the parts with warm tap water and add 1% by volume of detergent (Liqui-Nox, from Alcohox, obtainable from Science Stores). Agitate in a ultrasonic cleaner for half an hour. Rinse in running tap water and dry. This step can be done outside the fume hood.

II. Acetone immersion with ultrasonic agitation

Put the parts into a large clean beaker and immerse in acetone. Use clean aluminum foil to cover the top of the beaker. Agitate in a ultrasonic cleaner for 10 minutes. Dump the acetone in the chemical waste bottle. Rinse the parts in running tap water and air dry.

III. Methanol vapor degreasing

The setup can be borrowed from David Venus' lab. Fig. 5.2 shows a schematic of the setup.

Put about 2-3 mm of methanol in the beaker. Put small parts inside a wire-frame basket and hang large parts from the bar. Try to face the larger surfaces of the parts towards the bottom of the beaker. Cover the beaker with clean aluminum foil and put the beaker on top of the hot plate. Slowly turn up the temperature and keep an eye on the methanol. Don't let the methanol boil. After a while, there should be methanol droplets dripping from the basket or the large parts. Continue heating for 20 minutes.

Dump the methanol in the chemical waste bottle. Rinse the parts in running tap water thoroughly.

IV. Deionized water rinse and immersion with ultrasonic agitation

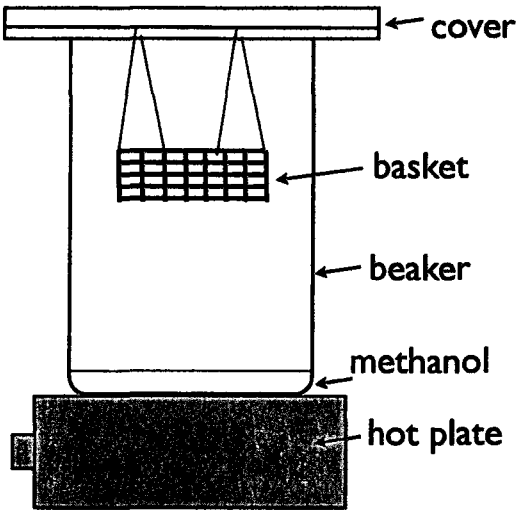

Figure 5.2: Schematic of vapor degreasing setup.

Deionized water can be obtained from Kari Dalnoki-Veress' lab (ABB 440) or Peter Kruse's lab (ABB A101).

Rinse the parts using deionized water. Put the parts into a clean beaker and immerse in deionized water. Use clean aluminum foil to cover the beaker. Agitate in the ultrasonic cleaner for 10 minutes. Dry under the flow hood.

V. Repeat step II-IV if necessary

5.3.2 Chemical Cleaning of Stainless Steel – Non-trap Electrodes

The solution is from Ref. [76], page 15, SS-1. Always add acid to water, slowly; do not add water to concentrated acid. Do not use chemical cleaning for the trap parts; the surface becomes rough after the chemical cleaning.

Solution:	Tap water	750 ml
	HCl (concentrated)	250 ml
	HNO_3 (concentrated)	200 ml

I. Agitate for 30 seconds in the solution. The solution left should be disposed of with acids in appropriate waste container.

II. Rinse thoroughly in running tap water. The first rinse after the acid immersion should be disposed of in appropriate waste container. Immerse the parts in concentrated HNO_3 solution.

III. Repeat step I and II if necessary for a uniform surface.

IV. Rinse in running hot tap water for 10 minutes.

V. Rinse in two changes of deionized water. If there are deep recesses or holes in the parts being cleaned, boil in deionized water.

VI. Rinse in methanol.

VII. Dry under flow hood.

5.3.3 Electropolishing Trap Electrodes

Electropolishing is an electrochemical process which polishes a metal surface by removing a microscopic amount of material from the work piece. The solution is from Ref. [76], page 22, EPSS-6. This bath can be used with an AC current source, but we use a DC source. Fig. 5.3 shows the schematic of the setup.

Nitric/Acetic Acid Bath:	Nitric Acid	70%
	Acetic Acid	30%
	Current density (amp/ft^2)	75 minimum
	Temperature (°C)	24 maximum

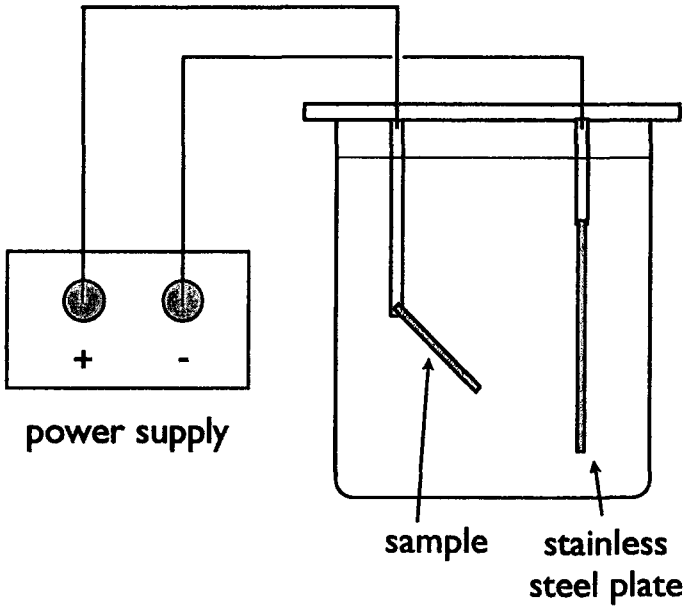

Figure 5.3: Schematic of the electropolishing setup.

The parts to be cleaned are connected to the positive terminal of the DC power supply. The power supply we use is a Protek 3033B. Only the trap parts (rods and tubes) need electropolishing. The optimum time to get a smooth surface is 3 minutes at 1.5 A for the rods and 2 minutes at 1.0 A for the tubes.

5.4 Trap Assembly

The trap assembly should be performed under the flow hood. Usually we put layers of clean aluminum foil (Fisher Part No. 01-213-102) on top of the table as

working space. Care must be taken to prevent organic body particles such as hair or skin flakes entering the vacuum system. It is good practice to dress in a long-sleeved lab coat, especially in the summer time. Gloves must be worn at all times because body oils are one of the contaminations which can prevent us reaching UHV. Note that latex gloves are soluble in acetone so non-latex gloves are preferred during the assembly. Non-latex nitrile gloves can be purchased from the Science Store.

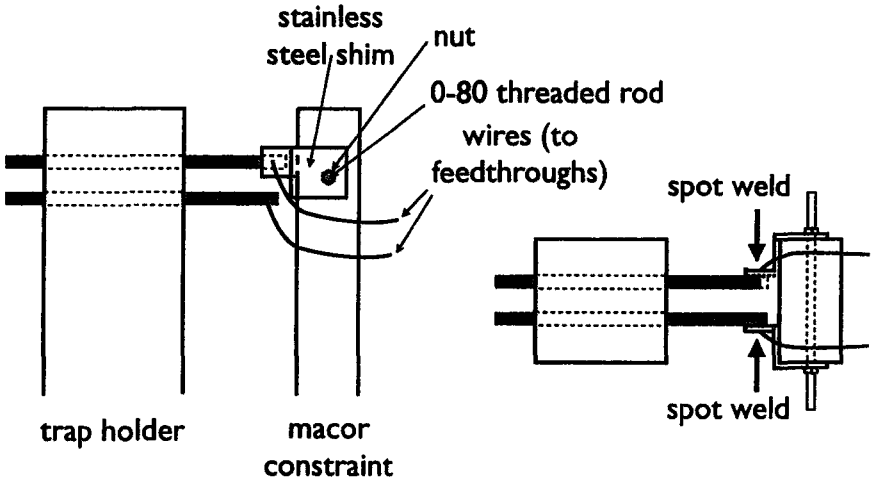

Figure 5.4: Schematic of the macor constraint bracket. The left picture is the side-view and the right one is the top-view. This figure is not to scale.

Normally we assemble the trap on the base plate first. We thread two ground rods into the trap holder, then slip on the polyimide tubes and tube electrodes. One end of the rods is spot welded to an L-shape made of stainless steel shim, and the shim is bolted to a 0-80 threaded rod which passes through a hole in the macor constraint bracket. This will fix the position of the rods (see Fig. 5.4) and help in adjusting

the tube position. The separation between the tube electrodes is adjusted to about 3 mm. A microscope is used to inspect if any polyimide is sticking out on the trap side. The tube end that is away from the trap is slightly crimped using a round-nose pliers in order to hold the tube electrode in place. We then thread two rf rods into the trap holder and fix their position using another macor bracket. At last, we mount two ovens and two electron-guns on the base plate.

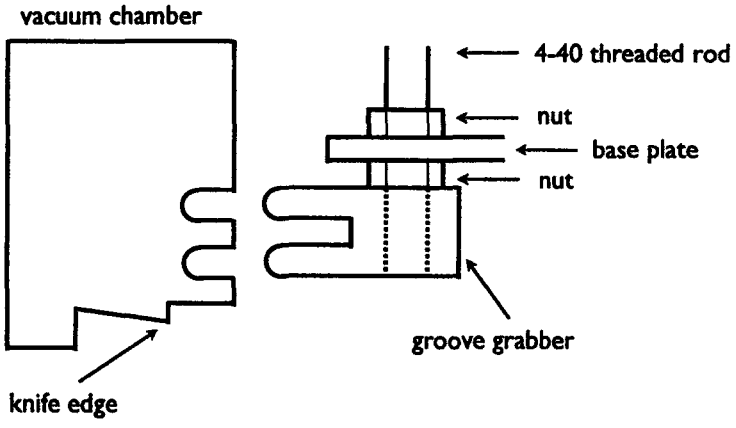

Figure 5.5: Cross section of the mounting (not to scale).

The trap, ovens and electron guns are all mounted on the base plate. Mounting the base plate to the chamber is tricky. We attach one groove grabber loosely on the base plate and mount the groove grabber to the chamber. The groove grabber is loosely attached so we can tilt the base plate to mount on another groove grabber which is attached to the chamber beforehand. The groove grabbers clamp four threaded 4-40 rods, onto which the base plate is bolted (see Fig. 5.5).

The dc and rf connections are made to the feedthroughs. We check electrical continuity of the leads before we close the chamber.

The seals in the vacuum system are made by ConFlat flanges. The Conflat system contains a sharp knife edge on each flange. These knife edges compress the soft copper gasket which flows under ductile stress to form a UHV compatible, bakeable seal. The bolts compressing the flange must be evenly tightened. Also, the leak-detector grooves on each flange should be lined up; this will facilitate leak testing the system. The 2.75" flanges are designed to have 12 ft-lbs of torque on each bolt, but in practice, the flanges are tightened to the point where the copper gasket can barely be seen between the flanges.

All the bolts and gaskets should be silver-coated except the ones to mount the top viewport on the re-entrant flange. This will make it easier to remove the flanges after the baking. Table 5.3 is a list of bolts and gaskets need to assemble the vacuum system.

Item	Company	Part Number	Quantity
bolts, 2-3/4 CF, with platenuts	Duniway	SPBN28-125-275	60
bolts, 2-3/4 CF, tapped hole	Duniway	SBX-28-087	72
bolts, 3-3/8 CF, with platenuts	Duniway	SPBN24-175-338	6
bolts, 3-3/8 and 6 CF, tapped hole	Duniway	SBX-24-125	56
copper gasket for 2-3/4 flange	Duniway	SG-275	21
copper gasket for 3-3/8 flange	Duniway	SG-338	5
copper gasket for 6 flange	Duniway	SG-600	2

Table 5.3: Bolts and gaskets

5.5 Baking

Table 5.4 is a list of parts needed for baking the vacuum chamber.

Item	Company	Part Number
Type K thermocouples	Omega	XC-20-K
Tape heaters	Omega	FGS101-040
Bar heaters	Omega	OT-1202/120
High temperature ring terminals	Omega	RLNI-22
Bar heater hook-up wires	Omega	HTMG-1CU-316S/C
Insulating boards	McMaster CARR	9391K52
Angle posts	T&T	E-35-144-G
Swivel casters	T&T	361RH
Gusset plates	T&T	GP3X3
Hex cap screws	T&T	075-442
Hex nuts	T&T	087-016
Flat washers	T&T	154-016

Table 5.4: Checklist for baking

The furnace is a 2 ft×3 ft×3 ft box made of angle posts and insulating boards. The 1-1/2" thick Calcium Silicate insulating boards can stand a maximum temperature 650 °C and have a low heat-flow rate. A hole is cut in the bottom to provide access for the turbo pump. Bar heaters are distributed at different locations to evenly heat the whole furnace (see Fig. 5.6).

Once the whole vacuum system is assembled and moved into the furnace, we connect the valve to the turbo-pump station through a flexible bellows. Thermocouples are put at various places to monitor the temperature during the bake-out. The thermocouples are wrapped with insulating tape to prevent shorting. We then wrap the whole system with aluminum foil and tape heaters. Care must be taken to avoid placing tape heaters directly on flanges and windows. The bar heaters are also placed under and around the chamber. We then close the furnace and start baking.

The temperature measured by the thermocouples is read using a LabView program. The temperature is slowly ramped up to 200 °C and kept there for about 3-4 days until the pressure reaches equilibrium. Normally the pressue is in the low 10^{-7}

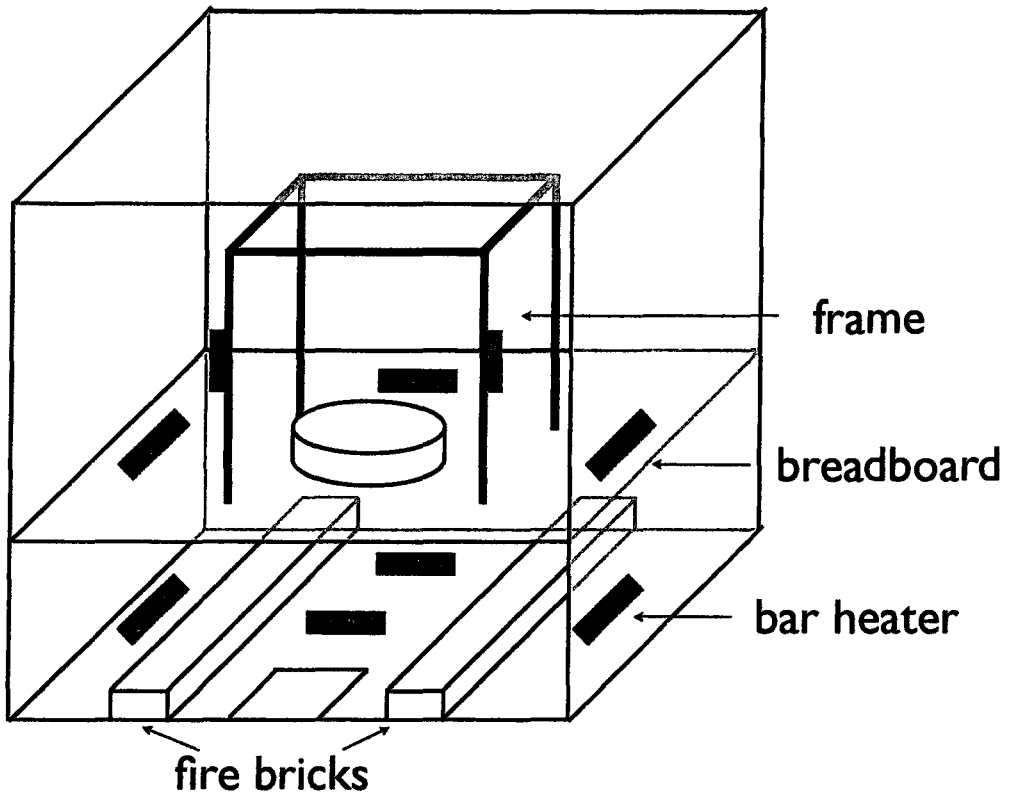

Figure 5.6: Schematic of the furnace.

torr. We then turn on the ion pump and nude ion gauge, close the valve and start the second stage of baking. The whole process usually takes about 1-2 weeks.

Chapter 6

Laser System

All laser beams used in our experiments have frequencies lying in the ultraviolet. The laser system is divided into four sets of beam lines:

- the photoionization beam, used to ionize the neutral atoms and produce ions.
- the Raman beams, used to manipulate the qubit states $|^2S_{1/2}, F = 3, m_F = -3\rangle \equiv |\downarrow\rangle$ and $|^2S_{1/2}, F = 2, m_F = -2\rangle \equiv |\uparrow\rangle$ through two-photon stimulated-Raman transitions.
- the Cycler and the Red Doppler, which are used for optical pumping, Doppler cooling and driving the cycling transition for detection.
- the Repumper, used to clear out $|^2S_{1/2}, F = 3, m_F = -2\rangle$ level without affecting the $|\downarrow\rangle$ state.

For each of the beam lines, the wavelength of the laser is around 280 nm – except the photoionization laser, which operates at 285 nm. We have one dye laser and two fibre lasers as our laser sources. The wavelength of the dye laser can be varied from 555 to 590 nm. The fibre lasers output 1120 nm infrared light. In both cases we need to make use of frequency-doubling to get the right wavelength. One commercial frequency doubler is used to frequency-double the dye laser, and four frequency-doubling cavities were built in the lab for the fibre lasers. Finally, the laser frequency of each beam has to match the respective magnesium transition frequency within

several MHz, so we use Doppler-free saturated absorption spectroscopy of iodine to adjust or lock the lasers to the required frequency.

6.1 Laser Sources

6.1.1 Dye Laser

The Coherent-699 dye laser is used for photoionization and for the Raman beams because of its wide range of lasing wavelengths (tens of nanometers depending on the dye) and its high power. The dye we use is Rhodamine-19. A 10 W Verdi diode-pumped solid state laser is used to optically pump the dye laser. The cavity is formed by four mirrors, three concave and one planar, in a bow-tie configuration.

The Coherent-699 has a Brewster plate used to scan the frequency over large ranges, and an internal cavity assembly (ICA) consisting of a thin and a thick etalon. The ICA provides fine adjustment of frequency. Frequency stability is provided by locking to an external reference cavity and a side-lock scheme is used for this purpose. The linewidth of the dye laser output is measured to be $\approx$ 10 MHz.

The dye laser and its pump laser are located on a small, separate optical table to prevent mechanical vibrations from being transferred to the main optical table. The output of the dye laser is coupled through a single-mode optical fibre to the main optical table.

The dye laser outputs about 1.0 W of green light at 570 nm. We are able to couple about 0.6 W of the light to the main optical table. Once on the main table, the beam is then split in two: one beam goes to the diagnostics and the other is sent into a frequency-doubling cavity to produce 285 nm UV light.

The diagnostics consist of a Burleigh WA-1000 wavemeter and a Thorlabs SA200-5A scanning Fabry-Perot interferometer. The wavemeter has a resolution of 1 pm (1 GHz at 560 nm), and it is used to get the frequency within 1 GHz. The Thorlabs Fabry-Perot interferometer has a free-spectral-range (FSR) 1.5 GHz. We can send several beams into the interferometer to compare their relative positions in the frequency domain. Some of the light is also sent to an iodine spectrometer (see Section 6.3)

6.1.2 Fibre Lasers

Two Koheras A/S Boostik fibre lasers that operate in the infrared produce the beams used for the Cycler, Red Doppler and Repumper beam lines. The fibre laser can provide both a high power and a very stable frequency. The gain medium of the laser is a fibre with a ytterbium-doped inner core. The fibre is pumped by a 980 nm semiconductor laser. A Bragg grating is etched into the fibre which gives the fibre laser its narrow linewidth ($\approx$ 40 kHz). The output power then is increased by an internal amplifier to 1-2 W. Table 6.1 summarizes the technical specifications of the two fibre lasers.

Laser	Wavelength Range (nm)	Max. Output Power (W)	Temperature Tuning (pm/°C)	PZT Tuning (pm/V)
CYC, RD	1118.20 - 1180.80	2.0	15	0.1
RP	1121.30 - 1121.44	1.3	11	-0.1

Table 6.1: Technical specifications of two fibre lasers

The wavelength of the fibre laser can be changed by two mechanisms: varying the temperature of the fibre or changing the voltage on a piezo-electric transducer (PZT) connected to the fibre. Large wavelength changes can be accomplished by changing the temperature of the fibre, which subsequently changes the index of refraction of

the fibre. For every 1 °C change of temperature the wavelength is changed by about 10 pm. The temperature can be tuned from room temperature to about 40 °C. Compared to the temperature tuning, the voltage tuning is much faster but can only change the frequency over a small range. The change of the frequency is achieved by stretching the fibre with a PZT and changing the period of the grating length by a small amount. 10 V of voltage change on the PZT induces about 1 pm change in wavelength. Notice the sign difference in the PZT tuning coefficients for two fibre lasers (see Table 6.1).

The output of fibre laser consists both the signal light and amplified spontaneous emission (ASE [77]). The laser beam is coupled to the optical table using a single-mode fibre and collimated by an aspheric lens. The polarization of the output beam is elliptical, so a $\lambda/4$ waveplate is used to change the polarization to linear and a $\lambda/2$ waveplate is used to rotate the polarization if required. After we turn on the lasers each day, there is about a two-hour waiting time before the polarization settles down. The fibre laser is also very sensitive to back-reflected light so an optical isolator is placed right after the $\lambda/2$ waveplate.

The 2 W fibre laser broke in September 2006. We have sent it back for repair but haven't received it back yet. The 1.3 W fibre laser works fine, and most of the data in the latter sections of this thesis were taken using this laser.

6.2 Frequency Doubling

The dye laser output is frequency-doubled from visible to ultraviolet using a commercial Wavetrain doubler. The output of the fibre lasers is frequency-quadrupled from infrared to ultraviolet, using cavities that were designed in-group by Jason

Nguyen. Two cavities were made for each fibre laser: one LBO cavity to double infrared to visible and a subsequent BBO cavity to double visible to ultraviolet.

6.2.1 Wavetrain Doubling Cavity

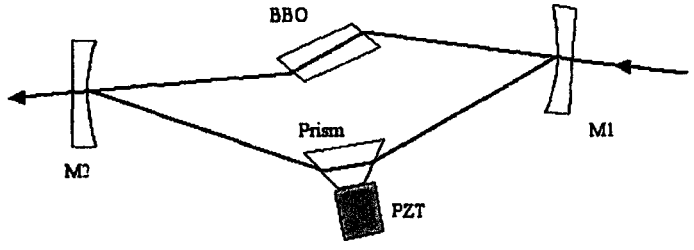

Figure 6.1: Schematic of Spectra-Physics Wavetrain frequency-doubling cavity. Figure courtesy of Laura Toppozini.

The Wavetrain is a frequency-doubling cavity that uses a beta-barium borate (BBO) crystal. It was designed by Spectra-Physics (now Newport). The beam is mode-matched using two spherical lenses and is steered into the Wavetrain using two flat mirrors. The light enters the cavity through a spherical mirror M1 (see Fig. 6.1). From here it passes through the Brewster-cut crystal and reaches a second spherical mirror M2, which also serves as an output coupler. The beam then passes through a prism and returns to M1. The prism is mounted on a PZT stack which is used to

change the length of the cavity by changing the optical length of the path passing through the prism. The cavity is kept resonant using the Pound-Drever-Hall locking scheme [78, 79].

6.2.2 LBO Cavity

We are using a lithium borate (LBO) crystal to frequency-double the fibre laser into the visible. The crystal is 7 mm long and has a 4 mm × 8 mm aperture. The crystal surfaces are cut at Brewster's angle. The crystal is put inside an oven and noncritical phase matching [80] is accomplished by heating the crystal to 107 °C.

Boyd and Kleinman [81] have discussed the interaction of focussed Gaussian beams with nonlinear crystals. Using their results, we can calculate the optimum waist of the fundamental light inside the crystal for our given crystal length and the nonlinear conversion efficiency κ_0. The optimum waist for our crystal is 25 μm, and the theoretical conversion efficiency is calculated to be 80×10^{-6} W^{-1}.

A resonant cavity is built around the crystal in order to provide the optimum waist and increase the intensity of the fundamental light inside the crystal. The output power of the second harmonic light P_2 will be determined by the power of the fundamental light P_1 and the nonlinear conversion efficiency κ_0:

$$P_2 = \kappa_0 P_1^2. \tag{6.1}$$

Frequency-doubling is a nonlinear process: doubling the fundamental power will quadruple the second-harmonic power.

We are using a four-mirror bow-tie configuration (Fig. 6.2). This setup supports a traveling wave, which can prevent reflecting any light back to the pump laser and avoid the intensity modulation of the pump light inside the crystal. The optimum 25

μm waist is achieved by two curved mirrors (M3 and M4) with a radius of curvature 75 mm, spaced roughly 80 mm apart. One of these mirrors is mounted on a PZT to allow the cavity length to be stabilized, and the other one serves as an output coupler. Two flat mirrors are used to close the cavity, and one of them is the input coupler with 98% reflectivity. The input coupler is chosen so that the transmittance of the mirror is about the same as the cavity loss. The incident angle on the curved mirror is chosen to compensate the astigmatism introduced by the titled crystal surfaces [82]. The mirrors other than the input coupler are specially coated to have better than 99.5% reflectivity by Precision Photonics.

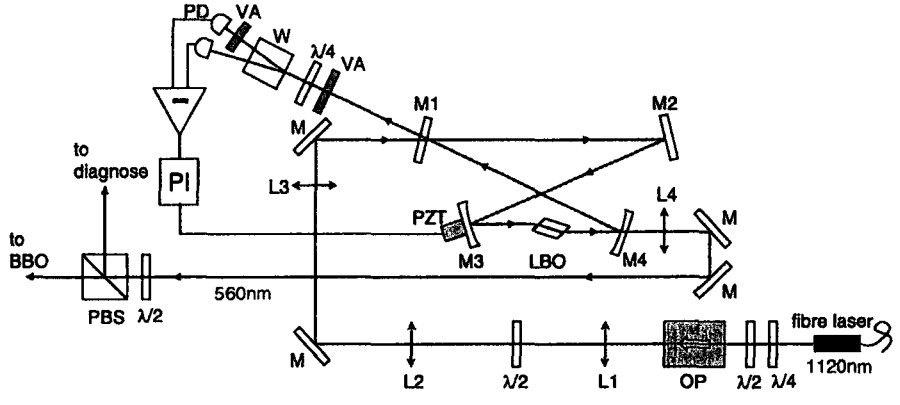

Figure 6.2: Schematic of the LBO cavity. OP: optical isolator. W: Wollaston prism. VA: variable attenuator. PBS: polarization beam splitter cube. PD: photodiode. PI: proportional and integral gain for the feedback loop. M's and L's are mirrors and lenses.

The cavity length is stabilized using the Hänsch-Couillaud scheme [83]. In principle, the scheme requires only a $\lambda/4$ waveplate and a $\lambda/2$ waveplate. Additional birefringence in the input coupler and the attenuator shifts the lock signal. This can be corrected with a variable attenuator in front of one of the photodiodes. The polarization of the input light is tilted using a $\lambda/2$ waveplate to provide mainly p-polarization, but also a small amount of s-polarization. The s-polarized light is totally reflected because of the Brewster-cut crystal, and the reflection of the p-polarized light depends on whether the cavity is on resonance. The s-polarized light then serves as a phase reference to probe the phase shift of the p-polarized light. This locking scheme outputs a nice dispersion curve as an error signal for a loop filter. The loop filter then provides the proportional and integral gain for the error signal and feeds its output to a PZT driver. The PZT driver amplifies the signal and applies the voltage to the PZT to keep the cavity length stable.

Under normal conditions, the 1.3 W fibre laser outputs about 900 mW of non-ASE IR. We can measure the light reflected from the input coupler when the cavity is locked and unlocked. The difference tells us how much light is coupled into the cavity. Normally we get 95% input coupling efficiency with a 98% input coupler. The circulating power inside the cavity can be derived from the fundamental power transmitted through mirror M2 and the transmissivity of M2. We measure the circulating power to be 72.9 W. The ratio between the input power and circulating power gives the cavity loss. The loss is about 1.2%, which includes 0.7% of linear loss due to the loss of mirrors and crystal, and 0.5% of nonlinear loss due to the second harmonic generation. The power of the second harmonic output is 270 mW, which gives a single-pass efficiency 65×10^{-6} W^{-1}. This value agrees reasonably well with the theoretical value 80×10^{-6} W^{-1}.

6.2.3 BBO Cavity

We are using a BBO crystal to frequency-double the visible light into the UV. The crystal is 7 mm long and has a 4 mm × 8 mm aperture. The crystal surfaces are cut at Brewster's angle. Critical Type-I phase matching [80] is accomplished by angle-tuning the crystal. The optimum waist inside the crystal is calculated to be 22 μm, and the theoretical single-pass conversion efficiency to be 100×10^{-6} W^{-1}.

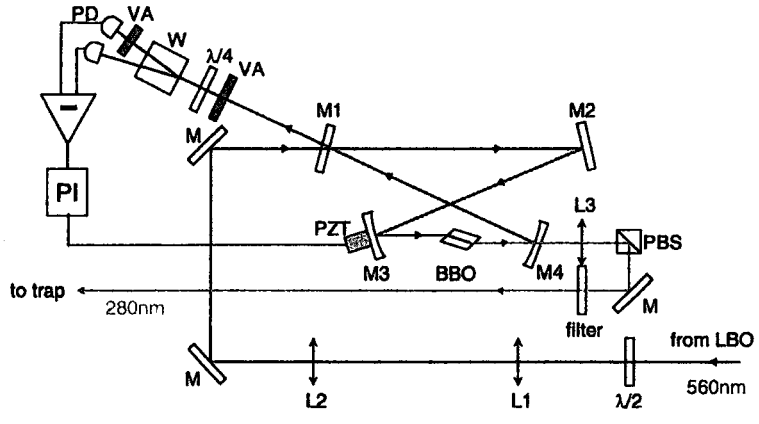

Figure 6.3: Schematic of the BBO cavity. W: Wollaston prism. VA: variable attenuator. PBS: polarization beam splitter cube. PD: photodiode. PI: proportional and integral gain for the feedback loop. M's and L's are mirrors and lenses. L3: cylindrical lens.

The BBO cavity (Fig. 6.3) is similar to the LBO cavity. We are using a four-mirror bow-tie configuration, and the Hänsch-Couillaud scheme to stabilize the cavity. BBO

crystal has a very soft surface. It also is hygroscopic, so extra care needs to be taken to ensure the crystal stays dry. The cavity is shielded by a home-made board box and desiccants are placed inside the box. The output UV beam is elliptical because of walk-off [84], so a cylindrical lens is used to form a circular beam.

Under normal conditions, we are able to couple 83 % of the 250 mW green light into the cavity. We are using a 98% input coupler; the cavity loss is about 2.0%, most of which is linear loss. The power inside the cavity is 10.4 W and the UV generated is 3 mW, which gives a single-pass efficiency 47×10^{-6} W^{-1}. This value is only about half of the theoretical value 100×10^{-6} W^{-1}. It is always difficult to get a high single-pass efficiency for the BBO crystal because of its hygroscopic properties.

6.3 Doppler-Free Saturated Absorption Spectroscopy

We use Doppler-free saturated absorption iodine spectroscopy [85] to characterize the frequency of our lasers. The iodine molecule has many well-defined transitions in the visible range so it is a useful frequency reference.

6.3.1 Theory

In a typical vapor-cell arrangement, atomic transitions are broadened by the Doppler shifts associated with the motion of the atoms. Suppose an atom is moving with velocity $\vec{v}$ and its rest-frame transition frequency is ω_0. It will absorb light from a narrowband laser with frequency ω and wavevector $|\vec{k}| = \omega/c$, if the Doppler condition

$$\omega = \omega_0 + \vec{v} \cdot \vec{k} \tag{6.2}$$

is satisfied. Hence in a thermal sample of atoms, even if the laser light is off-resonant with the transition, $|\omega - \omega_0| \gg 0$, there still will be some atoms with a large Doppler shift $\vec{v} \cdot \vec{k}$ to fulfill Eqn. (6.2). At room temperature, the broadened linewidth of a sample of iodine molecules is about 1 GHz.

We now treat the iodine molecule as a two-level system. Suppose the atoms are illuminated by a laser beam traveling along the z-axis. For fixed laser frequency ω and transition frequency ω_0, only the atoms in a narrow velocity range Δv_z will satisfy condition Eqn. (6.2) and be resonant with the laser. This leads to a population transfer from the ground-state to the excited state, but only for atoms whose velocities fall in this narrow velocity interval. Δv_z is determined by the linewidth of the transition, which is much less than the Doppler-broadened linewidth. In the plot of velocity distribution (Fig. 6.4) for the ground-state, we see a broad Gaussian distribution with a hole at $v_z = (\omega - \omega_0)/|\vec{k}|$, a so-called "Bennet hole" [86]; in the plot for the excited state, we see a peak at the same velocity.

An interesting phenomena is that when we scan the laser frequency, the absorption profile shows no holes at all, even though at each frequency ω the monochromatic laser burns a Bennet hole into the velocity distribution. The reason is the Bennet hole occurs at every frequency when the frequency is scanned, hence affecting the absorption profile in a uniform manner.

Let us now consider a situation where there are two overlapping beams present. One is a strong, saturating beam (pump beam) traveling with $\vec{k_1} = (0, 0, k_1)$ and frequency ω_1, and the other one is a counter-propagating, weak probe beam with $\vec{k_2} = (0, 0, -k_2)$ and frequency ω_2. The frequency difference between these two beams is set to a constant $\Delta\omega = \omega_2 - \omega_1$. In general, the absorption of the weak probe beam will be independent of the presence of the strong pump beam, because they are traveling in opposite directions, so they strongly interact with *different* velocity

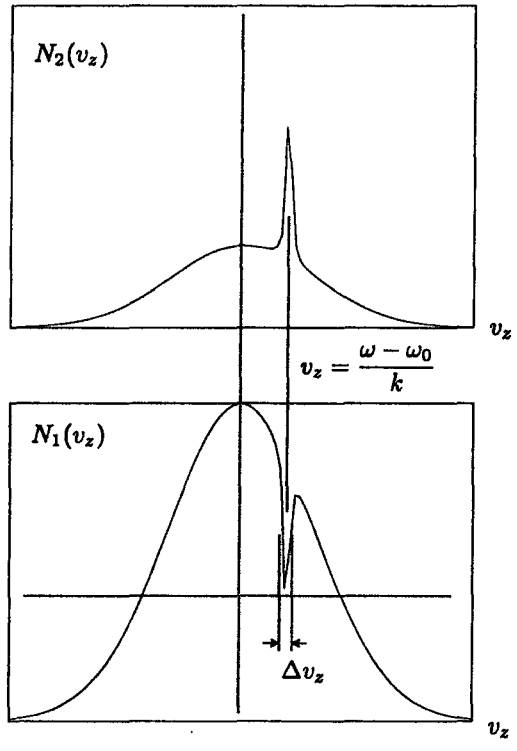

Figure 6.4: Schematic of the velocity-selective saturation of a Doppler-broadened transition. We can see the Bennet hole in the lower- and the Bennet peak in the upper-state population distribution $N_i(v_z)$.

classes of atoms. However, this is not true when the same velocity class of atoms satisfies the Doppler condition for both beams:

$$\omega_1 = \omega_0 + v_z k_1,$$

$$\omega_2 = \omega_0 - v_z k_2.$$

In this special case, the atoms will hardly absorb the weak probe beam, because most of the atoms have been excited by the strong pump beam. If we scan the probe beam frequency and keep the frequency difference $\Delta\omega$ constant, observing the transmitted probe beam power, we will see a narrow peak at frequency $\omega_2 = \omega_0 + \frac{1}{2}\Delta\omega$ in the

absorption profile of the probe beam. Here we have used the approximation that $v_z k_1 \approx v_z k_2 \ll \omega_0$.

One of the choices of the detuning is $\Delta\omega = 0$, so the atoms with $v_z = 0$ will be resonant with both beams. Since the atoms are most likely to have a velocity $v_z = 0$, the absorption signal is the strongest. In our experimental setup, we choose $\Delta\omega = 80$ MHz because the use of an acoustic-optic modulator (AOM) gives us the ability to amplify the signal using a lock-in amplifier. The signal will be reduced to about $\exp(-80\text{MHz}/1\text{GHz}) \approx 0.92$, where the 1 GHz is the Doppler linewidth of iodine molecular at room temperature.

6.3.2 Experimental Setup

Part of the green beams from the LBO cavity and fibre output from the dye laser are used for iodine spectroscopy. The beam is sent through an angled piece of glass. Each surface picks off about 4% of the incoming beam due to Fresnel reflection. These two beams are used as weak probe and reference beams and are sent through the iodine vapor cell. The transmitted beam is sent through an 80 MHz AOM to frequency modulate the pump beam. The first-order diffracted beam is then sent through the vapor cell to approximately overlap with the probe beam, but from the opposite directions. The probe and reference beams illuminate two photodiodes after passing through the vapor cell. The signals from two photodiodes are subtracted to cancel out the Doppler profile. Two variable attenuators are used before the photodiodes in order to set the subtracted-signal offset to zero.

We use an 85 kHz sine wave to frequency modulate the 80 MHz AOM; generating a derivative of the absorption signal. The signal from the photodiodes is fed into

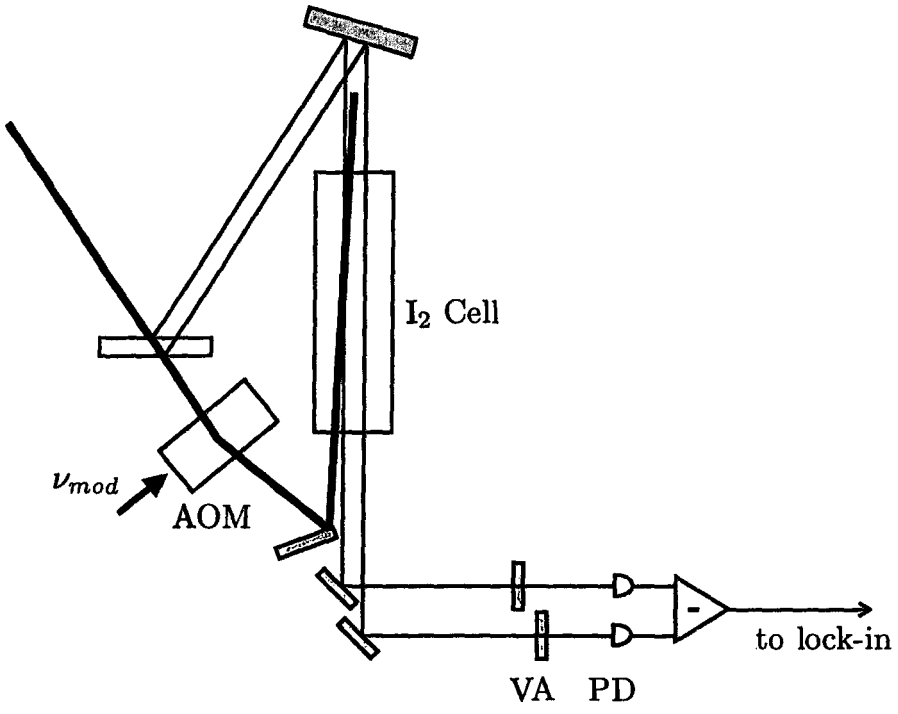

Figure 6.5: Schematic of the iodine spectroscopy setup. VA: variable attenuator. PD: photodiode. AOM: acoustic-optic modulator. $\nu_{mod} = 80$ MHz.

a lock-in amplifier, which is used to increase the signal-to-noise ratio and output a dispersion curve.

We obtained the iodine spectrum near the transition $^2S_{1/2} \leftrightarrow {}^2P_{1/2}$ of $^{24}Mg^+$ ion ([87], around 560.707 nm on the wavemeter before doubling from visible to UV). Since the cycler fibre laser is broken, we presently have to use this transition to laser cool and detect ions. The measurement is done by slowly varying the voltage adjustment of the fibre laser ($\sim$ 50 V) to change the laser frequency. The frequency axis is calibrated by steering part of the green beam into a Fabry-Perot interferometer. The frequency change is determined by comparing the change of the peaks on an oscilloscope to the

free spectral range of the etalon. The details of this measurement can be found in Laura Toppozini's thesis [22].

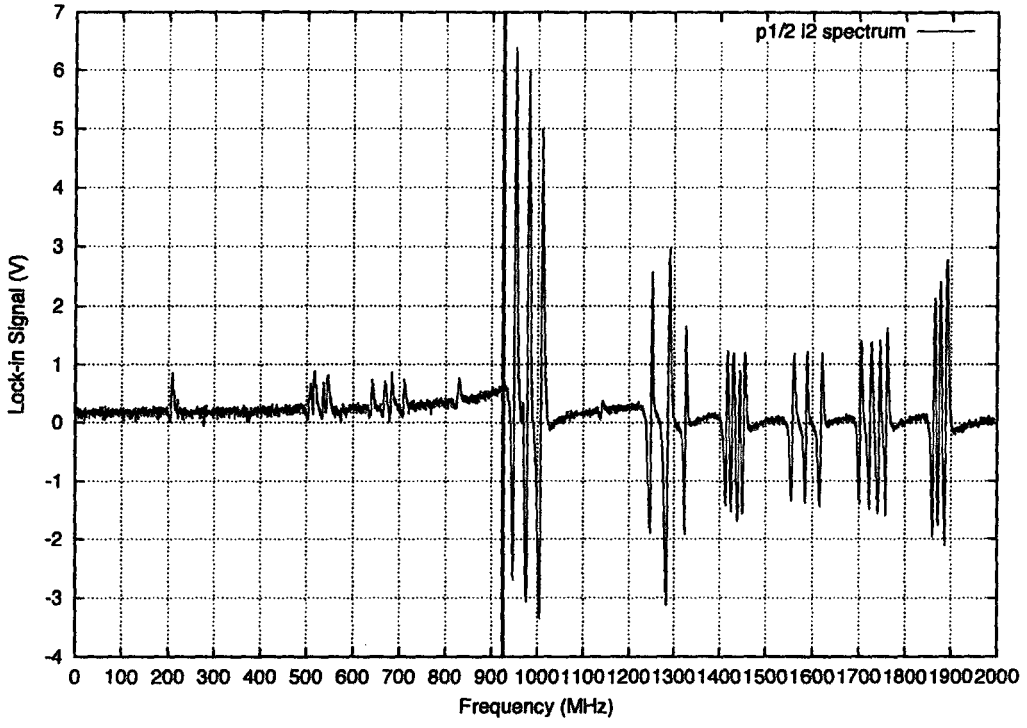

Figure 6.6: Iodine spectrum near 560.707 nm. The line labels the $^{24}Mg^{+}$ transition $^{2}S_{1/2} \leftrightarrow {}^{2}P_{1/2}$.

Chapter 7

Imaging System

The imaging system is used to collect the ions' fluorescence so we can (a) form an image of trapped ions and (b) determine the internal state of the ion. A schematic of the imaging system is shown in Fig. 7.1. The fluorescence from the ion passes through the top viewport and is collected by an objective (Mitutoyo M Plan UV 20x, numerical aperture 0.36, 10 mm focal length and 15 mm working distance). The objective is placed inside the re-entrant flange (see Section 4.3) so the trap centre is about the working distance away from the objective. The objective collimates the light and a subsequent lens L2 (CVI laser BICX-25.4-50.6-UV, 50 mm focal length) focuses the light to form the first image. An adjustable aperture (Thorlabs SM1D12C) is placed at the first image's position to filter out the background light and light scattered from the trap electrodes. The combined magnification of L1 and L2 is 5×. After the aperture, the fluorescence passes a doublet L3 (two Newport SPX 025, 150 mm focal length) and is focused on one of the two photon detectors. The magnification of L3 is 8×, for an overall magnification of 40×.

The photon detection is carried out by either a UV sensitive electron-multiplying CCD camera or a photomultiplier tube (PMT). The fluorescence is steered to one or the other detector using a removable mirror. The CCD camera used in the experiment is from Andor Technology (iXon DV887 ECS-UVB), which has single photon counting capability and specified 35% quantum efficiency at wavelength 280 nm. The camera has 512×512 active pixels and the pixel size is 16 μm $\times$ 16 μm. The camera is very

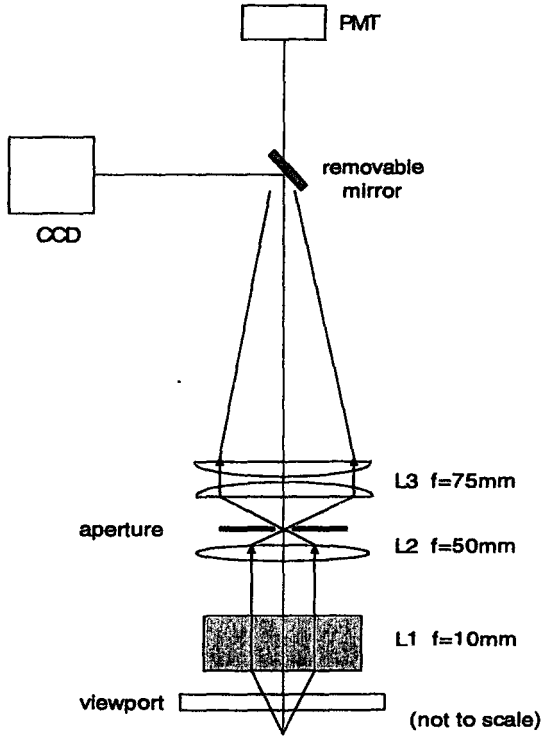

Figure 7.1: Schematic of the imaging system.

handy because it can help us to align the imaging system and form a real-time image of the trapped ions.

One disadvantage of the CCD camera is the delay between two acquisitions caused by the CCD readout process. So a high-speed PMT will also be used to take data. The PMT was purchased from Hamamatsu (Part No. H8259-01) and has specified 20% quantum efficiency at 280 nm. This unit takes +5 V dc voltage input and outputs a TTL-compatible pulse for every photon it detects.

7.1 Detection Efficiency

The overall detection efficiency of the system was calculated to be about 0.31% with the CCD camera. This includes several effects. A summary of various losses is listed in Table 7.1.

Objective Half Angle (°)	21.1	
Photon Collecting (%)	2.60	
Wire Mesh Open Area (%)	59.1	
Viewport Transmittance (%)	99.0	
Objective Transmittance (%)	60.0	
Lenses Transmittance (%)	98.5	
All optics transmittance (%)	58.5	
Quantum Efficiency (%)	35.0 (CCD)	20.0 (PMT)
Overall Collection (%)	0.31 (CCD)	0.18 (PMT)

Table 7.1: Detection efficiency of the imaging system.

Due to the ion's dipole radiation pattern and the solid angle of the detection system, only 2.60% of the scattered photons will fall onto the objective. Here we assume that we use $\hat{\sigma}_-$-polarized Cycler for the detection. The wire mesh (see Section 4.3) has a 59.1% open area. The viewport has an anti-reflection coating with greater than 99% transmission; the transmittance of the objective is 60% at 280 nm and the reflection loss due to each surface of the other lenses is 0.25%, which combines

to 98.5% transmittance. So the total loss due to the optics is about 58.5%. The quantum efficiency of the CCD camera is 35%, which gives us an overall collection of 0.31%.

7.2 Spherical Aberration

For a typical axial trap frequency $\omega_z/2\pi = 1$ MHz, 5 ions will be separated by about 5 μm [88]. So our imaging system should have a resolution better than 5 μm.

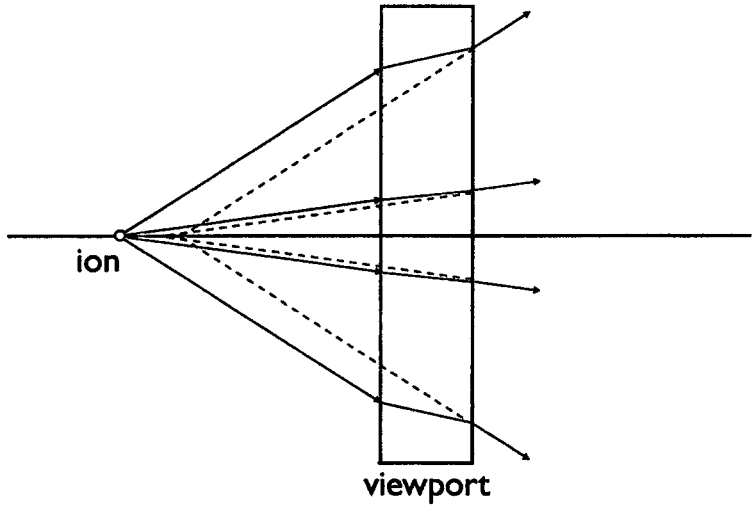

Figure 7.2: The viewport introduces spherical aberration.

The main aberration of the imaging system is spherical aberration introduced by the viewport. From Fig. 7.2, rays striking the viewport surface at greater distance from the optic axis are imaged in front of the paraxial image. The convex lens in the system will also introduce spherical aberration but fortunately in the opposite sense: the marginal rays focus to a point behind the paraxial image [89]. The spherical

aberration can be canceled out by varying the distance between the objective L1 and bi-convex lens L2.

Fig. 7.3 (a) shows a ray tracing diagram for an ion lying on the optic axis after lens L2. The distance between L1 and L2 was chosen to be 39.3 mm to minimize the spot size. We can see that most of the rays are focused down to a spot less than 1 μm in diameter. The magnification of the first stage is 5×, which means we can resolve better than 0.5 μm.

Fig. 7.3 (b) shows a ray tracing diagram for an ion off the optic axis by 100 μm. The spot size increases to 20 μm. Since the magnification for the first stage is 5×, ions separated by more than 4 μm will still be resolved. The ray tracing was done using OSLO *.

*Lambda Research Corp., Massachusetts, USA. http://www.lambdares.com/

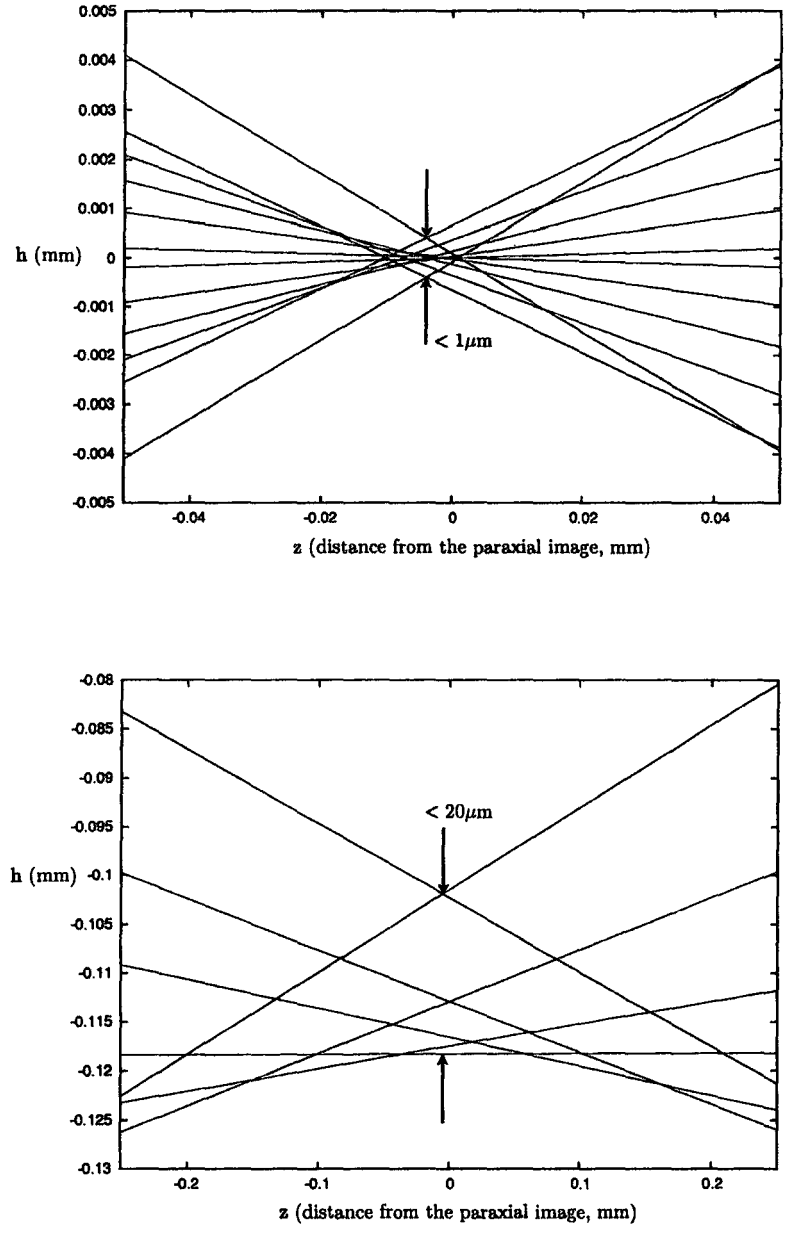

Figure 7.3: (a) Top figure, ray tracing with an ion on the optic axis. (b) Bottom figure, ray tracing with an ion off the optic axis by 100 μm.

Chapter 8

Operation of the Ion Trap

Our plan is to trap $^{24}Mg^{+}$ first because of its simple ground-state structure (no hyperfine splitting). Since the breakdown of the cycler fibre laser, we have set the frequency of the repumper to drive the $^{2}S_{1/2} \leftrightarrow {}^{2}P_{1/2}$ transition and use this laser for laser cooling and detection [38]. The dye laser output is used for photoionization (PI).

8.1 Alignment

The laser parameters for trapping $^{24}Mg^{+}$ are summarized in Table 8.1. The wavelengths listed here are for visible light, which will be frequency-doubled into the UV.

Laser	Visible wavelength on wavemeter (nm)	Max. UV output power (mW)	Waist at trap centre (μm)
RP	560.707	0.5	30
PI	570.593	1.0	30

Table 8.1: Laser parameters for trapping $^{24}Mg^{+}$.

The RP and PI beams are combined on a polarizing beam splitter cube. The polarization of the RP beam is parallel to the optical table, and that of the PI beam is perpendicular to the table. We set up the quantization magnetic field such that the RP beam has $\hat{\pi}$-polarization and PI beam has a combination of $\hat{\sigma}_{+}/\hat{\sigma}_{-}$. Both beams then pass a $\lambda/2$ waveplate and a $f = 50$ cm lens to focus near the trap centre.

The position of the trap centre is deduced by translating the imaging system (see Chapter 7) to focus upon recognizable parts of the trap electrodes with known positions. First, we focus the edge of two tube electrodes which are on the same rf ground rod, noting the micrometer reading of the imaging system. The geometric centre of the trap has position along the axial direction half way between the edges of the two tubes. The position in the radial direction is found by focusing on the edges of the rod electrodes.

The focus of the imaging system is set by turning on the magnesium oven and focusing on the PI beam. The polarization of the PI beam needs to be parallel to the table so we can see the fluorescence from the neutral atoms. Once we set the focus we set the RP polarization to horizontal, eliminating PI fluorescence and maximizing collected RP fluorescence.

8.2 Loading

The loading process is simple. The magnesium oven is turned on with ≈ 1.8 A of current. The temperature will reach an equilibrium of about 175 °C. The RP beam is always present, and the PI beam is pulsed on for 30-60 seconds. Then we adjust the frequency of the RP beam to look for the fluorescence from the trapped ions.

We typically load a cloud of 10-100 Mg^+ ions, an image of which is shown in Fig. 8.1. The number of ions trapped depends on the temperature of the magnesium oven, the intensity and the detuning of the PI laser. For a small cloud, we try to Doppler cool [10, 11, 12, 13] the ions. This is done by tuning the frequency of RP beam close to the resonance. When the ion cloud is cooled, it undergoes a phase transition to a state where the ions are arranged in a crystalline structure. (see Fig. 8.1).

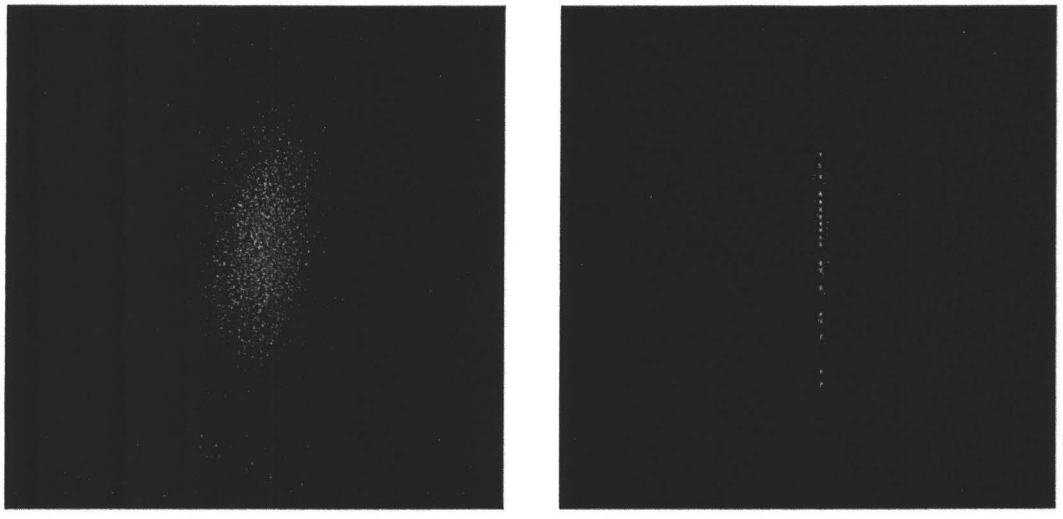

Figure 8.1: Left: image of an ion cloud. The rf voltage is 120 V and dc voltage is 20 V. Right: image of a chain of ions. The rf voltage is 120 V and dc voltage is 1 V.

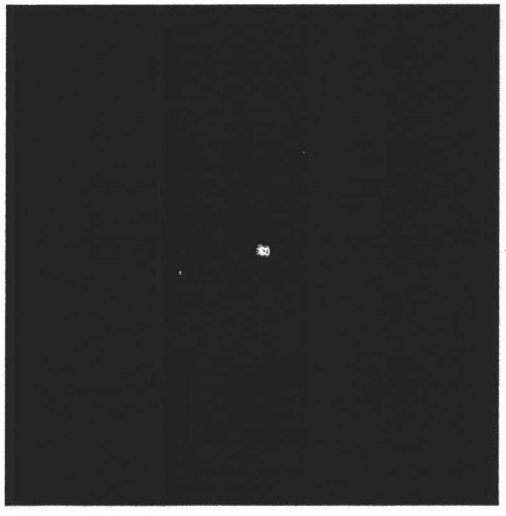

Figure 8.2: Image of a single ion. The rf voltage is 120 V and dc voltage is 10 V.

The process of loading a desired number of Mg^+ ions is complicated by the fact that other charged particles may also be ionized and trapped. The presence of these 'dark ions' can be deduced from the lack of fluorescence at certain positions in the ion crystal. A single ion can be captured when we shorten the exposure time of the PI beam and detune the PI beam farther red from the resonance. Fig. 8.2 shows an image of one single $^{24}Mg^+$ ion.

8.3 Trap Frequencies

The trap frequencies can be measured by applying an oscillating voltage on one of the dc electrodes. This creates a semi-uniform electric field near the ions' location, which creates a time-dependent electric force on the ions. The frequency of the oscillating voltage is scanned. When the voltage is at a resonant frequency of the trap, the ions are heated into large cloud and the fluorescence signal falls off.

We can measure the radial trap frequencies at different rf voltages and deduce the geometric factors in the radial directions. From Eqn. (2.15), the relation between the trap frequency and the rf voltage is

$$\omega^2 = \left(\frac{Q^2\alpha'^2}{2m^2\Omega_T^2}\right) V_{\rm rf}^2 + \frac{QU_{\rm dc}\alpha}{m}. \tag{8.1}$$

So we can fit the data (ω^2, $V_{\rm rf}^2$) to a linear function and find the slope k', then the geometric factor can be derived:

$$\alpha' = \frac{\sqrt{2k'}m\Omega_T}{Q}. \tag{8.2}$$

Fig. 8.3 shows our data and the linear fits. The slopes give the geometric factors in the radial directions:

$$\alpha' = 2.64 \pm 0.01(\text{mm}^{-2}), \quad \beta' = 2.52 \pm 0.05(\text{mm}^{-2}). \tag{8.3}$$

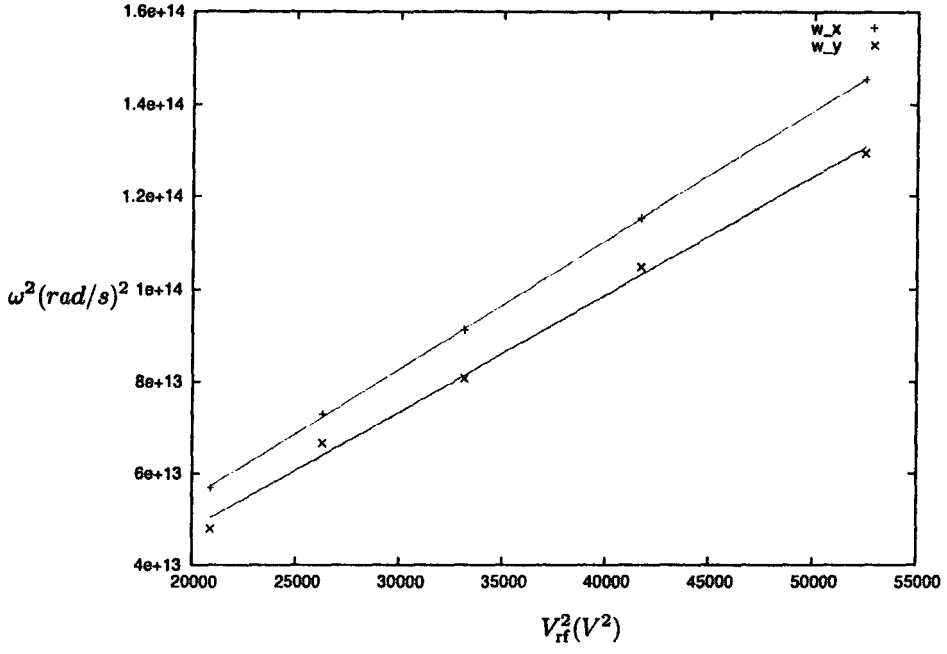

Figure 8.3: The square of the measured radial trap frequencies ω^2 as a function of the square of rf voltage $V_{\rm rf}^2$. The solid lines show a fit of the linear function.

The results agree very well with the results from the computer simulation using CPO program:

$$\alpha' = 2.57(\text{mm}^{-2}), \quad \beta' = 2.56(\text{mm}^{-2}). \tag{8.4}$$

The small difference maybe due to the errors in our measurement of the rod separations.

We can also measure the axial trap frequencies at different dc voltages and deduce the geometric factor in the axial directions in a similar way. Eqn. (8.1) can be rewritten in the axial direction as

$$\omega^2 = \left(\frac{Q\gamma}{m}\right) U_{\rm dc} + \frac{Q^2 V_{\rm rf}^2 \gamma'^2}{2m^2\Omega_T^2}. \tag{8.5}$$

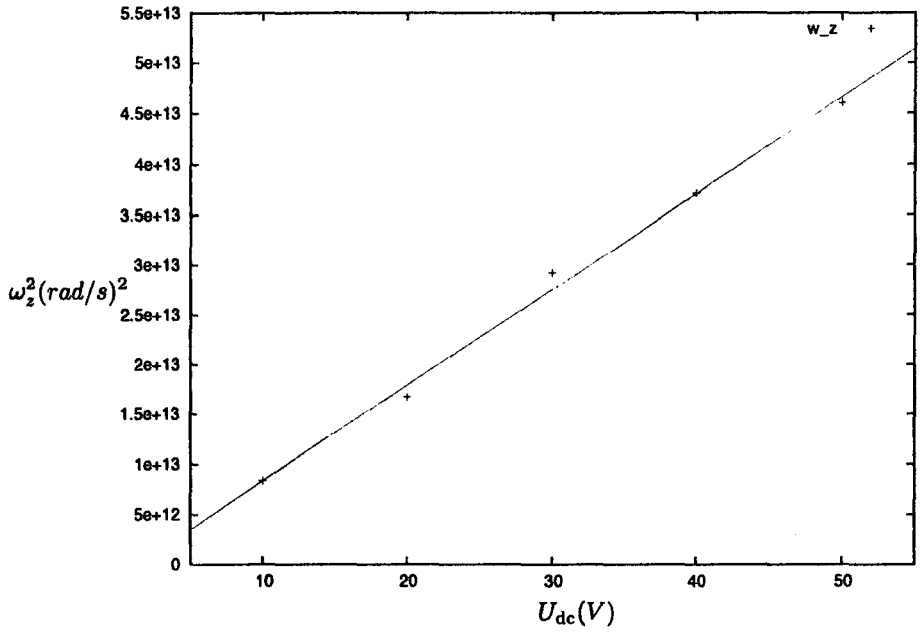

Figure 8.4: The square of the measured axial trap frequency ω_z^2 as a function of the dc voltage $U_{\rm dc}$. The solid lines shows a fit of the linear function.

So the geometric factor in the axial direction can be found by fitting the data (ω_z^2, $U_{\rm dc}$) to a linear function and finding the slope k:

$$\gamma = \frac{km}{Q}. \tag{8.6}$$

Fig. 8.4 shows our data and the linear fit. The slope gives the geometric factor in the axial direction:

$$\gamma = 0.24 \pm 0.01(\mathrm{mm}^{-2}). \tag{8.7}$$

We also measured the separation between the tube electrodes by moving the imaging system to focus on the edge of the tube. This measurement gives a tube separation

3.2 ± 0.1 mm. The error is mainly from the reading of the micrometer. We then used the CPO program to calculate the geometric factor γ for 3.2 mm separation,

$$\gamma = 0.088(\text{mm}^{-2}). \tag{8.8}$$

The difference between these two results may due to several factors: (1) we modeled our tubes as cylinders, but the real tubes have tabs to which the wires are spot weld (see Chapter 4). The simulation shows that 25% change of the tube length will only change γ by about 5%, so this is not sufficient enough to explain the difference. (2) the edge of the tube near the trap side is not perfectly perpendicular to the rod axis. We found that γ strongly depends on the separation between the tubes, so irregular edge of the tube will cause the γ differ from the simulation results. We estimated the irregularity of the edges to be less than 0.2 mm, while the CPO simulation shows that it requires 2.4 mm separation to produce a γ value of 0.24 mm^{-2}, so the irregular edge is still not enough to explain the difference. (3) The polyimide tubes used to insulate the tube electrode from the rod may have some effect on the value of γ; however, we couldn't model the dielectric material in the CPO simulation. The polyimide tubes will increase the capacitance between the dc tube and ground rod. So, if the applied voltages stay the same, the charge on the tubes will be greater compared to the situation where there are no polyimide tubes. We can estimate that the capacitance increases by ε, where $\varepsilon = 3.4$ is the dielectric constant of the polyimide. The change of the capacitance will increase the charge by ε. (This will over-estimate the capacitance and the charge since there are still some field lines pass through the free space from the dc tubes to the ground rods.) So according to this estimate, the extra charges would increase the γ value to $0.088 \times 3.4 = 2.99$ mm^{-2}, which is closer to the measured value 2.4 mm^{-2}. We suspect the insulating material is the main reason for the difference.

Bibliography

[1] R. Feynman, Int. J. Theor. Phys. **21**, 467 (1982).

[2] D. Deutsch, Proc. R. Soc. London A **400**, 97 (1985).

[3] D. Simon, in *Proc. 35th Annual Symposium on Foundations of Computer Science* (IEEE Computer Society Press, Los Alamitos, California, 1994).

[4] P. Shor, SIAM J. Comput. **26**, 1484 (1997).

[5] H. Dehmelt, Rev. Mod. Phys. **62**, 525 (1990).

[6] W. Paul, Rev. Mod. Phys. **62**, 531 (1990).

[7] S. Chu, Rev. Mod. Phys. **70**, 685 (1998).

[8] C. N. Cohen-Tannoudji, Rev. Mod. Phys. **70**, 707 (1998).

[9] W. Phillips, Rev. Mod. Phys. **70**, 721 (1998).

[10] D. Wineland and H. Dehmelt, Bull. Am. Phys. Soc. **20**, 637 (1975).

[11] T. Hänsch and A. Schawlow, Opt. Commun. **13**, 68 (1975).

[12] D. Wineland, R. Drullinger, and F. Walls, Phys. Rev. Lett. **40**, 1639 (1978).

[13] W. Neuhauser, M. Hohenstatt, P. Toschek, and H. Dehmelt, Phys. Rev. Lett. **41**, 233 (1978).

[14] J. Cirac and P. Zoller, Phys. Rev. Lett. **74**, 4091 (1995).

[15] C. Monroe *et al.*, Phys. Rev. Lett. **75**, 4714 (1995).

[16] Q. Turchette *et al.*, Phys. Rev. Lett. **75**, 4710 (1995).

[17] F. Schmidt-Kaler *et al.*, Nature **422**, 408 (2003).

[18] D. Leibfried *et al.*, Nature **422**, 412 (2003).

[19] A. Steane, Appl. Phys. B **64**, 623 (1997).

[20] D. Leibfried, R. Blatt, C. Monroe, and D. Wineland, Rev. Mod. Phys. **75**, 281 (2003).

[21] M. A. Nielsen and I. L. Chuang, *Quantum Computation and Quantum Information* (Cambridge University Press, Cambridge, 2000).

[22] L. Toppozini, Master's thesis, McMaster University, 2006.

[23] P. Ghosh, *Ion Traps* (Clarendon, Oxford, 1995).

[24] M. Combescure, Ann. Inst. Henri Poincaré **44**, 293 (1986).

[25] R. Glauber, in *Laser Manipulation of Atoms and Ions, Proceedings of the International School of Physics "Enrico Fermi" Course 118*, edited by E. Arimondo, W. Phillips, and F. Strumia (Horth-Holland, Amsterdam, 1992).

[26] J. Cirac *et al.*, Phys. Rev. A **49**, 421 (1994).

[27] P. Bardroff, C. Leichtle, G. Schrade, and W. Schleich, Phys. Rev. Lett. **77**, 2198 (1996).

[28] J. Prestage, G. Dick, and L. Maleki, J. Appl. Phys. **66**, 1013 (1989).

[29] M. Raizen *et al.*, J. Mod. Opt. **39**, 233 (1992).

[30] M. Raizen *et al.*, Phys. Rev. A **45**, 6493 (1992).

[31] D. Berkeland, Rev. Sci. Instrum. **73**, 2856 (2002).

[32] P. Kapitsa, Zh. Eskp. Teor. Fiz. **34**, 242 (1951).

[33] M. Abramowitz and I. Stegun, *Handbook of Mathematical Functions* (Dover, New York, 1972).

[34] J. Mathews and R. Walker, *Mathematical Methods of Physics*, 2nd ed. (Benjamin, California, 1970).

[35] D. Berkeland *et al.*, J. Appl. Phys. **83**, 5025 (1998).

[36] H. Straubel, Naturwissenschaften **18**, 506 (1955).

[37] D. Kielpinski, C. Monroe, and D. Wineland, Nature **417**, 709 (2002).

[38] S. Seidelin *et al.*, Phys. Rev. Lett. **96**, 253003 (2006).

[39] K. R. Brown *et al.*, Phys. Rev. A **75**, 015401 (2007).

[40] M. Poitzsch, J. Bergquist, W. Itano, and D. Wineland, Rev. Sci. Instrum. **67**, 129 (1996).

[41] U. Tanaka *et al.*, Opt. Lett. **22**, 1353 (1997).

[42] P. Barton *et al.*, Phys. Rev. A **62**, 032503 (2000).

[43] T. Crow, Am. J. Phys. **55**, 817 (1987).

[44] F. Hart, Am. J. Phys. **57**, 559 (1989).

[45] F. Read, A. Adams, and J. Soto-Montiel, J. Phys. E (Sci. Instrum.) **4**, 625 (1971).

[46] J. Schiffer, Phys. Rev. Lett. **70**, 818 (1993).

[47] D. H. Dubin, Phys. Rev. Lett. **71**, 2753 (1993).

[48] D. Enzer *et al.*, Phys. Rev. Lett. **85**, 2466 (2000).

[49] D. DiVincenzo, Fortschr. Phys. **48**, (2000).

[50] ARDA road map, http://qist.lanl.gov/, 2004.

[51] M. Barrett *et al.*, Nature **429**, 737 (2004).

[52] M. Riebe *et al.*, Nature **429**, 734 (2004).

[53] D. Kielpinski *et al.*, Science **291**, 1013 (2001).

[54] C. Langer *et al.*, Phys. Rev. Lett. **95**, 060502 (2005).

[55] G. Woodgate, *Elementary Atomic Structure*, 2nd ed. (Oxford University Press, Oxford, 1983).

[56] P. Fisk *et al.*, IEEE Trans. on Instrum. and Meas. **44**, 113 (1995).

[57] S. Olmschenk *et al.*, 2007, arxiv:0708.0657v1 [quant-ph].

[58] R. Loudon, *The Quantum Theory of Light*, 3rd ed. (Oxford University Press, Oxford, 2000).

[59] H. Metcalf and P. van der Straten, *Laser Cooling and Trapping* (Springer, New York, 1999).

[60] B. E. King, Ph.D. thesis, University of Corolado, 1999.

[61] M. Acton *et al.*, Quant. Inf. Comput. **6**, 465 (2006).

[62] P. Farrell and W. MacGillivray, J. Phys. A: Math. Gen. **28**, 209 (1995).

[63] E. Condon and H. Odabasi, *Atomic Structure* (Cambridge University Press, Cambridge, 1980).

[64] A. Edmonds, *Angular Momentum in Quantum Mechanics* (Princeton University Press, Princeton, 1974).

[65] T. Schaetz *et al.*, Phys. Rev. Lett. **94**, 010501 (2005).

[66] D. Wineland *et al.*, Phil. Trans. R. Soc. Lond. A **361**, 1349 (2003).

[67] A. Barenco, D. Deutsch, A. Ekert, and R. Jozsa, Phys. Rev. Lett. **74**, 4083 (1995).

[68] A. Barrenco *et al.*, Phys. Rev. A **52**, 3457 (1995).

[69] A. M. Steane, Phys. Rev. A **68**, 042322 (2003).

[70] A. Peres, *Quantum Theory: Concepts and Methods* (Kluwer, Dordrecht, 1995).

[71] R. Boivin and S. Srivastava, J. Phys. B: At. Mol. Opt. Phys. **31**, 2381 (1998).

[72] D. N. Madsen *et al.*, J. Phys. B: At. Mol. Opt. Phys. **33**, 4981 (2000).

[73] W. Macalpine and R. Schildknecht, Proc. of the IRE **1959**, 2099 (1959).

[74] A. Zverev and H. Blinchikoff, IRE Trans. on Comp. Parts **1961**, 99 (1961).

[75] S. Fiedziuszko and R. Kwok, IEEE MTT-S **1998**, 1323 (1998).

[76] F. Rosebury, *Handbook of Electron Tube and Vacuum Techniques* (American Insititute of Physics, New York, 1993).

[77] A. Siegman, *Lasers* (University Science Books, California, 1986).

[78] R. Drever *et al.*, Appl. Phys. B **31**, 97 (1983).

[79] E. D. Black, Am. J. Phys. **69**, 79 (2001).

[80] A. Yariv, *Quantum Electronics*, 2nd ed. (John Wiley & Sons, New York, 1975).

[81] G. Boyd and D. Kleinman, J. Appl. Phys. **39**, 3597 (1968).

[82] H. Kogelnik, E. Ippen, A. Dienes, and C. Shank, IEEE Journal of Quantum Electronics **QE-8**, 373 (1972).

[83] T. Hänsch and B. Couillaud, Opt. Commun. **35**, 441 (1980).

[84] C. Davis, *Lasers and Electro-Optics* (Cambridge University Press, Cambridge, 1996).

[85] W. Demtröder, *Laser Spectroscopy*, 3rd ed. (Springer, New York, 2003).

[86] W. Bennet Jr., Phys. Rev. **126**, 580 (1962).

[87] D. Leibfried, private communication, 2006.

[88] D. James, Appl. Phys. B **66**, 181 (1998).

[89] E. Hecht, *Optics*, 4th ed. (Addison-Wesley, San Francisco, 2002).